Title

Characterizing Brown Dwarfs and Exoplanets in the Mid-Infrared

Permalink

https://escholarship.org/uc/item/2x1629bv

Author

Miles, Brittany E

Publication Date

2022

Peer reviewed|Thesis/dissertation

UNIVERSITY OF CALIFORNIA
SANTA CRUZ

CHARACTERIZING BROWN DWARFS AND EXOPLANETS IN THE MID-INFRARED

A dissertation submitted in partial satisfaction of the
requirements for the degree of

DOCTOR OF PHILOSOPHY

in

ASTRONOMY AND ASTROPHYSICS

by

Brittany Elaina Miles

June 2022

The Dissertation of Brittany Elaina Miles
is approved:

Professor Andrew Skemer, Chair

LAO Director Philip Hinz

Professor Jonathan Fortney

Professor Caroline Morley

Peter Biehl
Vice Provost and Dean of Graduate Studies

Table of Contents

List of Figures

List of Tables

Abstract

Characterizing Brown Dwarfs and Exoplanets in the Mid-Infrared

by

Brittany Elaina Miles

My dissertation combines the atmospheric characterization of brown dwarfs using mid-infrared spectroscopy with the development of next generation mid-infrared detector technology. Brown dwarfs have similar atmospheric physics and chemistry to gas giant exoplanets, but they are much easier to observe because they do not suffer from host star obscuration. Brown dwarfs are high-quality testing grounds for atmospheric models, optimizing requirements for exoplanet-focused instrumentation, and planning observations with the James Webb Space Telescope. I led two mid-infrared observational projects to characterize the atmospheres of brown dwarfs. First, I took 3 μm -4 μm spectra of VHS 1256b and PSO 318.5, two analogs of the HR 8799 planets using Keck/NIRSPEC. I detected methane, providing evidence of disequilibrium chemistry. For my second project, I acquired Gemini/GNIRS 4.5 μm - 5 μm spectra of four ultra-cool brown dwarfs. Combined with previously existing mid-infrared spectra of four additional brown dwarfs I show that brown dwarfs 700 K and below have disequilibrium carbon monoxide absorption. For my last project, I tested a 10 μm detector that will be photon-noise-limited, unlike the mid-infrared detectors currently used in astronomical instruments. My detector test setup shows that the 10 μm detector can be operated cryogenically and fast enough to overcome the mid-infrared sky background.

To my Mother and Sister.

Acknowledgments

My family, friends, partner, and community in Santa Cruz made the journey to my PhD possible. I love y'all and thank you for allowing my work to flourish.

I am incredibly thankful for all of the things my advisor Andy has done to support me as a person and student during my time at UC Santa Cruz. I have developed so much more confidence in my work and have had the privilege of being a part of cutting-edge science since day one. There were many times when I struggled to see the end of scientific problems, but Andy keep me going and constantly reminded me of the big picture. I am so lucky to have an incredible mentor and I will miss our weekly meetings about research, joking around, or whatever is going on in the world.

I want to thank Phil, who has closely mentored me through my first instrumentation project even through the pandemic. No matter how basic of a question/need I had, you made sure I had the info and connections to get things done. Working together I learned to appreciate going with the flow in research given how often unexpected things happen in instrumentation. No matter what the outcome of research I get to have a career where I get to understand and explore the universe.

Numerous staff - telescope operators, engineers, and administrative staff, made sure my observational data was taken, I was paid on time, lab orders went through, and parts were built. Their labor made all of the work in my thesis possible.

Chapter 1

Introduction

1.1 Brown Dwarfs and Their Importance to Exoplanet Science

Brown dwarfs are astrophysical objects primarily composed of hydrogen that are not massive enough to fuse hydrogen like the lowest mass stars (Kumar, 1963). More massive brown dwarfs can burn deuterium for the first hundred million years (Spiegel & Burrows, 2012). As time passes, brown dwarfs lose their heat from formation, cooling and collapsing in size. Brown dwarfs are an important part of both stellar astrophysics and exoplanetary science.

Last century brown dwarfs were theorized in the 60s and discovered in the 1980 and 90s. The first few brown dwarfs were initially found through infrared imaging around stellar companions (Becklin & Zuckerman, 1988; Nakajima et al., 1995), then infrared sky surveys discovered larger numbers of nearby brown dwarfs. Ground based near-infrared surveys like the Two Micron All-Sky Survey and Deep Near-Infrared Survey (Kirkpatrick et al., 1997; Delfosse et al., 1997; Ruiz et al., 1997) discovered many relatively warm brown dwarfs and the space based WISE survey provided mid-infrared photometry for these warmer brown dwarfs while also discovering further and cooler brown dwarfs Kirkpatrick et al. (2011); Cushing et al. (2011). Follow-up ground-based infrared spectroscopy and space-based observations from the Hubble Space Telescope, Spitzer, and AKARI have vastly improved our understanding of brown dwarf atmospheres and their composition since their discovery Cushing et al. (2006); Sorahana & Yamamura (2012, 2014). In the 2020s and onward, JWST will be used to provide the brown dwarf and exoplanet community with more sensitivity and spectral coverage than any of the previously mentioned instruments/surveys.

Brown dwarfs, Jupiter, and Jupiter-like planets likely have different formation mechanisms, but are all mainly hydrogen with secondary gases within their atmospheres. For all of these objects, portions of the upper atmosphere are cold enough where gases can condense into clouds. My observational graduate research focuses on studying brown dwarfs as Jupiter-like exoplanet analogs that bridge the gap between our current characterization limits with direct imaging around other planetary systems and planets in our own Solar System like Jupiter. Comparing equivalent observations, an isolated brown dwarf will produce higher quality data compared to a similar temperature exoplanet or brown dwarf companion that is obscured by a host star. The current effective temperature range of known brown dwarfs is significantly wider and cooler than known directly-imaged exoplanets, allowing us to understand what atmospheric chem-

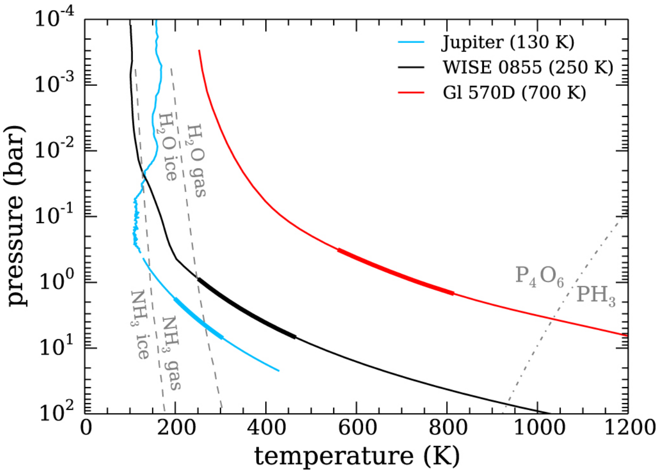

Figure 1.1: Plot from Skemer et al. (2016b) showing the atmospheric pressure-temperature profiles of WISE 0855, the coldest known brown dwarf and Jupiter. Both WISE 0855 and Jupiter are cool enough to condense water vapor into clouds within their atmosphere. WISE 0855 and other cold brown dwarfs fill the gap between our sensitivity limits with direct imaging (∼ 700 K ex. Gl 570 D)

istry and cloud structures we may find when cooler gas giant planets are detected with direct imaging (Figure 1.1). Our understanding of brown dwarfs atmospheres is also not complete, therefore pushing for extended wavelength coverage and reaching higher spectral resolution observations are important for testing and validating atmospheric models and theories.

Brown dwarfs are typically described by their spectral type (L, T, or Y) which is loosely correlated with effective temperature. L dwarfs are the warmest brown dwarfs that span about ∼2800 K down to ∼1400 K, and have carbon monoxide as their dominant carbon-bearing gas. T-dwarfs are ∼1400 K to ∼600 K, and their atmospheres primarily have methane as the dominant carbon bearing gas. L dwarfs and the warmest T-dwarfs closely mimic most of the directly imaged exoplanets we have been able to

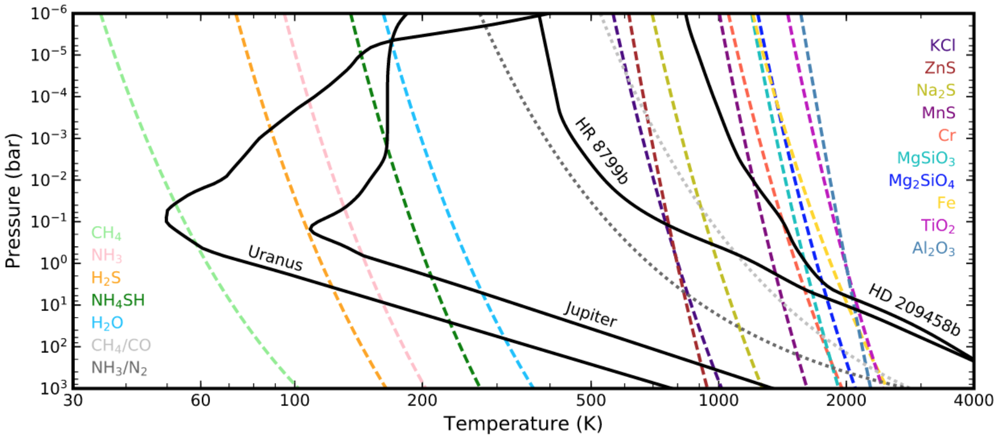

Figure 1.2: Figure from Gao et al. (2021) showing a range of potential clouds that condense out of the atmospheres of Jupiter-like planets and exoplanets. Understanding the presence and composition of different gas species and clouds within similar temperature brown dwarfs is crucial for properly interpreting the spectra of planets

image to date, namely the HR 8799 planets. At the L to T transition, atmospheres become cold enough where silicate clouds can begin to condense out, also causing brown dwarf spectra to appear redder in near-infrared band passes.

Y-dwarfs, which have been recently discovered are the coldest spectral type of brown dwarf. These brown dwarfs are still methane rich, but potentially have water, alkali salts, and sulfide clouds that condense out in their upper atmospheres. There are currently no directly-imaged exoplanets that share the same effective temperature range as Y-dwarfs. Ground-based slit spectroscopy, and upcoming space-based observations with JWST will offer high signal-to-noise, broad wavelength coverage data that will cover the to-be explored parameter space of directly imaged exoplanets prior to their discovery.

1.2 The Future of Direct Imaging

Direct imaging is an observational technique that captures the light emitted from extrasolar planets and/or widely separated brown dwarf companions. Direct imaging surveys are biased towards young, massive planets that have a significant amount of internal heat from formation. Most known exoplanets are detected through indirect means which are also biased towards larger, more massive planets. However, these methods, specifically the transiting and radial velocity methods are sensitive to smaller, shorter-periods planets that are Earth and Neptune sized respectively (Gaudi, 2022). Using direct imaging, the only class of planet we have been sensitive to are relatively large, widely separated Jupiter-like exoplanets (Bowler, 2016). To capture the full range of planet classes, including smaller, habitable planets like Earth we must extend the conventional wavelength coverage of direct imaging exoplanet instruments to expand their detection and characterization capabilities. Many current and future exoplanet missions will be able to detect smaller exoplanets, but instruments that make use of direct imaging typically also have the capability to perform low to high resolution spectroscopy without having to account for stellar activity in the case of transit spectroscopy.

The 1μm - to 5μm portion of the infrared is frequently used to find and characterize directly imaged exoplanets which are young and Jupiter-sized. Earth-like planets have the highest contrast relative to a Solar-type star around 10 μm, making this the ideal wavelength range to search for these types of planets. 30-meter class telescopes will be able to detect Earth-like planets in the mid-infrared however, a major challenge to this is choosing the most efficient detector for hundred hour integrations needed to find a single planet. The most common type of detector used in mid-infrared instruments are arsenic doped silicon detectors (Si:As) but these detectors have excess low frequency noise (ELFN) at long integration times reducing the signal by a factor of four due to extra chopping during the observing sequence. Mercury-Cadmium-Telluride (HgCdTe) detectors are commonly used in the near-infrared without ELFN noise and have had their wavelength cutoffs extended further into the mid-infrared for space based applications. My instrumentation work is dedicated to understanding if and how HgCdTe detectors can be used in a laboratory setting and ultimately used within ground-based, mid-infrared astronomical instruments. Mid-infrared imaging and spectroscopy are often seen as niche techniques, but developing this observational capability at observatories expands our ability to detect potential biosignatures in Earth-like planets (Madden & Kaltenegger, 2020), understand the types of clouds that influence the atmospheres of gas giant exoplanets (Luna & Morley, 2021), and explore other trace species not typically accessible in the near-infrared (Encrenaz, 2022).

1.3 Atmospheric Characterization of Brown Dwarfs and Exoplanets

After brown dwarfs and directly imaged exoplanets are found, their photometry and/or spectra are compared to models in order understand their properties such as age, temperature, gas and cloud composition, and etc. There are several approaches to model fitting, but in general for my work a set of basic assumptions about atmospheric physics and chemistry need to be made to create a parameter space or grid of a models for comparison. Readily available model grids used to characterize brown dwarfs and directly imaged exoplanets are useful for placing generic constraints on temperature, composition, cloud presence and age however, there are several atmospheric properties such cloud particle size distribution, cloud height extent, and disequilibrium chemistry that require some attention on an object by object basis. Brown dwarfs with similar spectral typing and color may even exhibit different spectral features and slopes.

There is merit to detailed analysis of individual brown dwarfs given their higher data quality and spectral coverage, allowing us to understand atmospheric effects that are yet to be fully parameterized. At the time of my graduate career, there are only a handful of directly imaged exoplanets (Bowler, 2016) and Y-spectral type brown dwarfs (Cushing et al., 2011; Kirkpatrick et al., 2012; Luhman, 2014). In addition to this, atmospheric model grids are not perfect at very cool effective temperatures (<500K) when including clouds. The model comparisons in my research focuses heavily on atmospheric disequilibrium chemistry and clouds, two parameters that take post processing to reasonably fit data. The goal of my model interpretations are not to get everything perfect, but to understand which atmospheric phenomena can explain most of the handful of spectra we have.

1.4 Dissertation Overview

This first portion of this dissertation covers advancement in our understanding of disequilibrium chemistry in the atmospheres of brown dwarfs and directly imaged exoplanets using mid-infrared spectroscopy. Chapter 2 covers observations of VHS 1256b and PSO 318.5 that demonstrated that methane abundances can be depleted in the atmospheres of brown dwarfs and directly imaged exoplanets because of disequilibrium chemistry. I cover the observation strategy and data reduction techniques used to get 3 μm to 4 μm spectroscopy of both brown dwarfs in Section 2.2. In Section 2.3 I describe the efforts to model that data's molecular abundances and cloud properties. I end the section by describing the implications these observations have for the HR 8799 exoplanets and similar temperatures planets. Chapter 3 discusses the presence of disequilibrium carbon monoxide in the atmospheres of late-T and Y-dwarfs. Section 3.1 describes the queue mode observations used to get new 4.5 μm – 5.0 μm spectroscopy of 4 brown dwarfs, description of the published spectra added to the sample. Section 3.2 describes the photometry used to calculate the luminosity for inferring effective temperature for each object. Section 3.3 shows model comparisons of the spectra to equilibrium models and their discrepancies. Section 3.4 address the current assumptions of disequilibrium and adjustments made to equilibrium models to match the carbon monoxide features. Section 3.5 summarizes the inferred carbon monoxide abundances of each brown dwarfs and the estimated rate of atmospheric mixing. Section 3.6 finishes this chapter by discussing the implications for future directly imaged exoplanets.

The last third of my dissertation in Chapter 4 covers my instrumentation work to assess the potential of mercury cadmium telluride detectors for use behind thirty meter class telescopes. In Section 4.1 I will describe the detector we are testing and why it was originally created. In Section 4.3, I will discuss the theory for the set up that would enable the detector to be used on sky for exoplanet applications. Section 4.4 will document the test dewar set up for the detector and optics chosen for the testing and iterations of the set up. Section 4.5 will describe the testing performed on the detector and a MUX (detector multiplexer without photosensitive layer and their result. Lastly, I will discuss the analysis techniques that will be used to characterize the detector.

Chapter 2

Methane in Analogs of Young Directly Imaged Exoplanets

Methane (CH_4) is fundamental to our understanding of planet formation and other processes that influence the composition of an exoplanet's atmosphere (Öberg et al., 2011; Barman et al., 2011a). Methane is detected on the majority of Solar System planets, represents a large fraction of the carbon budget in gas giant planets, and is a significant greenhouse gas produced by biological and geological processes on Earth (Lunine, 1993; Karkoschka, 1994; Keppler et al., 2006; Guzmán-Marmolejo & Segura, 2015). Detecting and constraining methane is extremely important for characterizing exoplanets as a whole.

Current directly imaged gas-giants like the HR 8799 planets (Marois et al., 2008, 2010) show much less methane in their H band spectra than is seen in the majority of similar temperature field brown dwarfs (Bowler et al., 2010; Barman et al., 2011a). Most directly imaged exoplanets also have red near-infrared colors compared to most field brown dwarfs, especially near the L to T transition (see Figure 2.1, Liu et al. (2016)). The L to T transition is both an evolutionary transition and a region of the near infrared color-magnitude diagram where: 1) Cloud properties rapidly alter the near infrared colors of brown dwarfs by several magnitudes over a small temperature range and 2) The dominant carbon bearing, photospheric gas transitions from carbon monoxide (CO) to methane (CH_4) (Burrows et al., 1997; Ackerman & Marley, 2001; Burgasser et al., 2002; Geballe et al., 2002; Tsuji & Nakajima, 2003; Knapp et al., 2004; Burrows et al., 2006; Saumon & Marley, 2008). The relatively red near infrared colors of directly imaged exoplanets have primarily been explained lingering photospheric clouds composed of silicate and iron condensates (Madhusudhan et al., 2011; Marley et al., 2012; Currie et al., 2011). The lack of methane is thought to be the result of disequilibrium chemistry, driven by vertical mixing interchanging cool CH_4-rich gas with warmer CO-rich gas (Barman et al., 2011b,a; Zahnle & Marley, 2014).

To understand cloud properties and atmospheric mixing in exoplanets, broad wavelength coverage is essential for breaking degeneracies. Atmospheric models that only consider clouds can reproduce the near infrared (.8 μm - 2.3 μm) colors of exoplanets, but under-predict their fluxes from 3 μm - 4μm (Hinz et al., 2010; Skemer et al., 2012, 2014; Barman et al., 2011b, 2015). Various studies have been able to get better fits to 1 μm - 5 μm photometry and spectroscopy of 2MASSJ 1207334-393254b (2MASS 1207 b) (Chauvin et al., 2004) and the HR 8799 planets by including the effects of iron and silicate clouds, patchy clouds, and non-equilibrium chemistry (Marois et al., 2008, 2010; Hinz et al., 2010; Barman et al., 2011b,a, 2015; Currie et al., 2011; Konopacky et al., 2013; Skemer et al., 2011; Marley et al., 2012; Skemer et al., 2012, 2014; Currie et al., 2014; Barman et al., 2015).

Currently, our understanding of directly-imaged exoplanet atmospheres is limited by data quality. Directly-imaged exoplanets are difficult to observe because they are faint compared to the glare of their much brighter host stars. Young, free floating and wide separation planetary mass objects often share the same color space as directly-imaged gas giant exoplanets (Faherty et al., 2013; Liu et al., 2016). These objects are significantly easier to study in detail and provide insight into the atmospheric properties of bona fide gas giant exoplanets.

In this study, we present L band (3 μm - 4 μm) spectra of two exoplanet analogs, VHS J125601.92-125723.9b (VHS 1256 b, Gauza et al., 2015) and PSO J318.5338-22.8603 (PSO 318.5, Liu et al., 2013). The opacity of CH_4 dominates over all other gases within the L band (peaking at ~3.3 μm see Morley et al. (2014); Yurchenko & Tennyson (2014)) allowing for an unambiguous detection, even at low abundances. VHS 1256b and PSO J318.5 are both low gravity objects that have similar colors to the HR 8799 planets (Figure 2.1) and show no near infrared CH_4 absorption.

VHS 1256 b is a wide companion (8" separation) to a late M dwarf binary system (Stone et al., 2016) making it accessible to long slit spectroscopy. The age of the VHS 1256 system is not well known, however VHS 1256 b's weak absorption from neutral gases (Na and K) and collisionally induced absorption from hydrogen indicates a low surface gravity, which implies youth (Gauza et al., 2015). Model fits to the optical to mid infrared photometry of VHS 1256 b suggests a very cloudy atmosphere (Rich et al., 2016). PSO J318.5 is a free floating object that is a member of the β Pictoris moving group, making it about 20 - 25 Myr old (Allers et al., 2016). The time series photometry and near infrared spectra of PSO 318.5 also suggest a cloudy atmosphere (Biller et al., 2015, 2018).

In Sections 3.1 and 2.2 we present L band observations and reductions of VHS 1256b and PSO J318.5. In Section 2.3 we quantify the significance of the CH_4 features and fit our L band spectra and published near-infrared spectra with atmospheric models. We discuss the astrophysical ramifications of our results and future observations with ground-based high-contrast imagers and the *James Webb Space Telescope* in Section 2.4. We summarize our results in Section 2.5.

2.1 Observations

We observed VHS 1256 b and PSO 318.5 on UT 2016 June 19 during photometric conditions using the NIRSPEC spectrograph (McLean et al., 1998), an instrument on the Keck II Telescope on Mauna Kea. NIRSPEC was set up in low resolution mode with the KL filter and a 42 ″by .570 ″slit. Two grating positions were used to achieve a wavelength coverage from 2.9 μm to 4.4 μm with a resolution of 1300 (in low resolution mode, NIRSPEC has a nominal resolution of $\sim$ 2500 with a .380″slit). Between 4.2 μm - 4.4 μm the atmospheric transmission is zero and the KL filter only transmits out to 4.2 μm. Our observations are background limited due to the high thermal emission from the

Earth's atmosphere. An integration time of 0.5 seconds with 120 co-adds was chosen for each spectral image. The spectral images were taken in an ABBA nod pattern. Telluric calibrations were taken before and after every two or three ABBA sequences for both science targets. A0V and A1V stellar spectra were taken at the same airmass as the science targets and used as telluric calibrators. The mean precipitable water vapor for our observations was 1.3 mm and the standard deviation over the night was 0.06 mm. There were only smooth changes in water vapor over each science observation block. The slit was not aligned to the parallactic angle for every observation over the course of the night, however atmospheric dispersion across the L band is negligible A summary of all NIRSPEC observations is listed in Table 2.1.

2.2 Data Reduction

2.2.1 Removing NIRSPEC Detector Artifacts and Background Subtraction

Bad pixels were identified by looking at the entire night of spectral images for anomalous values (negative or extremely low/high values across sky lines) appearing at the same position. Bad pixels in the spectral images are replaced by the average of the surrounding pixels. A-B pair nod subtraction is done to eliminate the majority of the sky lines from the traces in the calibrator and science spectral images. Each A-B pair produces a spectral image with a positive and a negative trace. The top right quadrant (redder half in low resolution mode) of NIRSPEC's detector has pattern noise

Science Target	**Grating Angle (°)**	**Wavelength Coverage (μm)**	**AB Pairs (N)**	**Science Airmass**	**Telluric Calibrator**	**AB Pairs (N)**	**Telluric Airmass**
VHS 1256 b	32.76	2.9 - 3.8	6	1.24	HIP 63109	3	1.24
VHS 1256 b	32.76	2.9 - 3.8	4	1.42	HIP 62096	2	1.42
VHS 1256 b	34.19	3.5 - 4.4	6	1.23	HIP 63109	2	1.29
VHS 1256 b	34.19	3.5 - 4.4	6	1.39	HIP 62096	2	1.50
PSO 318.5	32.76	2.9 - 3.8	6	1.72	HIP 101384	2	1.72
PSO 318.5	32.76	2.9 - 3.8	4	1.38	HIP 99592	2	1.40
PSO 318.5	32.76	2.9 - 3.8	6	1.35	HIP 104810	2	1.36
PSO 318.5	32.76	2.9 - 3.8	4	1.33	HIP 109775	2	1.43
PSO 318.5	34.19	3.5 - 4.4	6	1.68	HIP 101384	2	1.64
PSO 318.5	34.19	3.5 - 4.4	4	1.37	HIP 99592	2	1.40
PSO 318.5	34.19	3.5 - 4.4	6	1.35	HIP 104810	2	1.36
PSO 318.5	34.19	3.5 - 4.4	4	1.32	HIP 109775	2	1.41

Table 2.1: The reported airmasses of the science target and calibrator observations are median values. Our observations extend out to 4.4 μm in wavelength coverage, but the transmission of the KL filter beyond 4.2 μm is zero. Each nod consists of 120 co-adds of 0.5 second exposures.

that appears as a horizontal row of increased noise every eight pixels that is primarily along the spatial direction. The pattern noise response is always smaller than the sky emission and calibrator stars, but changes quickly between exposures making it difficult to remove with A-B pair nod subtraction. The width of the pattern noise was one pixel for all observations of VHS 1256 b. The first block of PSO 318.5 data in the 32.76° grating setting has one pixel wide pattern noise. The pattern noise width in the last three blocks of the same setting increased to a width of two pixels. The first half and last half of the 34.19° grating setting PSO 318.5 data have one and two pixel wide pattern noise respectively. This pattern noise was addressed in the A-B pair subtracted spectral images for each pixel by doing a linear interpolation using the pixel above and the pixel below from the affected rows.

2.2.2 Spectral Image Rectification and Residual Sky Subtraction

The spectral traces are curved in the A-B pair subtracted spectral images and are rectified before extraction. Centroids are fit along the traces of the calibrator star spectral images to estimate the deviation from a straight line and create the spatial rectification map. The spatial rectification map is applied to an A+B image of the calibrator star, where the sky lines are used to create a second rectification map for the wavelength direction. Creating rectification maps from the science targets is difficult because their traces are extremely faint. Therefore, the two spatial and spectral rectification maps calculated from the calibrator star are applied to the A-B images of the calibrator star and the A-B images of the associated science target. After nod subtracting and rectifying the calibrator and science images, there is still excess sky to be removed. At each row along the entire wavelength direction, the median of the pixels along spatial direction is subtracted off.

2.2.3 Wavelength Solution

The wavelength solution is calculated by fitting a second order polynomial to the sky emission lines along the wavelength direction of the spatially and spectrally rectified A+B calibrator images. The spectral features are identified by referencing a smoothed model of the Mauna Kea Sky [1] to a resolution of 1300, matching the data. For the 32.76° grating setting 18 benchmark features were used to estimate the wavelength solution. For the 34.19° grating setting, 6 benchmark features were used. We estimate the uncertainty in the wavelength solution by taking the difference between the initial wavelengths of the benchmark lines and the final wavelengths of the benchmark lines after the wavelength solution has been assigned. On average there is a .4 pixel or $2.5 * 10^{-4}$ μm offset, but it is not significant for our analysis and is addressed by binning the spectra.

2.2.4 Spectral Extraction and Error Estimation

To find the centers and widths of the traces we take the mean of the fully rectified A-B spectral images and sum along the wavelength direction. A Gaussian is fit to the positive and negative trace profiles and the standard deviation of the profile

---

[1] www.gemini.edu/sciops/telescopes-and-sites/
observing-condition-constraints/ir-background-spectra

is used to estimate the optimal radius (1.5852σ,[2] typical radius was 3.5 pixels) for the boxcar extraction. To estimate the error at every wavelength element, we take the nearest 25 pixels to the left and right of the trace centroid, mask out the trace within the extraction radius, fit a first order polynomial to the counts and pixel positions, then take the variance of the residual of the fit from the row counts. The goal of this is to capture the average noise away from some baseline profile which is not necessarily constant across an entire wavelength. The variance of the residual is multiplied by the square root of the extraction width to get an error at each wavelength element.

2.2.5 Telluric and Relative Flux Calibration

The calibrators and the science targets will have their spectra influenced by the transmission of the Earth's atmosphere, which includes absorption from gaseous methane. The absorption of Earth's atmosphere is addressed by dividing the raw science spectrum by a telluric calibrator spectrum, which has a known response such as a black body. To account for the transmission of Earth's atmosphere, each science trace is telluric calibrated by dividing the extracted trace by an A0 or A1 star.

The errors of the telluric calibrated science spectrum are calculated with standard error propagation, using error information from the extracted science trace and the telluric spectrum. The background from the science trace is the dominant source of error. The telluric calibrated line of the science target is then multiplied by Planck's Law at the appropriate temperature based on the spectral type of the calibrator star.

---

[2] http://wise2.ipac.caltech.edu/staff/fmasci/GaussApRadius.pdf

We have two telluric calibrated spectra for every A-B image. Our science observations were bracketed by A0 and A1 stars at similar air masses for a good telluric correction, which is important especially around the methane feature at 3.3 μm. Even though the Earth's transmission is low near 3.3 μm, we still have significant signal for our calibrators (Figure 2.2).

To quantify the quality of the telluric calibration, we extract the calibrator spectra taken before and after each science target block, normalize by the median, and then divide the before calibrator by the after calibrator. The ratio of the normalized "before" calibrator to the normalized "after" calibrator should be unity, but there are deviations, especially where the atmospheric transmission is very low. The deviation from one is interpreted as a percentage error that is included in the error of the final spectrum.

For each science target, the telluric and relative flux calibrated spectra from each observational block are normalized by the median value. All of the normalized data points from each observational block are combined, reordered by wavelength, and binned down to 512 pixels using a weighted average. The ratios of the "before" and "after" calibrators are reordered and binned down using the same weights. The final normalized spectra for VHS 1256 b and PSO 318.5 along with the telluric calibration ratios are shown in Figure 2.3.

2.2.6 Absolute Flux Calibration

Unlike A-type stars, brown dwarfs are not well approximated by a black body due to absorption from various molecules. Therefore it is not appropriate to scale a normalized spectrum by a photometry point at the effective wavelength of a given filter. To find a better scale factor(D) to multiply the normalized science spectrum by, we first solve for the total number of photons through a filter (and sky transmission if necessary) for a flux calibrated Vega spectrum (Rieke et al., 2008) and the normalized science spectrum.

The total number of photons(N) measured within a filter covering a wavelength range from λ_1 to λ_2 can be approximated by

$$N \propto \sum_{\lambda_1}^{\lambda_2} \frac{F_\lambda T_\lambda A \tau_{exp} \lambda \Delta\lambda}{hc} \tag{2.1}$$

where h and c are the Planck constant and the speed of light respectively. The transmission through the sky and/or telescope is T_λ, the area of the telescope aperture is A, and the exposure time of the measurement is τ_{exp}.

For one instrument configuration, the ratio of counts from the normalized science target and Vega should be proportional. The scale factor D is then equal to

$$D = \frac{N_{sci}}{N_{Vega}} \frac{\sum_{\lambda_1}^{\lambda_2} F_{\lambda,Vega} T_\lambda \lambda \Delta\lambda_{Vega}}{\sum_{\lambda_1}^{\lambda_2} F_{\lambda,sci} T_\lambda \lambda \Delta\lambda_{sci}} \tag{2.2}$$

The ratio of science counts to Vega counts can be calculated using the magnitude of the science target within a given filter. To calculate the number of photons that pass through the sky (if relevant) and a filter, the transmission curves are binned down to the resolution of the spectra and then interpolated onto the same wavelengths.

The VHS 1256 b L band spectrum is flux calibrated using the Subaru Infrared Camera and Spectrograph (IRCS) L' photometry point from Rich et al. (2016). PSO 318.5 has a Wide-field Infrared Survey Explorer (WISE) (Wright et al., 2010) W1 photometry point, but the W1 filter transmits light blueward of the L band spectra. Flux calibrating the PSO 318.5 L band spectrum is not possible without making assumptions about the continuum shape, therefore the scale factor (D) is allowed to be offset by up to 10% while model fitting.

2.3 Analysis

2.3.1 Detection and Significance of Methane in L band Spectra

Methane is predicted to be the only significant absorber across the L band for ~1300K objects (Morley et al., 2014). Methane absorption becomes deeper and broader through the L to T transition, especially around the Q - branch band head of methane that peaks in opacity at ~ 3.3 μm (Noll et al., 2000; Cushing et al., 2005; Kirkpatrick, 2005). VHS 1256 b and PSO 318.5 have features around ~3.3 μm that resemble absorption from methane. Despite their cool photospheric temperatures, these features appear shallow relative to other late L dwarfs and early T dwarfs (Figure 2.4). Unlike field L dwarfs, the spectral slopes of VHS 1256 b and PSO 318.5 show increasing flux density at longer wavelengths along the L band. These slopes resemble the spectral shapes of the T dwarfs, but with less methane absorption.

We provide evidence for the methane detection by showing that a best fit line to the data from 3.2 μm - 3.4 μm produces a worse fit than a simple two-line model with a break at the characteristic wavelength (λ_0) over the same wavelength range. A two-line model does not accurately represent the complex absorption feature of methane, but we want to rule out a smooth continuum before comparing to models with varying methane abundances later in Section 2.4.3. Methods that quantify absorption, such as the equivalent width or spectral indices require knowledge of the continuum and that is difficult to account for across the L to T transition as methane absorption gets broader. The 3.2 μm - 3.4 μm range was chosen for fitting, because that is where methane absorption appears most consistent from the mid-L to mid-T dwarf range (Figure 2.4). The two-line model $y(\lambda)$ is described by the function

$$y(\lambda) = \left\{ \begin{array}{lll} m_1\lambda + b_1 & for & \lambda \leq \lambda_0 \\ m_2\lambda + b_2 & for & \lambda > \lambda_0 \end{array} \right\} \tag{2.3}$$

and the coefficients are fit using the Markov Chain Monte Carlo (MCMC) method with the python package `emcee` (Foreman-Mackey et al., 2013). An example of the two-line model can be seen in the best fit for PSO 318.5 in Figure 2.5.

The relative model quality of the one and two-line best fits were assessed by a $\Delta\chi^2$ value and the Akaike Information Criterion (AIC). The difference between the one and two-line best fit χ^2 values produce a $\Delta\chi^2$ value of 74.6 and 100.3 for VHS 1256 b and PSO 318.5 respectively. For VHS 1256 b, the best fit two-line model has an AIC of 159.0 and the one-line model has an AIC of 227.7. For PSO 318.5, the best fit two-line model has an AIC of 181.4 and the one-line model has an AIC of 275.7. For both objects, the two-line model produces a lower AIC and a better quality fit to the data.

The depth parameter (ΔF) is a derived quantity from the two-line model that is the difference between $y_1(\lambda_0)$ and $y_2(\lambda_0)$. A higher value of ΔF corresponds to a deeper absorption feature. The posterior distributions of the depth parameter for VHS 1256 b and PSO 318.5 are compared with two L dwarfs, 2MASS J1507-1627 and DENIS J0255-4700, featured in Figure 2.6. Two other brown dwarfs, 2MASS J1439+1929 (L1) and 2MASS J1506+1321 (L3) are also plotted for reference. The mean values of ΔF for VHS 1256 b and PSO 318.5 are inconsistent with a straight line ($\Delta F = 0.0$) by 10.5σ and 13.3σ respectively. Nearly the entire probability distribution of VHS 1256 b and PSO 318.5's ΔF parameter lies in between the distributions of the 1700K (L5) brown dwarf and the 1500K (L8) brown dwarf. This quantitatively shows that VHS 1256 b and PSO 318.5 have methane, but show less methane absorption than hotter brown dwarfs. There is significant overlap between the ΔF distributions of VHS 1256 b and PSO 318.5, but the mean ΔF of VHS 1256 b is slightly higher.

The depleted methane features of VHS 1256 b and PSO 318.5 are evidence for non-equilibrium chemistry. Previous work has shown that vertical mixing can displace methane from the photosphere with warmer, carbon monoxide dominated gas (Hubeny & Burrows, 2007; Zahnle & Marley, 2014). In Section 2.3.3, we further quantify VHS 1256 b and PSO 318.5's methane absorption features and estimate the magnitude of their vertical mixing using custom atmospheric models.

2.3.2 Published Optical/ Near Infrared Studies of VHS 1256b and PSO 318.5

VHS 1256 b and PSO 318.5 both have optical to mid-infrared photometric measurements and near infrared spectra that have been published. For our analysis, we applied the absolute flux calibration outlined in Section 2.2.6 to the normalized near infrared spectra of VHS 1256 b and PSO 318.5 from Gauza et al. (2015) and Liu et al. (2013). The normalized optical/near infrared spectrum from Gauza et al. (2015) is broken up into optical/J, H, and K portions that are flux calibrated separately using the J, H, and K VISTA InfraRed CAMera (VIRCAM) photometry. Two near-infrared spectra of PSO 318.5 were presented in Liu et al. (2013), but for this work we do our analysis with the Gemini Near-Infrared Spectrograph (GNIRS) data because it has a higher spectral resolution. The near-infrared spectrum of PSO 318.5 was flux calibrated using the K band MKO photometry (Liu et al., 2013) measured using WFCAM on the UK Infrared Telescope.

Both objects have Two Micron All-Sky Survey (2MASS) measurements, but the 2MASS photometry is not consistent with the VISTA (VHS 1256 b) or MKO (PSO 318.5) photometry. The VISTA and MKO photometry are used for flux calibration because they produce less scatter in the final spectra when scaling by the different infrared photometry points (J, H, K) and are more precise than the 2MASS photometry. Photometric variability studies have been done on PSO 318.5 and similar objects (Biller, 2017) and this effect will be discussed later in Section 2.4.4 although we note that the measured variability cannot explain the photometric discrepancy discussed here.

2.3.3 Description of Models and Fitting

The models used to fit the data were calculated using a method similar to the one outlined in Barman et al. (2011b) with the `PHOENIX` atmospheric code and updated CH_4, CO_2, and NH_3 line lists. The intermediate cloud model (ICM) has a base pressure set by equilibrium chemistry and the vertical extent of the cloud is parameterized by a pressure value, above which the number density of cloud particles falls of exponentially. The cloud particle sizes follow log-normal distribution characterized by a median grain size. The composition of the cloud is dependent on equilibrium chemistry, resulting in clouds composed primarily of silicates (Ex. Enstatite ($MgSiO_3$), Forsterite ($MgSiO_4$)).

A grid similar to Barman et al. (2011b) was used to fit the parameters of VHS 1256 b and PSO 318.5 to confirm that the inferred temperatures and gravities were similar to previous studies on these two objects. Vertical mixing is parameterized by the vertical eddy diffusion coefficient K_{zz} which is defined as

$$K_{zz} = \frac{L^2}{\tau_{dyn}} \tag{2.4}$$

where τ_{dyn} is the dynamical time scale and L is the length scale of diffusion. The length scale in this work is approximately a third of the pressure scale height as outlined in Smith (1998).

Another model grid with slightly finer parameter sampling was created spanning an effective temperature of 1000 K to 2000 K (every 50 K), log(g) from 3.0 - 4.0

(every 0.25 decs), mean grain sizes of (0.5, 1, 2, 3 and 5 μm) and 5 different cloud heights. The abundances of these models are assumed to be solar according to Asplund et al. (2009). After an initial best fit was found using χ^2 values, the cloud distribution, effective temperature and CH_4 mixing ratio above the quenching point was tuned for a better fit.

The best fit model for PSO 318.5 also applies to VHS 1256 b because the objects share similar spectral features. The best fit model has its structure shown in Figure 2.7 and the spectrum is shown along with the data in Figure 2.8. VHS 1256 b and PSO 318.5 each have a best fit temperature of 1240 K and a best fit K_{zz} of 10^8 cm^2 s^{-1}. Above the quenching point, the mixing ratio of CH_4 was increased by two orders of magnitude to $2.4 * 10^{-6}$ for PSO 318.5 and $3.5 * 10^{-6}$ for VHS 1256 b to get a better fit. From about 1 to .1 bar, the abundance of CH_4 is two orders of magnitude higher in the best fit non-equilibrium case than the equilibrium case. Above .1 bar, the best fit non-equilibrium model has one to two orders of magnitude less methane than the equilibrium case (Figure 2.8, Middle Panel). The photospheres have clouds with a median grain size of 0.5 μm. An increased CH_4 mixing ratio also implies that a model with a smaller K_{zz} value could also explain the spectra.

With an assumed distance of 22 pc (Liu et al., 2016), the inferred radius of PSO 318.5 is 1.3 R_{Jup}, which is consistent with PSO 318.5 being a young planetary mass object (Baraffe et al., 1998). With an assumed distance of 17 pc (Stone et al., 2016), the implied radius of VHS 1256 b is 0.9 R_{Jup}, which is inconsistent with youth (Baraffe et al., 1998). The parallax and photometric distance estimates of the binary

Object	**T$_{eff}$** **(K)**	**log(g)**	**Radius** R$_{jup}$	**K$_{zz}$** cm^2 s$^-1$	**Ref**
VHS 1256 b	**1240**	**3.2**	**0.9**	**10^8**	**1**
VHS 1256 b	800 - 1000	3.5 - 4.5	1.34 - 1.8	N/A	2,3
PSO 318.5	**1240**	**3.2**	**1.3**	**10^8**	**1**
PSO 318.5	1210	4.21	1.40	N/A	2
HR 8799 c	1100	3.5	1.40	10^8	5
HR 8799 d	1100	3.5	1.40	10^8	5
2M1207 b	1000	4.0	1.5	10^8	6

Table 2.2: The atmospheric properties of VHS 1256 b, PSO 318.5, and other low gravity brown dwarfs and exoplanets for comparison. The adopted parameters of this work are bolded. The distance of VHS 1256 b is not well constrained therefore a range of parameters are presented for previously published work. The parameters for HR 8799 c and d are from the grid that gave the best fit for data across the 3μm - 5μm range in Greenbaum et al. (2018). References: 1 - this work, 2 - Liu et al. (2013), 3 - Rich et al. (2016), 4 - Gauza et al. (2015), 5 - Greenbaum et al. (2018), 6 - Barman et al. (2011b).

host are discrepant(Stone et al., 2016), therefore there is large uncertainty on the actual radius of VHS 1256 b. VHS 1256 b has very similar spectral features as PSO 318.5 and to get a similar radius, VHS 1256 b could possibly be as far as 20 parsecs. If VHS 1256 b is actually at 20 parsecs, its place on the color magnitude diagram would move up closer to the absolute magnitude of PSO 318.5. Constraints on the distance and age of VHS 1256 b will allow for evolutionary constraints and a comparative analysis on the atmospheric properties and evolution of red, dusty objects. A summary of our best fit and previously published parameters for VHS 1256 b and PSO 318.5 are shown in Table 2.2, along with parameters for similar objects.

2.4 Discussion

2.4.1 Strong Vertical Mixing in VHS 1256 b and PSO 318.5

In Section 2.3.1 we showed that VHS 1256 b and PSO 318.5 have less L band methane absorption than similar temperature brown dwarfs. This is evidence that their photospheres are not in chemical equilibrium. Strong vertical mixing can lower the amount of methane visible in the infrared spectra of low-gravity brown dwarfs and exoplanets (Hubeny & Burrows, 2007; Barman et al., 2011b, 2015). Methane's cross section per volume peaks at 3.3 μm, therefore L band spectra provide excellent constraints on methane abundances and vertical mixing.

A relatively high eddy diffusion coefficient was needed in our models ($K_{zz} = 10^8$ cm^2 s^{-1}) to match the depths of the 3.3 μm methane features. Assuming mixing length theory and that all of the convective flux from heat transport is contributing to mixing, the upper limit on K_{zz} is expected to range from 10^8 cm^2 s^{-1} - 10^9 cm^2 s^{-1} for low gravity, self luminous, gas giant planets (Zahnle & Marley, 2014).

2.4.2 Comparison with 3 μm - 4 μm photometry of HR 8799 c and d

As color-magnitude analogs of HR 8799 c and d, the spectra of VHS 1256 b and PSO 318.5 provide insight into the methane abundances and vertical mixing of these exoplanetary atmospheres. Using L/M band mid-InfraRed Camera (LMIRcam) on the Large Binocular Telescope, Skemer et al. (2014) took adaptive optics corrected images of the HR 8799 system in six different custom narrow band filters. The images resulted in 3 μm to 4 μm photometry of HR 8799 c and d. The NIRSPEC L band spectra of VHS 1256 b and PSO 318.5 are convolved with the filters used in Skemer et al. (2014) to get synthetic photometry for comparison with HR 8799 c and d. In Figure 2.9, we show the normalized photometry of VHS 1256 b, PSO 318.5, HR 8799 c and d, along with 2MASS J0559-1404, a ∼1000 K, T5 brown dwarf. The photometry for VHS 1256 b, PSO 318.5, HR 8799 c and d are relatively flat, but there are slight differences. The spectral slopes of HR 8799 c and d start to decrease in flux past the 3.59 μm photometry point, whereas the spectral slopes for VHS 1256 b and PSO 318.5 increase across the entire L band. This may be due to slightly different cloud or temperature-pressure properties between these objects. Across 3.31 μm, the spectral slopes of VHS 1256 b and PSO 318.5 appear as straight lines due to their weak methane signatures. HR 8799 c and d show a slight depression at the 3.31 μm photometry point, which indicates that they may have more photospheric methane and weaker vertical mixing than VHS 1256 b and PSO 318.5. VHS 1256 b, PSO 318.5 and HR 8799 c and d all have less methane absorption relative to 2MASS J0559-1404 despite having similar photospheric temperatures, which indicates that all four objects are out of chemical equilibrium. In previous work by Hinz et al. (2010) and Skemer et al. (2014), non-equilibrium chemistry and photospheric clouds were needed to fit the near infrared and mid infrared photometry of the HR 8799 c and d and our model analysis on analogs VHS 1256 b and PSO 318.5 is consistent with this view.

2.4.3 Using L Band spectroscopy for Detecting Methane in Exoplanets and Brown Dwarfs

If strong vertical mixing is present on numerous young, gas giant exoplanets, L band spectroscopy will be able to measure methane abundances for a wider range of objects at L to T transition temperatures than near-infrared spectroscopy alone. The best fit model from Section 2.3.3 was calculated with different CH_4 mixing ratios above the quenching point. For each of those models, we calculated three separate reduced χ^2 values only considering spectra within the MKO H band, MKO K band, and the extent of our L band data. In Figure 2.10, the reduced χ^2 value versus CH_4 mixing ratio is plotted for the H, K, and L band data of VHS 1256 b and PSO 318.5. The L band produces a more prominent local minimum along the methane mixing ratio curve than the H and K bands, showing that methane was detected and the abundance in VHS 1256 b and PSO 318.5 can be constrained.

The methane feature at $\sim$3.3 μm eventually blends in with the continuum at very low abundances when observed at lower resolutions (Figure 2.11). Future L band observations that will study methane at similarly low abundances need to be done at resolutions of $\sim$200 or higher in order to detect methane. Medium to high resolution slit spectroscopy of isolated or wide companion brown dwarfs can be done from the ground at L band with a number of instruments on medium to large sized telescopes (e.g. NIRSPEC, SpeX, iSHELL, CRIRES, and GNIRS McLean et al., 1998; Rayner et al., 2003, 2016; Kaeufl et al., 2004; Elias et al., 2006)). Present-day integral field units that are focused on finding and characterizing exoplanets in the glare of their host stars mostly operate blueward of L band (e.g. SPHERE, GPI, CHARIS Beuzit et al., 2008; Macintosh et al., 2014; Groff et al., 2017). Currently there is one exoplanet imaging IFU (ALES Skemer et al., 2015) capable of low-resolution L band spectroscopy. Higher spectral resolutions at L band are possible with lenslet and lenset/slicer integral field units (Skemer et al., 2018). Fiber injection units can be placed behind high contrast imaging systems to obtain even higher spectral resolutions of exoplanets (Wang et al., 2016; Mawet et al., 2017).

2.4.4 Future JWST Observations

The *James Webb Space Telescope* will be able to obtain high-fidelity spectra of brown dwarfs across a broad wavelength range, including L band. JWST can constrain the abundances of important secondary gases (e.g. H_2O, CO, CH_4, NH_3) for the entire temperature range of known brown dwarfs (Lodders & Fegley, 2002). Medium resolution spectra over a broad wavelength range will be critical for adequately defining and measuring the C/O ratios and metallicities for brown dwarfs and exoplanets. There is evidence for silicate condensates in L to T transition objects from *Spitzer* observations (Cushing et al., 2006) and it may be possible to determine the phase and composition of these silicates with Mid-Infrared Instrument (MIRI) spectra. Direct studies of condensates are important for testing our assumptions about clouds and the extent to which other physical effects (ex. temperature instabilities, cloud microphysics) significantly influence the atmospheres of brown dwarfs and exoplanets. (Tremblin et al., 2017; Leconte, 2018; Charnay et al., 2018).

Combining data from different epochs (as done in this work) may not accurately represent the average state of an atmosphere and introduces flux calibration errors. Most brown dwarfs with time series photometric measurements appear variable at the few percent level and rotate on the order of hours (Biller, 2017). PSO 318.5 has a measured variability of 3 - 4 % percent in several bands across the 1 μm - 5 μm range and these variations are suggested to be due to inhomogeneous cloud layers (Biller et al., 2015, 2018). No time series observations have been taken of VHS 1256 b. The MKO and 2MASS J, H, and K /K_s near infrared photometry for PSO 318.5 are different by $\sim$35, $\sim$9, and $\sim$23 percent respectively. The same is also true for the VISTA and 2MASS J, H, and K photometry of VHS 1256 b, which are different by $\sim$37, $\sim$13, and $\sim$3 percent respectively. The photometry of both objects are not completely inconsistent due to low signal to noise, however they can lead to different colors and flux calibrations. This ultimately influences our interpretation of the atmospheric and evolutionary properties of both objects. JWST's Near-Infrared Spectrograph (NIRSPEC) sensitivity enables contemporaneous coverage over the 1 μm - 5 μm wavelength range, making spectroscopic monitoring of brown dwarfs feasible. Contemporaneous and precise, medium resolution data of VHS 1256 b and PSO 318.5 will provide better constraints on the average effective temperature and other atmospheric properties of both objects.

2.4.4.1 High Contrast Imaging of Exoplanets and Exoplanetary Early Release Science Program

The High Contrast Imaging of Exoplanets and Exoplanetary Systems with JWST Early Release Science (ERS) Program will utilize all of JWST's instruments to provide a useful data set for the astonomical community to assess JWST's ability to execute observations of exoplanetary systems (Hinkley et al., 2017). VHS 1256 b is the first choice target for NIRSPEC and MIRI integral field unit (IFU) mode observations that will provide the first medium resolution (R $>$ 1,000), 0.7 μm - 28.0 μm spectrum of an exoplanet analog.

The ERS spectrum will detect the majority of VHS 1256 b's luminosity, important carbon, oxygen, and nitrogen bearing gases, and silicate condensates if present. The resolution of the ERS spectrum is sufficient for detecting the methane features presented in this work and other minor/low abundance molecular absorbers. The spectrum will be able to constrain all of the important carbon and oxygen bearing gases required to make an estimate for the C/O ratio of VHS 1256 b.

For gaseous Solar System planets, the K_{zz} profile of an object may change relatively quickly over a scale height or yield different results depending on which non-equilibrium gases are measured (Smith, 1998; Lellouch et al., 2002). NIRSPEC and MIRI measurements of CO and CH_4 at multiple wavelengths can test the strength and vertical extent of K_{zz} along an assumed pressure vs. temperature profile for VHS 1256 b. The ERS spectrum will be an enormous leap in the quality of data we have to study a directly-imaged exoplanet analog, and will allow us to test, compare, and improve the array of models and retrievals used to characterize the atmospheres of brown dwarfs and exoplanets.

2.5 Summary and Conclusions

Low gravity objects like 2MASS 1207 b and the HR 8799 planets appear redder on the color magnitude diagram relative to field brown dwarfs. Their near infrared spectra lack strong signatures of methane hinting that these atmospheres are out of chemical equilibrium. This non-equilibrium chemistry can be explained by vertical mixing exchanging warm carbon monoxide-rich gas with cool methane-rich gas. The opacity of methane is greatest within the L band and dominates over other secondary gases such as carbon monoxide and water, making it an excellent wavelength region for constraining methane in low gravity L to T transition objects.

In this work, we detect methane in R ∼1,300 L band spectra of the planetary mass companion VHS 1256 b, and the young, free floating planetary mass object PSO 318.5, which share the same color space as the HR 8799 planets. The L band spectra of these two objects provide an early look into the composition and cloud properties of self luminous, gas giant exoplanets that we may characterize with large ground based telescopes in the future.

The results of this paper are:

- We detect low abundances of CH_4 in L band spectra of VHS 1256 b and PSO

318.5. Both objects have spectral slopes that are relatively flat, similar to the 3 μm - 4 μm photometry of HR 8799 c and d featured in Skemer et al. (2014). HR 8799 c and d have deeper troughs through 3.3 μm, suggesting that these planets have more methane and/or less vertical mixing than VHS 1256 b and PSO 318.5.

- The reduced quantities of CH_4 detected in VHS 1256 b and PSO 318.5 suggest non-equilibrium chemistry between CO and CH_4. The upper atmospheres of the best fit models depart from equilibrium abundances of CH_4 by factors of 10 - 100. An eddy diffusion coefficient (K_{zz}) of 10^8 cm^2 s^{-1} is required to match the depths of the 3.3 μm CH_4 features.

- The best fit model to VHS 1256 b and PSO 318.5 is a low gravity, 1240K object, with photospheric clouds. This model produces a reasonable radius for PSO 318.5 that is consistent with evolution models (Baraffe et al., 1998). VHS 1256 b's spectrum looks remarkably similar to PSO 318.5, however, its uncertain distance manifests as an unconstrained radius. Future distance and age measurements will be able to connect these objects and others from an evolutionary standpoint.

- Medium resolution, L band spectroscopy can detect low abundances of CH_4 at 3.3 μm even when the CH_4 abundances are too low to be detectable at 1.6 μm in medium resolution H band spectra. For objects similar to VHS 1256 b and PSO 318.5, a R $\sim$ 200 is necessary to detect CH_4 at L band.

All known directly imaged exoplanets fall within the temperature range of brown dwarfs. A handful of brown dwarfs even share the same infrared colors as exoplanets and they are incredibly useful laboratories for studying the variety of atmospheric abundances and processes that are likely to be seen on gas giant exoplanets.

After my first two years of grad school I needed to start learning how to pour into myself more and take mental breaks from work. Despite being from Los Angeles, I never learned how to swim and I figured grad school was the time to get over my fear of the water with PE classes. I am by no means a great swimmer, but I'm glad I conquered a fear and swimming/working out is one of the few times my mind feels at rest.

"It's a full-time job fuckin loving yourself"

- Junglepussy, Bling Bling, *Satisfaction Guaranteed*

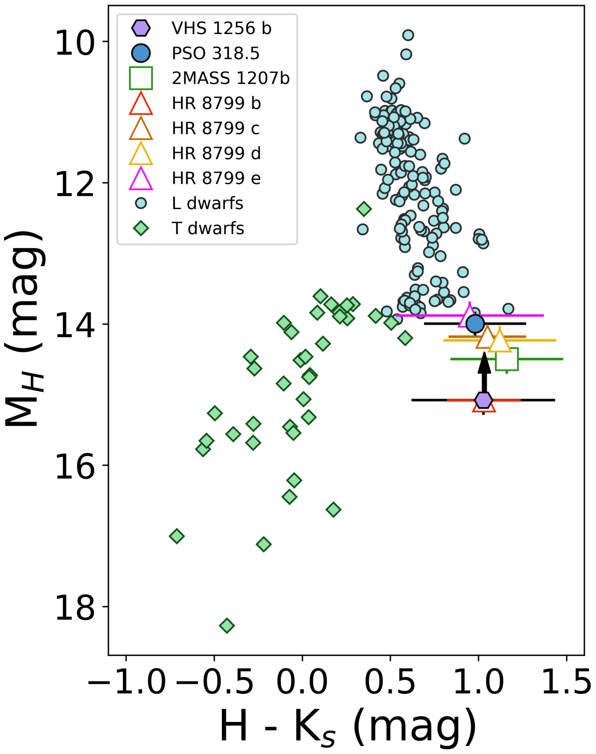

Figure 2.1: Color magnitude diagram of L (blue circles) and T (light green diamonds) dwarfs using measured and synthesized 2MASS magnitudes compiled in Dupuy & Liu (2012). The HR 8799 planets are plotted as triangles with colored edges (Marois et al., 2008, 2010; Metchev et al., 2009; Skemer et al., 2012). 2MASS 1207 b, a very young, low mass companion, is plotted as a square with green edges (Chauvin et al., 2004). VHS 1256 b is plotted as a lavender hexagon and PSO 318.5 is plotted as a blue circle. The distance of VHS 1256b is not well constrained, therefore the black arrow represents a range of possible absolute magnitudes.

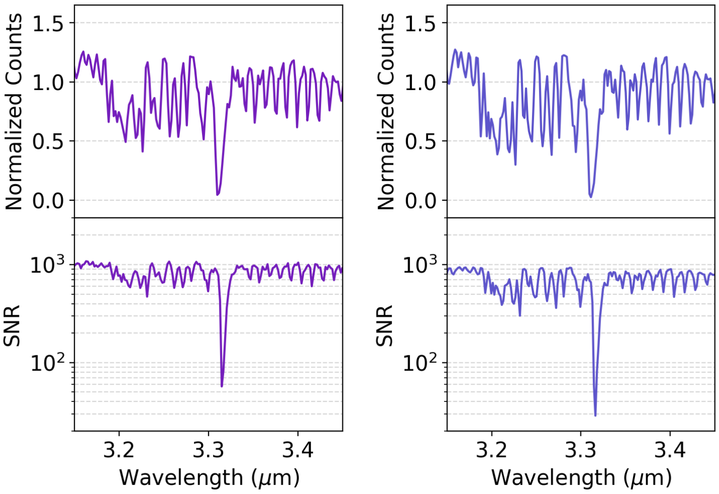

Figure 2.2: Top: The average telluric spectra for VHS 1256 b (left) and PSO 318.5 (right), centered on the peak of the Q-branch (3.3 μm) methane feature. Bottom: The signal to noise of the average telluric spectra for VHS 1256 b (left) and PSO 318.5 (right). At 3.31 μm, the atmospheric transmission is fairly low, however the telluric spectra have a signal to noise of 57 and 29, respectively in these troughs.

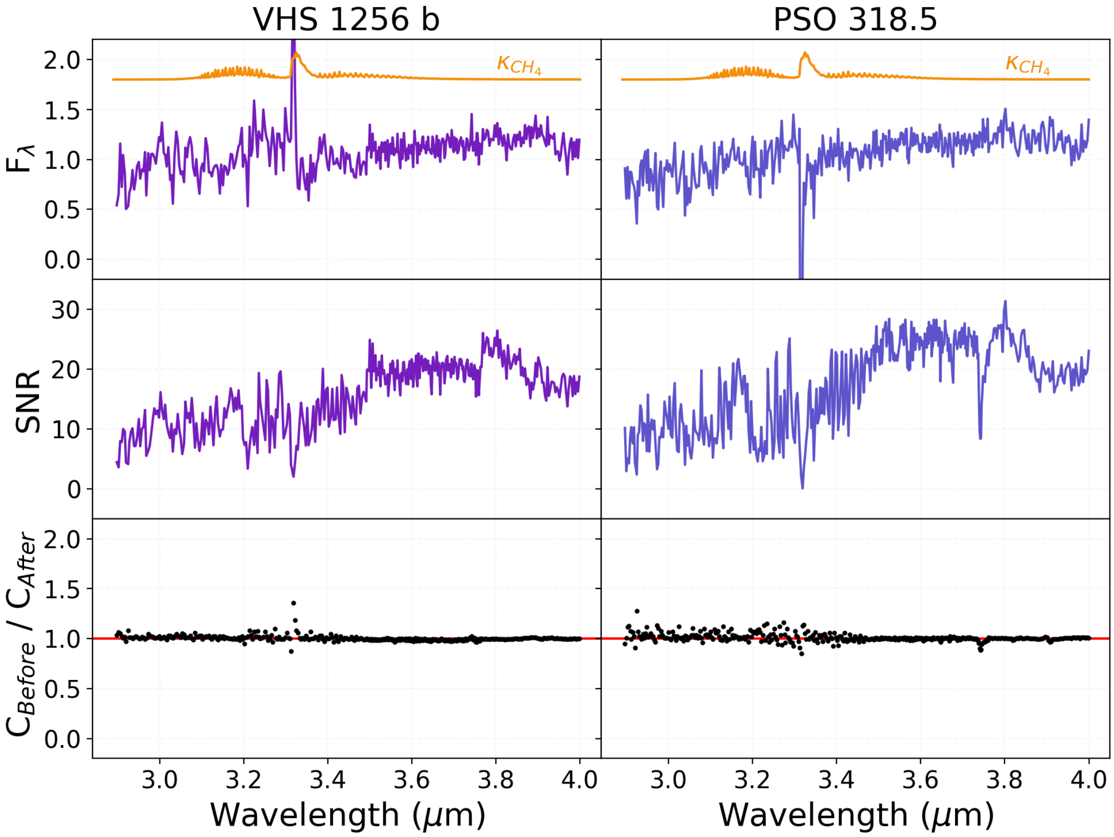

Figure 2.3: Top: Normalized flux (F_λ) plotted against wavelength for VHS 1256 b and PSO 318.5. The opacity of methane is plotted in orange above the spectra in arbitrary units on a linear scale. There is absorption from methane at ~3.3 μm in both objects. Middle: The signal-to-noise vs wavelength for VHS 1256 b and PSO 318.5. Bottom: The before calibrator (C_{Before}) divided by the after calibrator (C_{After}) combined for all science observations. This is a metric of the telluric calibration quality for each object. Both objects have a standard deviation of 1% over the entire spectrum. Across the peak of the methane feature (3.3 μm - 3.4 μm), the standard deviation of the telluric ratio is 8% for VHS 1256 b and 5% for PSO 318.5. The telluric ratio deviations are included in our error propagation and reflected in the errors for the signal-to-noise plots in the middle panel.

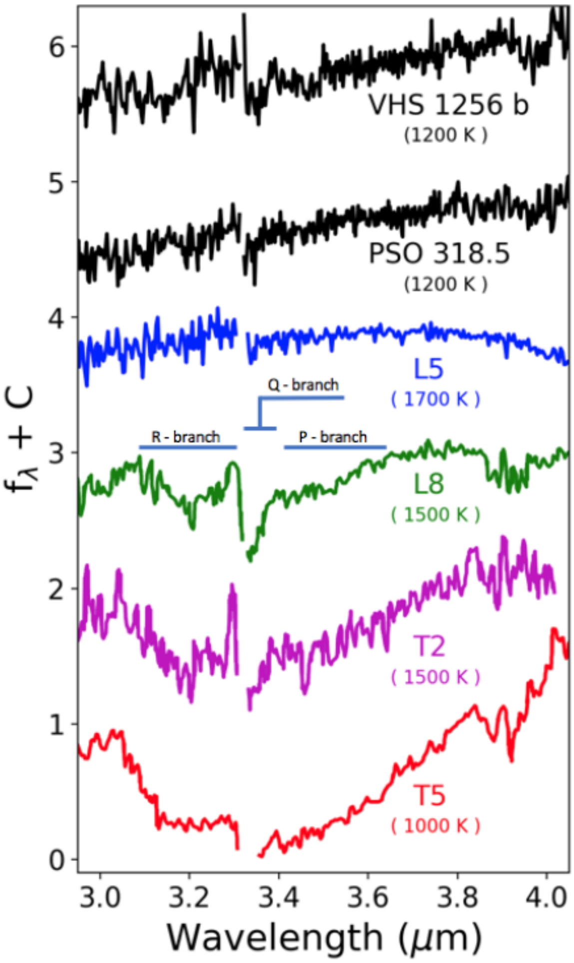

Figure 2.4: Normalized spectra of VHS 1256 b and PSO 318.5 (with SNR < 3 data points removed) along with L band spectra of 2MASS J1507-1627 (L5), DENIS J0255-4700 (L8), SDSS J1254-0122 (T2), and 2MASS J0559-1404 (T5) from Cushing et al. (2005). All of the spectral type identifications were done in the near infrared. Each spectrum is normalized at 3.8 μm and offset by an arbitrary constant. The best fit temperature estimate for VHS 1256 b is from Rich et al. (2016), for PSO 318.5 the estimate is from Liu et al. (2013). The temperatures of the brown dwarfs from Cushing et al. (2005) are estimated using the temperature vs. spectral type relationship derived in Golimowski et al. (2004). The P, Q, and R branch portions of methane absorption are labeled on the L8 brown dwarf. VHS 1256 b and PSO 318.5 have weak Q-branch methane features and show less methane absorption than brown dwarfs of similar temperatures.

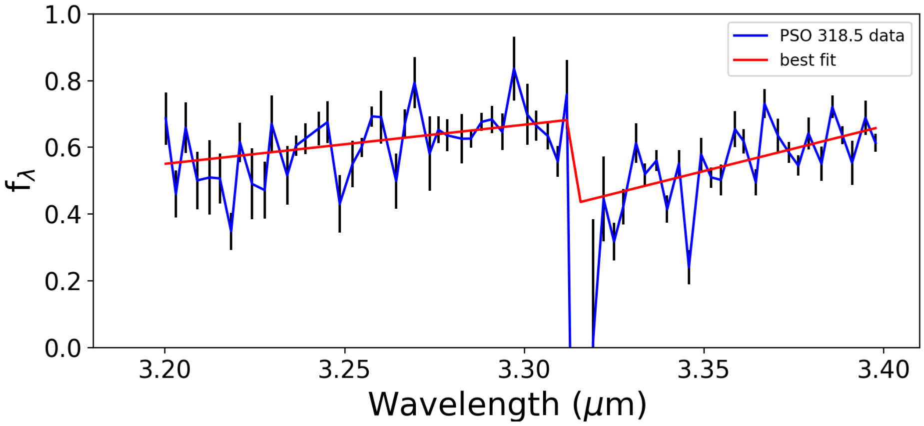

Figure 2.5: To quantify the significance of the methane absorption feature at $\sim 3.3\ \mu$m, we fit a one-line model and a two-line model with a characteristic break at λ_0 to the data of VHS 1256 b and PSO 318.5. The two-line model produces better fits to our data, showing that the absorption is statistically significant. In this figure, we show the best fit two-line model (red) to a subset of the PSO 318.5 spectrum (blue).

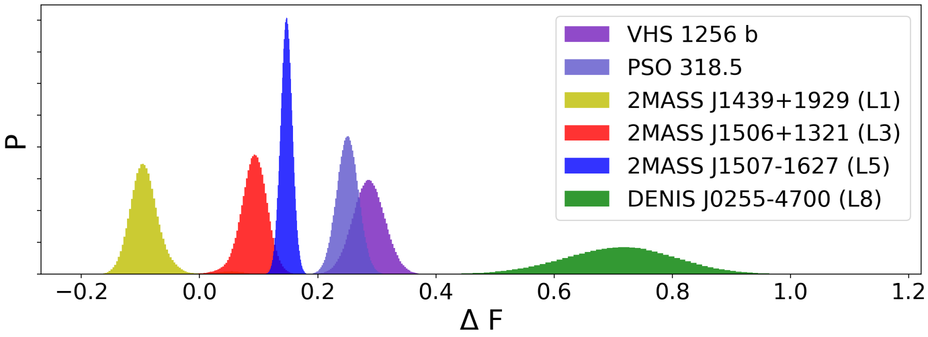

Figure 2.6: Probability distributions of the depth parameter (ΔF) for (left to right)2MASS J1439+1929, 2MASS J1506+1321, 2MASS J1507-1627, PSO 318.5, VHS 1256 b, and DENIS J0255-4700. Positive ΔF values correspond to methane absorption. The mean values for each distribution (left to right) are -0.02, 0.09, 0.15, 0.25, 0.34, and 0.66. VHS 1256 b and PSO 318.5 have methane absorption distributions that are intermediate between the distributions of 2MASS J1507-1627 (1700K) and DENIS J0255-4700 (1500K).

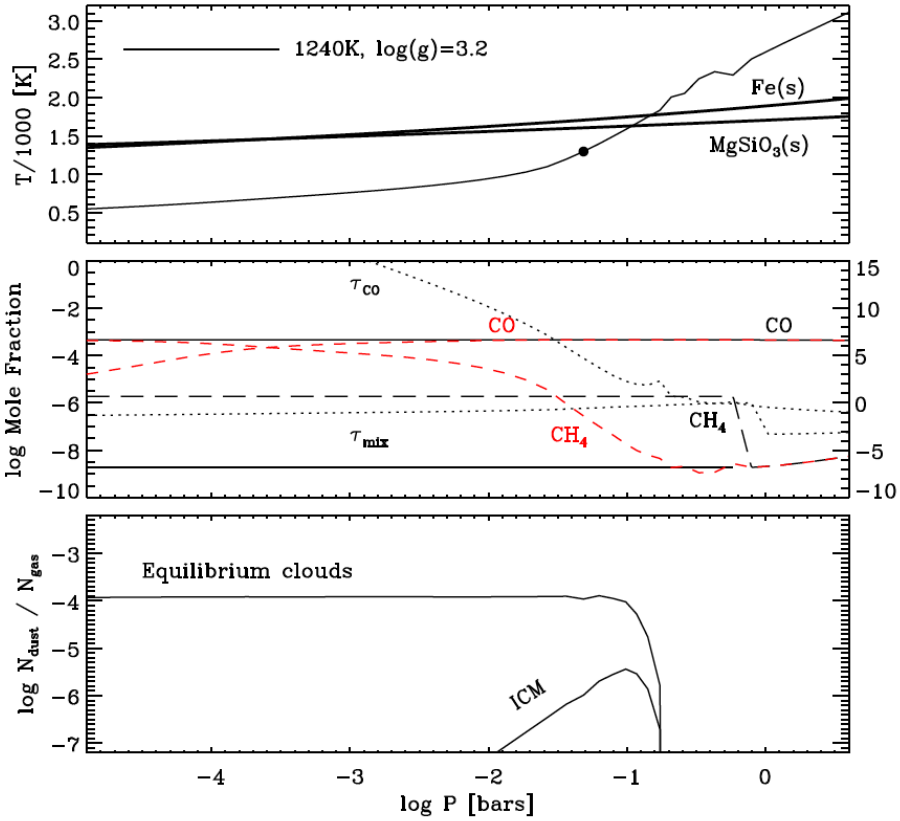

Figure 2.7: Atmospheric properties for VHS 1256 b and PSO 318.5. Top: Temperature versus pressure profile. The black dot approximates the location of the photosphere and the condensation curves of Enstatite ($MgSiO_3$) and Iron (Fe) are represented as thick black lines. Middle: CO and CH_4 mole fractions for equilibrium (dashed, red), non-equilibrium (solid, black, with K_{zz} of 10^8 cm^2 s^{-1}) chemistry, and best fit non-equilibrium with enhanced CH_4 (dashed, black, with K_{zz} of 10^8 cm^2 s^{-1}). Chemical and mixing timescales are also plotted (dotted lines). Bottom: dust to gas ratio for the intermediate cloud model (ICM), used for the best fit and the pure equilibrium cloud model.

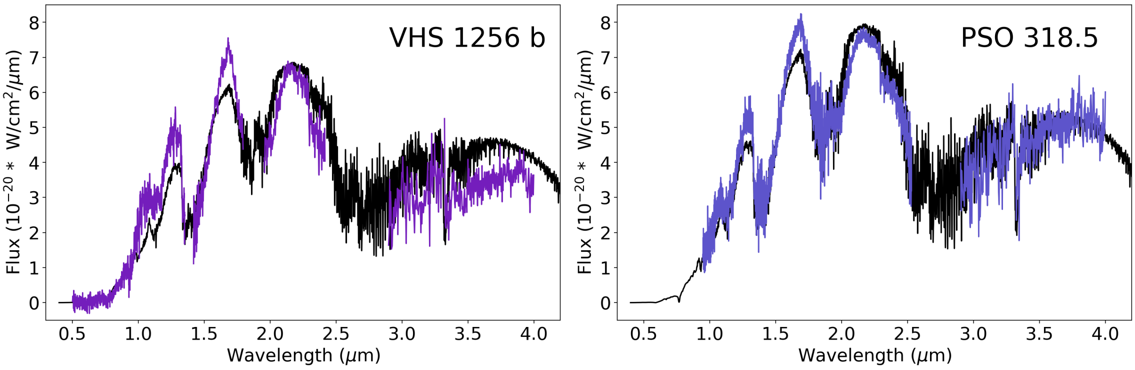

Figure 2.8: Near infrared and L band spectra for VHS 1256 b and PSO 318.5. The near infrared spectra for VHS 1256 b and PSO 318.5 are from Gauza et al. (2015) and Liu et al. (2013). The best fit, low gravity (log(g) = 3.2), 1240 K model is shown in black in both panels.

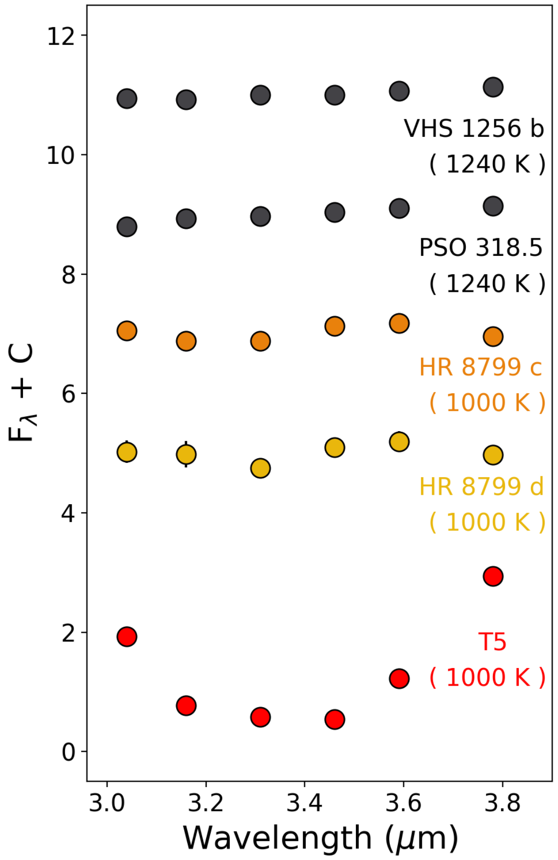

Figure 2.9: The top data points(black) are normalized 3 μm - 4 μm photometry of VHS 1256 b and PSO 318.5 calculated using the narrow band filter profiles from Skemer et al. (2014). The temperatures of VHS 1256 b and PSO 318.5 are now derived from our model fits. The narrow band filter photometry for HR 8799 c and d are from Skemer et al. (2014) and are plotted as orange and yellow points. The narrow band photometry of 2MASS J0559-1404 (featured in Figure 2.4, from Cushing et al. (2005)) is plotted in red. Relative to VHS 1256 b and PSO 318.5, HR 8799 c and d show deeper absorption at the 3.31 μm photometry point, which suggests that they may have stronger methane absorption. However, the absorption is still more shallow than seen in the similar temperature brown dwarf 2MASS J0559-1404, indicating that the HR 8799 c and d atmospheres are out of chemical equilibrium.

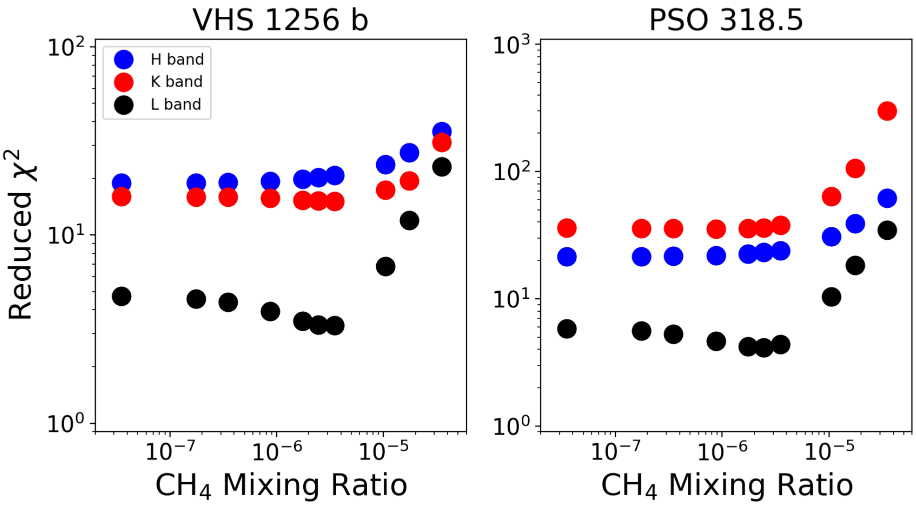

Figure 2.10: Reduced χ^2 value as a function of the CH$_4$ mixing ratio for spectra within the MKO H band (in blue), MKO K band (in red), and our L band spectra (black). The L band curve has a more prominent local minimum that is not clearly seen at either H or K band, allowing for the CH$_4$ abundances to be constrained on VHS 1256 b and PSO 318.5. The models used for this analysis are the best fit model with different CH$_4$ mixing ratios.

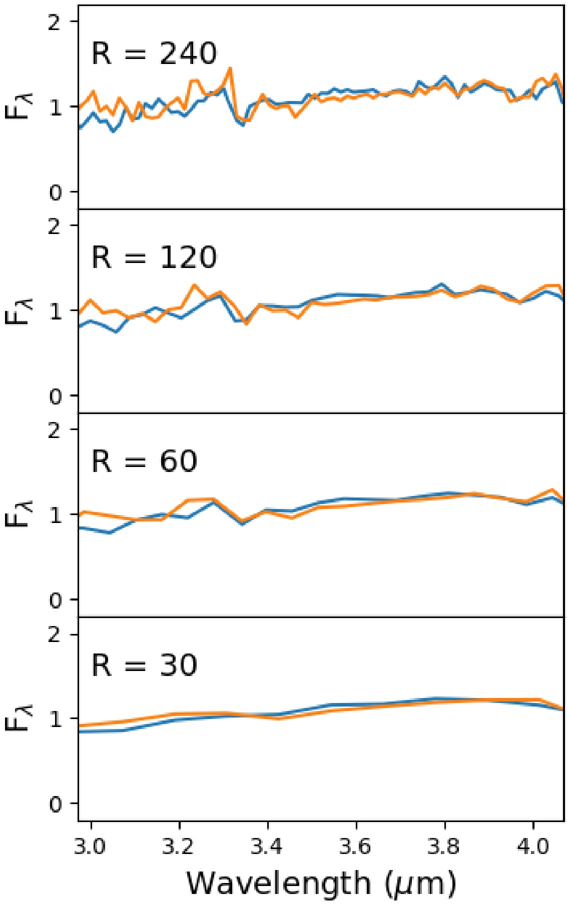

Figure 2.11: The L band spectra of PSO 318.5 (blue) and VHS 1256 b (orange) binned to different resolutions. The spectra are smoothed down with a boxcar kernel. Depending on the signal to noise of the detection, the Q-branch methane feature is hard to distinguish from the continuum below a resolution of ∼ 200.

Chapter 3

Observations of Disequilibrium CO Chemistry in the Coldest Brown Dwarfs

Studying the methane, ammonia, and water rich atmospheres of late T and early Y- type brown dwarfs is an endeavour that both challenges and improves our understanding of physics and chemistry within the atmospheres of gaseous objects. All current directly imaged planets fall somewhere within the effective temperature range of known brown dwarfs (Faherty et al., 2016; Bowler, 2016); the coldest brown dwarfs can be used to forecast the spectroscopic features in colder gas giants we may detect with future direct imaging surveys. We want to know what gas giant planets are made of, how they form, and the processes that take place within their atmospheres. Atmospheric studies of cool brown dwarfs are key to interpreting observations of widely separated gas giant planets.

Y-dwarfs are the coldest type of brown dwarf. They were recently discovered with the *WISE* mission (Cushing et al., 2011; Kirkpatrick et al., 2012) and several efforts have been made to characterize them using photometry and spectroscopy, primarily across the near infrared. Some of the earliest spectroscopic work by Cushing et al. (2011) and Kirkpatrick et al. (2012) showed that the near infrared absorption features of ammonia (NH_3), water (H_2O), and methane (CH_4) cause the J (1.2 μm) and H (1.6 μm) - band peaks to become narrower along the late-T to early-Y dwarf sequence. The main gaseous constituents of late-T and early-Y dwarf atmospheres are known, but atmospheric models often do not fit the available data well (Morley et al., 2014; Beichman et al., 2014; Schneider et al., 2015; Luhman & Esplin, 2016; Leggett et al., 2012, 2019b).

The bright thermal background of Earth's atmosphere makes ground-based mid-infrared (3 μm - 5 μm) observations of brown dwarfs and gas giant exoplanets challenging, however "the difficulties of observing in this part of the spectrum are outweighed by the rich variety of molecular bands that are detectable in this interval" (Noll, 1993). The 3 μm - 5 μm portion of the mid-infrared is where T- and Y- dwarfs emit the majority of their flux and several important gases such as water and methane can be detected (Burrows et al., 2003; Lodders & Fegley, 2002; Morley et al., 2014). Water absorption was detected in the M-band (4.5μm - 5μm) spectrum of the coldest brown dwarf, WISE J085510.83-071442.5 (**WISE 0855**, 250K, Luhman (2014); Skemer et al. (2016a)). Methane can be detected in both near infrared and L-band (3μm - 4μm) spectra of late T-dwarfs (e.g. UGPS 0722, Leggett et al. (2012)), but the mid-infrared becomes important for characterizing Y-dwarfs such as WISE 0855 spectroscopically

(Morley et al., 2018) because these objects emit most of their flux beyond 3μm (Beichman et al. (2014); Leggett et al. (2019b)).Water and methane can be used to estimate the overall atmospheric oxygen and carbon abundances of cool brown dwarfs (Line et al., 2015, 2017; Zalesky et al., 2019) and by extension, gas giant exoplanets that share the same effective temperatures.

Other trace species like carbon monoxide (CO), phosphine (PH_3), arsine (AsH_3), germane (GeH_4), and ammonia (NH_3) could potentially be detected between 3μm and 5μm (Morley et al., 2018), providing constraints on properties such as atmospheric mixing and abundance measurements beyond carbon and oxygen. T- and Y- spectral type brown dwarfs have methane as the dominant carbon-bearing species, but carbon monoxide gas can be brought into the methane-rich regions of the atmosphere through large scale vertical mixing (Lodders & Fegley, 2002). Disequilibrium carbon monoxide abundances have been inferred photometrically and confirmed spectroscopically in several T dwarfs providing evidence of atmospheric quenching driven by convective mixing (Noll et al., 1997; Oppenheimer et al., 1998; Saumon et al., 2003; Golimowski et al., 2004; Geballe et al., 2009; Sorahana & Yamamura, 2012; Leggett et al., 2012). The coldest T-dwarf with a disequilibrium CO detection is Gl 570 D, which has a near infrared classification as a T8 (Burgasser et al., 2006).

Phosphine is another signal of strong convective mixing that has been observed in Jupiter (126 K), but it was not seen in WISE 0855's (250 K) L or M-band spectrum (Skemer et al., 2016a; Morley et al., 2018). Jupiter and WISE 0855 are nearly similar in temperature (126 K vs 250 K), but phosphine's abundance is only quenched within

Jupiter's atmosphere. One of the goals of this work is to understand the diversity of atmospheric mixing between the parameter space of late-T dwarfs to early Y-dwarfs to giant planets.

Water clouds are predicted to be significant sources of opacity in brown dwarfs with effective temperatures below ∼375 K (Burrows et al., 2003; Morley et al., 2014). WISE 0855's M-band spectrum shows evidence of water clouds, because the spectral shape cannot be fit with a cloudless model (Skemer et al., 2016a; Miles et al., 2018). Cloudy models work well for fitting WISE 0855's normalized M-band spectra in isolation, but matching the available photometry is still an issue that could potentially be resolved with the consideration of upper atmospheric heating or other opacity sources (Esplin et al., 2016; Morley et al., 2018; Leggett et al., 2019a).

Extending the previous work of Skemer et al. (2016a) and Morley et al. (2018), we explore the atmospheric properties of seven brown dwarfs with effective temperatures covering 700 K to 250 K and Jupiter based on M-band spectroscopic data. In this study we present new Gemini/GNIRS M-band spectral observations of WISEPA J031325.96+780744.2 (**WISE 0313**, Kirkpatrick et al. (2011)), UGPS J072227.51-054031.2 (**UGPS 0722**, Lucas et al. (2010)), WISEPC J205628.90+145953.3 (**WISE 2056**, Cushing et al. (2011)), and WISEP J154151.65-225025.2 (**WISE 1541**, Cushing et al. (2011)). These new data are supplemented by previously published *AKARI* observations of **2MASS J0415-0935** and Gemini/NIRI observations of **Gl 570 D** (Sorahana & Yamamura, 2012; Geballe et al., 2009). The WISE 0855 M-band data presented in Skemer et al. (2016a) are re-reduced using the methods in this work and added to the sample. All spectra are fit better with disequilibrium CO abundances, even though methane is the dominant carbon bearing gas at these effective temperatures.

These observations address two questions: **1)** What do cool brown dwarfs look like spectroscopically across the M-band and why? **2)** Are there any trends in atmospheric quenching within this effective temperature range?

The observations and data reduction methods for the new M-band data are described in Sections 3.1 and 3.2. In Section 3.3, the M-band spectral sequence ordered by luminosity derived effective temperatures is shown. We show that equilibrium models do not adequately recreate the features of the spectra and disequilibrium abundances of carbon monoxide are needed to fit the spectra in Section 3.4. We briefly discuss the effect of carbon monoxide and clouds in WISE 0855 and WISE 1541 and their improvement of the spectral fits. In Section 3.5 we estimate the eddy diffusion coefficient for each object based on carbon monoxide abundances and make predictions for phosphine and ammonia, which are summarized in Table 3.15. Lastly we discuss the implications of this work for cold, directly imaged gas giant exoplanets that may be discovered in the future.

3.1 Observations

We obtained observations of WISE 0313, UGPS J0722, WISE 2056, and WISE 1541 over the course of a year at Gemini North (Programs GN-2016B-Q-23, GN-2017A-Q-5, GN-2017A-Q-32) using the Gemini near-infrared spectrograph (GNIRS; Elias et al.

(2006)). These observations are complementary to the M-band spectra of WISE 0855 published in Skemer et al. (2016a).

GNIRS was set up with the long camera (0.05″/pix resolution), 0.675″ slit, and deep detector well depth setting for all observations. There is uncertainty in the position of our objects due to their relatively high proper motions. We use a 13.5 pixel wide (0.675″) slit to avoid missing the objects completely when placing them in the slit. The deep well setting is needed to record more of the bright sky background without reaching non-linearity within the detector pixels. The 31.7 line mm^{-1} grating covers the M-band from 4.5 μm to 5.1 μm at an effective resolution of $\sim$ 7,400, which is eventually binned down to a resolution of $\sim$370. Each spectral image is the sum of 24 co-added 2.5 second long integrations. The total integration time was 4.2 hours for WISE 0313, 2.4 hours for UGPS 0722, 15.36 for WISE 2056, and 10.8 hours for WISE 1541.

A single observation sequence of a target consists of four spectral images in a ABBA pattern by nodding along the slit. Each block of data typically takes the following pattern:

1. Acquisition of first telluric calibrator star

2. First telluric calibrator star observation sequence.

   (1 x 24 co-adds X 2.5 seconds)

3. Acquisition of brown dwarf

4. Nine brown dwarf observation sequences.

(9 x 24 co-adds X 2.5 seconds)

5. Re-acquisition of brown dwarf.

6. Nine brown dwarf observation sequences.

   (9 x 24 co-adds X 2.5 seconds)

7. Acquisition of second telluric calibrator star

8. Second telluric calibrator star observation sequence.

   (1 x 24 co-adds X 2.5 seconds)

Every brown dwarf target was acquired by blind-offsetting from a bright, nearby star except for UGPS 0722. The position of the brown dwarf was calculated into a standard reference frame using proper motion propagation code and published parallaxes (UGPS 0722 - Kirkpatrick et al. (2012), WISE 0313 - Beichman et al. (2014), WISE 2056 - Kirkpatrick et al. (2019), WISE 1541 - Kirkpatrick et al. 2019). Every telluric calibrator is an A0 or A1 type star that is nearby and within .2 airmasses of its respective science target on the sky. The before and after calibrator stars are kept the same for an individual brown dwarf in all programs. A full breakdown of observations used for each object are listed in Tables 3.3, 3.4, 3.5, and 3.6.

3.2 Data Reduction

A single subset of spectral data consists of a telluric calibrator sequence and nine science target sequences. A subset is reduced to create two extracted science spectra. The final spectrum for each science target is the combination of all the extracted spectra from each subset of that object.

3.2.1 Spectral Images Removed from Analysis

On occasion, the Gemini NOAO Aladdin Array Controller[1] will create a checkerboard pattern visible in the A nod minus B nod (A-B) frames of calibrator and science targets. Spectral images affected by this noise are removed from the analysis. If the majority of a brown dwarf's observation sequence is affected by electronic pattern noise, it is not included in the analysis. Observations affected by electronic pattern noise are noted in the comments of Table **??**.

Despite the short integration times used for our observations, some longer-wavelength skylines still reach non-linearity. Wavelengths with count values in the non-linear range are flagged and later removed during the spectral extraction process (See Section 3.2.3). Clouds create a bright and variable sky background that eclipses the science target signal, making A-B sky subtraction useless. The 2016 - 10 - 18 observations of WISE 2056 are excluded from the analysis due to this.

3.2.2 Spectral Image Reduction

Sections 3.2 and 3.3 of Miles et al. (2018) based on the REDSPEC package (Kim et al., 2015) outline the procedure used for the sky subtraction, rectification, and wavelength solution of the spectral image data. These procedures are similar to the

---

[1] http://www.gemini.edu/sciops/instruments/gnirs/known-issues

ones used to reduce the WISE 0855 data presented in Skemer et al. (2016a). Centroids are fit along the traces of the mean A-B telluric calibrator spectral images to estimate the deviation from a straight line and create the spatial rectification map used for interpolation. Rectification maps have coefficients for each row used for one-dimensional interpolation. The spatial rectification map is applied to a mean A nod plus B nod (A+B) image of the telluric calibrator, where 12 sky lines are used to create a second rectification map for the wavelength direction. The A-B spectral images of the telluric calibrator and science target are taken to subtract most of the sky background. Each of these differenced spectral images are then interpolated using the rectification maps derived from the mean calibrator image. Excess sky remains after nod subtracting and rectifying the spectra, therefore at each row along the entire wavelength direction, the median of the pixels along the spatial direction is subtracted.

Following the ordering of the observational pattern steps listed in Section 3.1, the rectification and wavelength maps from the before telluric calibrator (Step 2) are applied to the first brown dwarf's sequence (Step 4). The rectification and wavelength maps from the after telluric calibrator (Step 8) are applied to the second brown dwarf sequence (Step 6).

The wavelength solution for each subset is calculated by fitting a second order polynomial to 13 sky emission lines along the wavelength direction of the spatially and spectrally rectified A+B calibrator images. The spectral features are identified by referencing a model of the Maunakea Sky[2] smoothed to the resolution of the data.

---

[1] numpy.interp

[2] www.gemini.edu/sciops/telescopes-and-sites/

3.2.3 Detector Non-Linearity

Earth's atmosphere has strong background emission across the M-band which can drive the detector into a non-linear regime. A very conservative approach is taken to address non-linearity on the detector for a better telluric calibration. Pixels with values in the non-linear response regime of >10,000 ADU per co-add[3] are marked in every spectral image by creating a separate non-linearity image where 0 is linear and 1 is non-linearity. These non-linearity images are also rectified using the appropriate rectification map. Interpolation causes surrounding pixels to be flagged (values above 0) in the non linear regime even if they were not originally. At most, 3.4% more pixels are flagged in the rectified non-linear maps than in the original spectral image. For a single subset (calibrator and science), the mean of all of the non-linearity maps are taken to create a final single map for the entire subset. If any pixel was flagged as non-linear over the course of a subset it is masked from the analysis.

3.2.4 Spectral Extraction and Error Estimation

After sky subtraction and rectification, a 3σ clip is made for each pixel along the stack of reduced science images in a subset to remove outliers. The mean of the reduced science image is used for extraction. The reduced mean science image is collapsed over the spatial direction by taking a mean weighted by noise in order to find the positive and negative traces of the faint science target. The boxcar extraction center

---

observing-condition-constraints/ir-background-spectra

[3] https://www.gemini.edu/sciops/instruments/gnirs/spectroscopy/detector-properties-and-read-modes

and radius (1.5852 σ)[4] of each trace are estimated by using the best-fit parameters of a Gaussian. The same extraction procedure is applied to the reduced calibrator images.

The errors are estimated by taking the variance image of a reduced stack of images and doing a boxcar extraction over the same center and widths as the respective trace. The rectified non-linear maps created for each subset (calibrator and science target pointing) are also boxcar extracted to find the wavelengths affected by non-linear pixels. If any pixel at a given wavelength within an extraction width had a non-linear response, the entire wavelength element is masked out in the final extracted spectrum.

3.2.5 Telluric and Relative Flux Calibration

Calibrator spectra of A0 and A1 stars are taken to remove the response of the telescope and Earth's atmosphere because the stellar spectra can be reproduced by a black body function across the mid-infrared. The extracted science spectra are divided by a calibrator star and then multiplied by Planck's law using the same temperature of the calibrator star. The calibrator star HIP 39898 from the WISE 0855 program (Skemer et al., 2016a) has a visible Pfund hydrogen recombination line at 4.65 μm. This line is removed prior to division by fitting a Gaussian to the feature. No calibrator stars from programs GN-2016B-Q-23, GN-2017A-Q-5, GN-2017A-Q-32 show Pfund ($7 -> 5$, 4.65 μm) or Humphreys ($11 -> 6$, 5.12 μm) hydrogen emission across the M-band.

Spectra of A0 stars are taken at the beginning and end of each observational

---

[4] http://wise2.ipac.caltech.edu/staff/fmasci/GaussApRadius.pdf

block to assess the quality of the telluric calibration. We extract the calibrator spectra taken before and after each science target observational block, normalize by the median, and then divide the before calibrator by the after calibrator. The ratio of the normalized "before" calibrator to the normalized "after" calibrator should be one, however there are deviations which are interpreted as percentage errors included in the final spectrum.

To get the final spectrum for each object, the normalized spectra from every subset are placed into a single array, then the data points are re-ordered by wavelength. The data points are then binned using an average weighted by the error to produce a 51 pixel length spectrum with a resolution of about 370 of each brown dwarf. M-band observations are background limited and binning always increases the signal-to-noise per pixel along the spectrum. The original WISE 0855 M-band spectrum was binned to 51 wavelength elements to flatten out ringing variations in the telluric ratio. The objects in this work are binned to the same amount of wavelength elements for convenience. The spectra of UGPS 0722, WISE 0313, WISE 1541, and WISE 2056 are shown in Figure 3.1.

3.2.6 Reduction Comparison with Skemer et al. 2016

The WISE 0855 data published in Skemer et al. (2016a) were re-reduced using the procedure described in this work. The results are compared in Figure 3.2. In Skemer et al. (2016a), the pixels affected by non-linearity 10% or less of the time in a mean spectral image were used in the extraction process. In this work, no non-linearity is accepted and this primarily affects the redder portion of the M-band spectrum where the

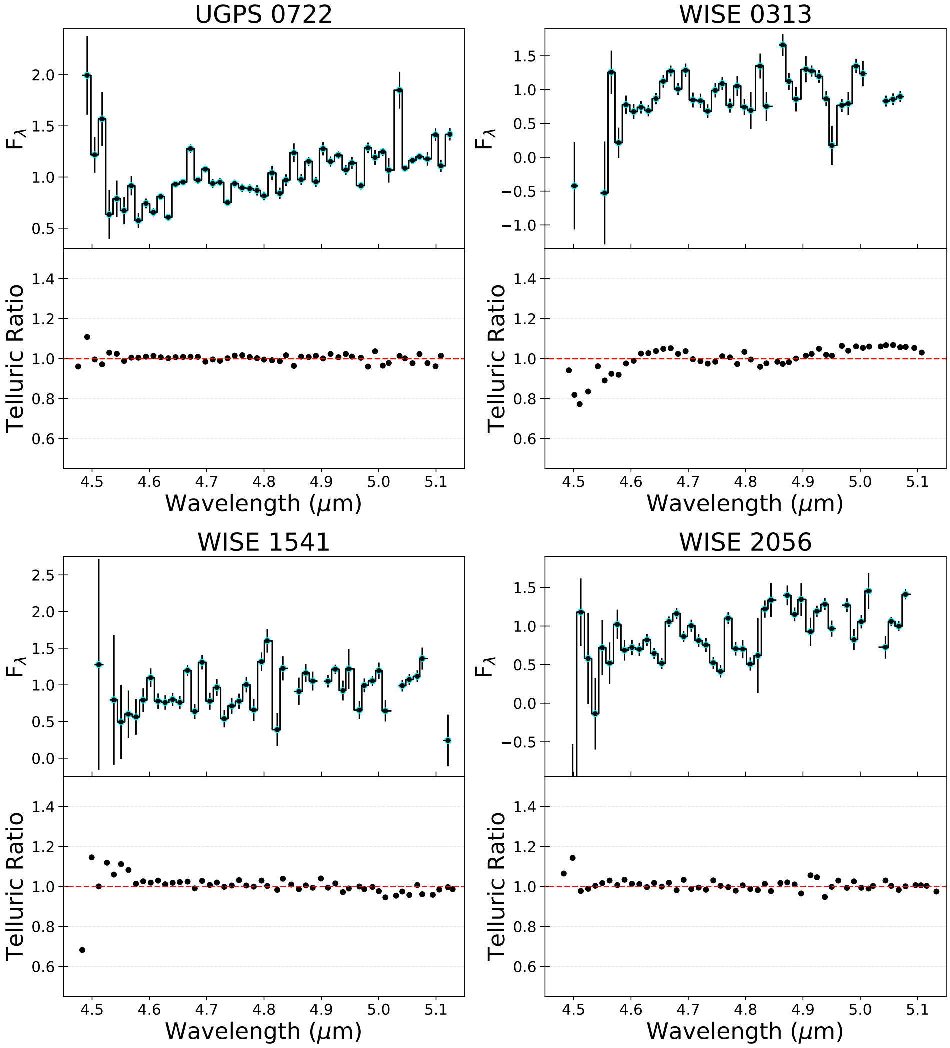

Figure 3.1: Each brown dwarf has a panel with a spectrum (*Top*) and the combined telluric ratio over the course of the program (*Bottom*). The telluric ratio is a metric for how consistent a calibrator spectrum is over a 2 hour period when the science data are taken. Percent deviations from unity are folded into the error bars of the final science spectrum of each object. The ratio between the before and after calibrators departs from unity significantly near areas of low atmospheric transmission. The median deviation for all brown dwarf telluric ratios is less than 2%, the largest deviations occur shortward of 4.55 μm where the deviations are as high as 14.5%

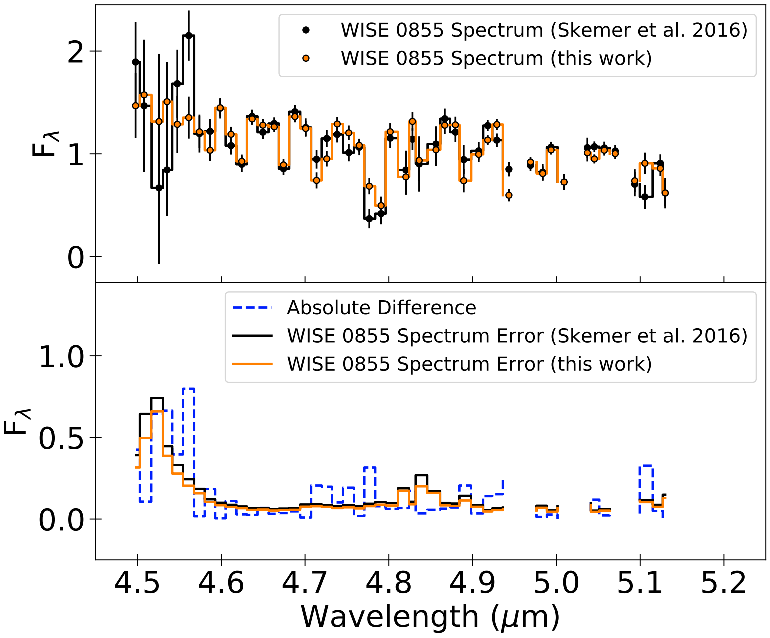

Figure 3.2: *Top Panel* - Black - The final WISE 0855 spectrum presented in Skemer et al. (2016a), Orange - The same data from Skemer et al. (2016a) re-reduced using the methods described in this paper and interpolated onto the same wavelength spacing as the Skemer et al. (2016a) spectrum. Error bars are plotted in black. *Bottom Panel* - Blue Dashed Line - The absolute difference between the previously published spectrum and the re-reduced spectrum. The solid orange and black lines are the errors of each spectrum. The spectral shapes are consistent, however there are discrepancies especially within regions of relatively low signal to noise.

sky is relatively brighter. On the blue side of the M-band spectrum there are fewer sky lines, leading to interpolation differences between this work and Skemer et al. (2016a). Qualitatively, the two reductions show very similar spectral shapes and absorption features across the M-band. The spectral points are on average within 1σ of each other, the largest differences are often in low signal-to-noise areas but the discrepancies are less than 3.5σ.

3.3 Sequence of Cool Objects

3.3.1 Object Temperatures

Brown dwarfs are often classified by their near-infrared spectral types rather than effective temperatures inferred from models, because the molecular features associated with certain spectral types can be proxies for effective temperature (Kirkpatrick, 2005). Near-infrared spectral indicators have been used to infer properties such as surface gravity, but these indicators are challenging to measure against the faint near-infrared emission of T and early Y dwarfs (Allers & Liu, 2013; Martin et al., 2017). Model-derived properties do have drawbacks, but they can be useful for predicting the gases or condensates that should be observable and constraining other atmospheric characteristics like vertical mixing, weather, and climate. Each object is classified by the effective temperature derived from estimated total fluxes and evolution models.

The adopted effective temperatures are derived from published near- and mid-IR photometry which captures 50 % to 84 % of the emitted flux from these brown dwarfs. Published near-infrared spectra could be used to constrain effective temperatures, but they do not cover the wavelength range where cooler brown dwarfs emit most of their luminosity and the spectra tend to dominate the fitting process. The Sonora Bobcat grid evolution models (Marley et al. in prep.) of solar metallicity, cloudless models are used to find a range of possible effective temperatures for each brown dwarf. The evolution model grid covers ages from 6000 years to 1 Gyr and masses of 0.5 to 102

---

[4] Sonora Bobcat grid models - https://zenodo.org/record/2628068#.Xb99ESV7lTI

Jupiter masses. We limit the mass range of the models to be between 1 Jupiter mass and 83 Jupiter masses. The 83 Jupiter mass upper limit is an estimate on the boundary between hydrogen-burning stars and brown dwarfs. Model ages are limited to cover from 1 Gyr to 10 Gyr; the only exception to this is UGPS 0722, whose inferred age range is 60 Myr and 1 Gyr (Leggett et al., 2012) based on kinematics. Gl 570D is assumed to be over 1 Gyr due the lack of activity from a stellar companion in the system (Burgasser et al., 2000). Gl 570 D and 2M0415 are assumed to have age upper limits of about 10 Gyr due their kinematics placing them in the Milky Way's galactic disk(Burgasser et al., 2000; Saumon et al., 2007). WISE 0313, WISE 2056, WISE 1541, and WISE 0855 do not have age constraints, but are assumed to have ages between 1 and 10 Gyr because they are all within 10 parsecs of the Sun like Gl570 D and 2M0415. The effective temperature range is determined by the evolution models that equal the estimated total flux derived from photometry. The adopted effective temperature is the Sonora grid atmospheric model with the effective temperature closest to the mean of the physical range. The Sonora Bobcat grid atmospheric model covers effective temperatures between 200 K - 2200 K with 25 K increments below 600 K, 50 K increments below 1000 K and 100 K increments below 2000 K. The surface gravities span log(g) = 3.2 to log(g) = 5.5 with increments of .25. Jupiter's effective temperature of 126 K is adopted from Li et al. (2012).

The list of substellar objects studied along with their published and adopted properties are shown in Table 3.2. The adopted effective temperature model spectra and synthetic photometry are compared against the published photometry in Figure 3.3. All of the estimated effective temperature ranges are consistent with previously published temperatures (Gl 570D Burgasser et al. 2000; Golimowski et al. 2004; Filippazzo et al. 2015, 2M0415 - Golimowski et al. 2004; Saumon et al. 2007; Filippazzo et al. 2015, WISE 0313 - Beichman et al. (2014), UGPS 0722 - Lucas et al. 2010; Leggett et al. 2012; Filippazzo et al. 2015, WISE 2056 - Beichman et al. 2014; Leggett et al. 2017; Zalesky et al. 2019, WISE 1541 - Beichman et al. 2014; Leggett et al. 2017; Zalesky et al. 2019,WISE 0855 - Luhman & Esplin 2016; Morley et al. 2018. The mean Sonora Bobcat evolution model-derived temperatures for WISE 2056 and WISE 1541 are each 90 K and 60 K warmer than published BT Settl model fits published in Beichman et al. (2014), but consistent with the Morley model derived temperatures in the same paper.

Object	Gl 570 D	2M 0415	UGPS 0722	WISE 0313	WISE 2056	WISE 1541	WISE 0855
Parallax	171.22 +/- 0.94 (1)	175.2 +/- 1.7 (1)	242.8 +/- 2.40 (2)	134.3 +/- 3.6 (3)	138.3 +/- 2.2 (3)	167.1 +/- 2.3 (3)	438.9 +/- 3.0 (3)
Filter				**Magnitudes**			
2MASS J	15.324 +/- 0.046 (4)	15.695 +/- 0.057 (4)	16.489 +/- 0.128 (4)	17.65 +/- 0.07 (5)	-	-	-
2MASS H	15.268 +/- 0.089 (4)	15.537 +/- 0.113 (4)	16.147 +/- 0.205 (4)	17.63 +/- 0.06 (5)	-	-	-
2MASS K_s	15.242 +/- 0.156 (4)	15.429 +/- 0.201 (4)	>14.823 (4)	-	-	-	-
Y MKO	-	-	17.37 +/- 0.02 (6)	18.27 +/- 0.05 (5)	19.94 +/- 0.05 (7)	21.63 +/- 0.13 (8)	-
J MKO	14.82 +/- 0.05 (9)	15.32 +/- 0.03 (10)	16.52 +/- 0.02 (6)	-	19.43 +/- 0.04 (7)	21.12 +/- 0.06 (7)	-
H MKO	15.28 +/- 0.05 (9)	15.70 +/- 0.03 (10)	16.90 +/- 0.02 (6)	-	19.96 +/- 0.04 (7)	21.07 +/- 0.07 (11)	-
K MKO	15.52 +/- 0.05 (9)	15.83 +/- 0.03 (10)	17.07 +/- 0.08 (6)	-	20.01 +/- 0.06 (7)	21.7 +/- 0.2 (11)	-
F105W	-	-	-	-	-	22.204 +/- 0.044 (8)	27.33 +/- .19 (17)
F110W	-	-	-	-	-	-	26.00 +/- .12 (17)
F125W	-	-	-	-	-	21.871 +/- 0.023 (8)	26.41 +/- .27 (18)
F127M	-	-	-	-	-	-	24.36 +/- .09 (17)
F140W	-	-	-	-	19.524 +/- 0.007 (8)	-	-
F160W	-	-	-	-	-	-	23.86 +/- 0.03 (18)
L′	12.98 +/- 0.05 (9)	13.28 +/- 0.05 (12)	13.4 +/- 0.3 (6)	-	-	-	-
M′	-	12.82 +/- 0.15 (12)	-	-	14.00 +/- 0.15 (13)	-	-
N	-	-	10.28 +/- 0.24 (6)	-	-	-	-
IRAC1	13.80 +/- 0.04 (14)	14.10 +/- 0.03 (14)	14.28 +/- 0.05 (6)	15.31 +/- 0.025 (15)	16.036 +/- 0.030 (5)	16.92 +/- 0.02 (7)	17.28 +/- .02 (20)
IRAC2	12.12 +/- 0.02 (14)	12.29 +/- 0.02 (14)	12.19 +/- 0.04 (6)	13.268 +/- 0.017 (15)	13.924 +/- 0.018 (5)	14.12 +/- 0.01 (7)	13.88 +/- 0.02
IRAC3	12.77 +/- 0.11 (14)	12.87 +/- 0.07 (14)	-	-	-	-	-
IRAC4	11.97 +/- 0.07 (14)	12.11 +/- 0.05 (14)	-	-	-	-	-
W1	14.824 +/- 0.034 (16)	15.108 +/- 0.041 (16)	15.250 +/- 0.045 (16)	15.953 +/- 0.045 (16)	16.48 +/- 0.075 (16)	16.736 +/- 0.165 (16)	17.819 +/- 0.327 (19)
W2	12.114 +/- 0.023 (16)	12.261 +/- 0.026 (16)	12.200 +/- 0.023 (16)	13.263 +/- 0.026 (16)	13.839 +/- 0.037 (16)	14.246 +/- 0.063 (16)	14.016 +/- 0.048 (19)
W3	10.863 +/- 0.082 (16)	11.132 +/- 0.113 (16)	10.206 +/- 0.069 (16)	12.045 +/- 0.264 (16)	11.731 +/- 0.249 (16)	>12.2 (16)	11.9 +/- 0.3 (13)
W4	>9.190 (16)	>8.638 (16)	>8.763 (16)	>8.668 (16)	>8.493 (16)	>8.892 (16)	-

Table 3.1: Published infrared photometry and parallaxes used to fit for effective temperatures of objects in our sample. The references for each measurement are indicated by a number enclosed in parenthesis following the error value. While UGPS 0722 and WISE 0313 are close in adopted temperature, WISE 0313 has less photometric data to constrain models. The references associated with each number are: 1 - Dupuy & Liu (2012), 2 - Kirkpatrick et al. (2012), 3 - Kirkpatrick et al. (2019), 4 - Skrutskie et al. (2006), 5 - Kirkpatrick et al. (2011), 6 - Lucas et al. (2010), 7 - Leggett et al. (2013), 8 - Schneider et al. (2015), 9 - Geballe et al. (2001), 10 - Knapp et al. (2004), 11 - Leggett et al. (2015), 12 - Golimowski et al. (2004), 13 - Leggett et al. (2017), 14 - Patten et al. (2006), 15 - Kirkpatrick et al. (2012), 16 - Cutri & et al. (2013)(AllWISE), 17 - Luhman & Esplin (2016), 18 - Schneider et al. (2016), 19 - Wright et al. (2014), 20 - Esplin et al. (2016).

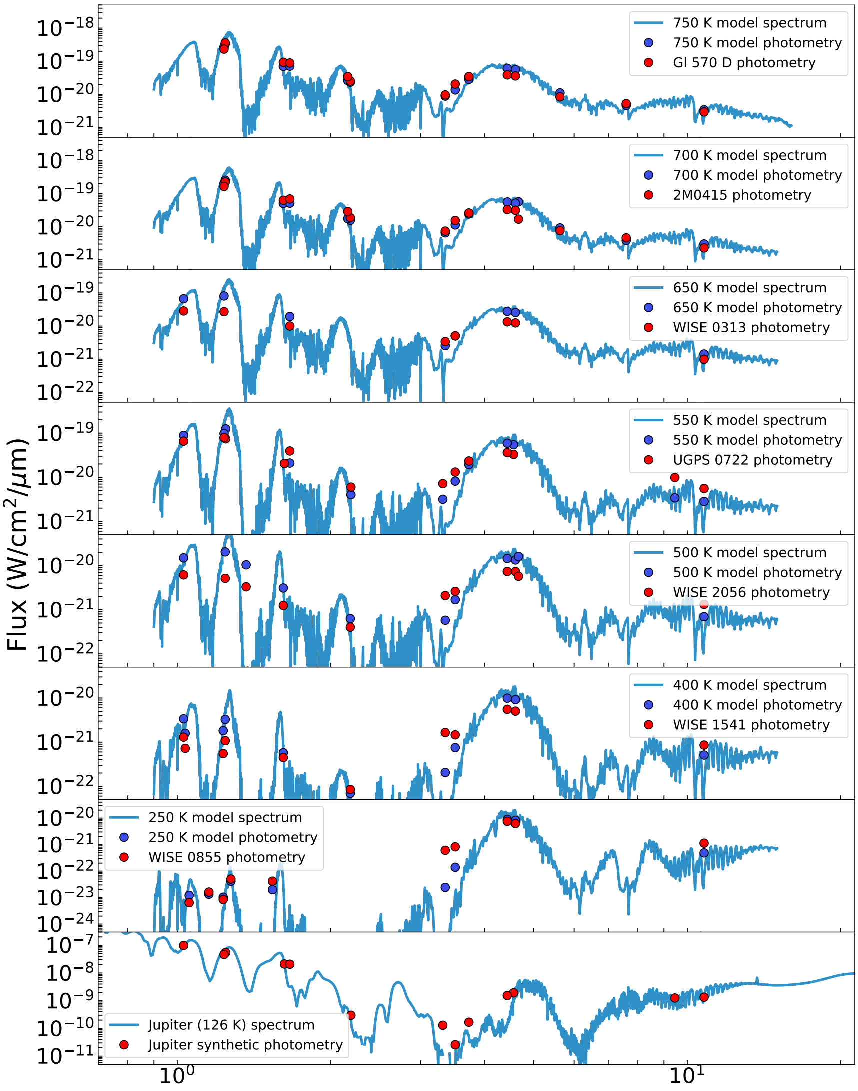

Figure 3.3: Model spectra (Blue lines) of the adopted temperatures scaled to the appropriate distance of the respective brown dwarf assuming thermochemical equilibrium, a size of 1 Jupiter radius, log(g) = 4.5, no clouds, and solar metallicity. The red points are the measured photometry of the brown dwarfs, blue points are the photometry derived from the model spectra. The error bars are about the size of the photometry points. There are major discrepancies across the near and mid-infrared, but the majority (50% - 89%) of the luminosity is captured with the available photometry. Jupiter's spectrum is real data was compiled by Mike Cushing (private communication) and originally taken with the Cassini Composite Infrared Spectrometer (CIRS), Infrared Space Observatory (ISO) Short Wavelength Spectrometer (SWS), and the Galileo Near-Infrared Mapping Spectrometer (NIMS). Shortward of 4 microns, Jupiter's spectrum is entirely reflected sunlight and without the Sun, the CH_4, C_2H_6, and C_2H_2 emission lines would not be present. The synthetic photometry of Jupiter is calcuated using the same bandpasses as the UGPS 0722 data.

Object	**Adopted Temperature (K)**	**Effective Temperature Range (K)**	**Temperature Reference**	**Spectral Type**	**Spectral Type Reference**	**Surface Gravity Range log(cm s^{-2})**
Gl 570 D	750 K	716 - 812	re-fit in this work	T7.5	Burgasser et al. (2006)	4.7 - 5.4
2MASS J0415-0935	700 K	649 - 734	re-fit in this work	T8	Burgasser et al. (2006)	4.6 - 5.3
WISE 0313	650 K	606 - 685	re-fit in this work	T8.5	Kirkpatrick et al. (2011)	4.6 - 5.3
UGPS 0722	550 K	522 - 558	re-fit in this work	T9	Cushing et al. (2011)	3.7 - 4.4
WISE 2056	500 K	471 - 522	re-fit in this work	Y0	Schneider et al. (2015)	4.4 - 5.0
WISE 1541	400 K	396 - 434	re-fit in this work	Y1	Schneider et al. (2015)	4.3 - 4.9
WISE 0855	250 K	249 - 260	re-fit in this work	>Y4	Kirkpatrick et al. (2019)	3.5 - 4.5
Jupiter	126 K	-	Li et al. (2012)	-	-	3.4

Table 3.2: Objects in our analysis which have temperatures from 75 K to 125 K and M-band spectral observations. WISE 0855's spectral type was inferred with photometry in Schneider et al. (2016), no near infrared spectral observations have been taken. The range of possible surface gravities for brown dwarfs in the last column are from the cloudless Sonora Bobcat evolution models and assume ages between 1 Gyr and 10 Gyr.

3.3.2 M-Band Spectral Sequence

Figure 3.4 shows the M-band spectra of brown dwarfs with effective temperatures from 750 K to 250 K and Jupiter. The M-band spectrum of 2M0415 was taken with the AKARI spacecraft and published in Sorahana & Yamamura (2012). The adopted M-band spectrum for Gl570D was taken using Gemini/NIRI and published in Geballe et al. (2009). The AKARI spectrum of Gl570D from Sorahana & Yamamura (2012) was not used because it has lower signal-to-noise than the Gemin/NIRI spectrum. The spectrum of WISE 0855 is the re-reduced version from this work. Jupiter's spectrum taken with the Short-Wavelength Spectrometer (SWS) on ISO (Encrenaz et al., 1996) was binned down from a resolution of 31,000 to 370. WISE 0855 has a distinct spectral slope compared to the rest of the sample that closely resembles an equilibrium atmosphere dominated by water across the M-band as shown in Figure 3.5. UGPS 0722 is the object with the highest signal-to-noise in our program and shows an absorption feature across 4.5 μm to 4.8 μm, peaking at $\sim$4.7 μm that looks similar to carbon monoxide which has been seen in T-dwarfs like Gl229B (Noll et al. (1997), Figure 3.6).

Science Target	Date YYYYMMDD	Total Integration Time (minutes)	Science Airmass	Science IQ	Science WVC	Telluric Calibrator	Telluric Airmass	Telluric IQ	Telluric WVC	Data Comments
WISE 0313	20161014	36.0	1.899	70%	20%	HIP 10054	2.090	70%	20%	
WISE 0313	20161014	36.0	1.934	70%	20%	HIP 16725	1.746	70%	20%	The single science frame with detector noise not included.
WISE 0313	20161015	36.0	1.909	70%	50%	HIP 10054	2.088	70%	50%	
WISE 0313	20161015	36.0	1.901	70%	50%	HIP 16725	1.691	70%	50%	
WISE 0313	20161104	36.0	1.973	70%	50/80%	HIP 10054	2.109	70%	50%	
WISE 0313	20161104	24.0	2.028	70%	50%	HIP 16725	1.827	20%	50%	
WISE 0313	20170103	12.0	1.915	70%	50%	HIP 10054	2.093	70%	50%	
WISE 0313	20170103	12.0	1.899	20%	50%	HIP 16725	1.687	20%	50%	

Table 3.3: The reported air masses of the science target and calibrator observations are median values over the course of the sequence. Image Quality (IQ) and Water Vapor Content (WVC) describe constraints on the point spread function width and the water content of the observations. See http://www.gemini.edu/sciops/telescopes-and-sites/observing-condition-constraints for more details

Science Target	**Date YYYYMMDD**	**Total Integration Time (minutes)**	**Science Airmass**	**Science IQ**	**Science WVC**	**Telluric Calibrator**	**Telluric Airmass**	**Telluric IQ**	**Telluric WVC**	**Data Comments**
UGPS 0722	20161115	36.0	1.110	70%	20%	HIP 30387	1.104	70%	20%	
UGPS 0722	20161115	36.0	1.164	70%	20%	HIP 42028	1.093	70%	20%	
UGPS 0722	20170104	36.0	1.186	70%	50%	HIP 30387	1.152	20%	50%	
UGPS 0722	20170104	36.0	1.110	20%	50%	HIP 42028	1.101	70%	50%	

Table 3.4: The reported air masses of the science target and calibrator observations are median values over the course of the sequence. Image Quality (IQ) and Water Vapor Content (WVC) describe constraints on the point spread function width and the water content of the observations. See http://www.gemini.edu/sciops/telescopes-and-sites/observing-condition-constraints for more details

Science Target	Date YYYYMMDD	Total Integration Time (minutes)	Science Airmass	Science IQ	Science WVC	Telluric Calibrator	Telluric Airmass	Telluric IQ	Telluric WVC	Data Comments
WISE 2056	20161009	36.0	1.057	20%	80%	HIP 95002	1.173	20%	80%	
WISE 2056	20161009	36.0	1.207	20%	80%	HIP 108060	1.135	20%	80%	
WISE 2056	20161010	36.0	1.014	20%	80%	HIP 95002	1.013	20%	80%	2056 traces not visible. Brown dwarf data not included
WISE 2056	20161010	36.0	1.011	20%	80%	HIP 108060	1.002	20%	80%	Detector noise. Brown dwarf data not included
WISE 2056	20161011	36.0	1.034	70%	50%	HIP 95002	1.113	70%	50%	
WISE 2056	20161011	36.0	1.231	70%	50%	HIP 108060	1.156	70%	50%	2056 traces not visible, Detector noise. Brown dwarf data not included.
WISE 2056	20161014	36.0	1.006	70%	50%	HIP 95002	1.023	70%	50%	2056 traces not visible, Brown dwarf data not included.
WISE 2056	20161014	36.0	1.026	70%	50%	HIP 108060	1.008	70%	50%	
WISE 2056	20161015	36.0	1.006	70%	50%	HIP 95002	1.026	70%	50%	
WISE 2056	20161015	36.0	1.021	70%	50%	HIP 108060	1.006	70%	50%	
WISE 2056	20161018	36.0	1.005	70%	20%	HIP 95002	1.026	70%	20%/50%	Fog, detector noise. Brown dwarf data not included
WISE 2056	20161018	22.0	1.015	70%	20%	HIP 95002	1.026	70%	20%/50%	Fog, detector noise. Brown dwarf data not included
WISE 2056	20161022	36.0	1.005	20%	80%	HIP 95002	1.045	20%	80%	
WISE 2056	20161022	36.0	1.042	70%	80%	HIP 108060	1.020	70%	80%	
WISE 2056	20161113	36.0	1.064	70%	50%	HIP 95002	1.206	70%	50%	Calibrations taken in K-band. Brown dwarf data not included
WISE 2056	20161113	36.0	1.215	70%	50%	HIP 108060	1.162	70%	50%	Detector noise. Brown dwarf data not included
WISE 2056	20161114	36.0	1.058	70%	50%	HIP 95002	1.1985	70%	50%	
WISE 2056	20161114	36.0	1.193	70%	50%	HIP 108060	1.127	70%	50%	
WISE 2056	20161115	36.0	1.070	70%	50%	HIP 95002	1.222	70%	80%	
WISE 2056	20161115	36.0	1.224	70%	50%	HIP 108060	1.158	70%	20%	
WISE 2056	20170611	36.0	1.099	20%	80%	HIP 95002	1.030	70%	80%	
WISE 2056	20170611	36.0	1.018	20%	80%	HIP 108060	1.024	70%	80%	
WISE 2056	20170612	36.0	1.267	20%	80%	HIP 95002	1.112	20%	80%	
WISE 2056	20170612	36.0	1.087	20%	80%	HIP 108060	1.113	70%	80%	
WISE 2056	20170616	36.0	1.221	70%	80%	HIP 95002	1.087	70%	80%	
WISE 2056	20170616	36.0	1.067	70%	80%	HIP 108060	1.086	70%	80%	

Table 3.5: The reported air masses of the science target and calibrator observations are median values over the course of the sequence. Image Quality (IQ) and Water Vapor Content (WVC) describe constraints on the point spread function width and the water content of the observations. See http://www.gemini.edu/sciops/telescopes-and-sites/observing-condition-constraints for more details

Science Target	Date YYYYMMDD	Total Integration Time (minutes)	Science Airmass	Science IQ	Science WVC	Telluric Calibrator	Telluric Airmass	Telluric IQ	Telluric WVC	Data Comments
WISE 1541	20170517	36.0	1.363	70%	20%	HIP 70765	1.335	70%	20%	
WISE 1541	20170517	36.0	1.422	70%	20%	HIP 81457	1.437	70%	20%	Severe detector noise. Brown dwarf data not included
WISE 1541	20170518	36.0	1.363	70%	20%	HIP 70765	1.324	70%	20%	
WISE 1541	20170518	36.0	1.436	70%	20%	HIP 81457	1.455	70%	20%	
WISE 1541	20170605	36.0	1.394	70%	80%	HIP 70765	1.316	70%	80%	
WISE 1541	20170605	36.0	1.363	70%	80%	HIP 81457	1.406	70%	80%	
WISE 1541	20170606	36.0	1.368	70%	50%	HIP 70765	1.315	70%	50%	
WISE 1541	20170606	36.0	1.378	70%	50%	HIP 81457	1.414	70%	50%	
WISE 1541	20170610	36.0	1.388	70%	>80%	HIP 70765	1.316	70%	80%	
WISE 1541	20170610	36.0	1.365	20%	>80%	HIP 81457	1.407	20%	80%	
WISE 1541	20170611	36.0	1.428	70%	50% / 80%	HIP 70765	1.327	70%	80%	
WISE 1541	20170611	36.0	1.362	70%	80%	HIP 81457	1.408	70%	80%	
WISE 1541	20170612	36.0	1.414	20%	80%	HIP 70765	1.328	20%	80%	WISE 1541 traces not visible. Brown dwarf data not included
WISE 1541	20170612	36.0	1.362	20%	80%	HIP 81457	1.410	20%	80%	
WISE 1541	20170623	36.0	1.451	20%	80%	HIP 70765	1.336	20%	80%	
WISE 1541	20170623	36.0	1.363	20%	80%	HIP 81457	1.426	20%	80%	
WISE 1541	20170708	36.0	1.362	20%	20%	HIP 70765	1.329	20%	20%	
WISE 1541	20170708	36.0	1.416	20%	20%	HIP 81457	1.432	70%	20%	

Table 3.6: The reported air masses of the science target and calibrator observations are median values over the course of the sequence. Image Quality (IQ) and Water Vapor Content (WVC) describe constraints on the point spread function width and the water content of the observations. See http://www.gemini.edu/sciops/telescopes-and-sites/observing-condition-constraints for more details

Gl 570D, 2M0415, and WISE 0313 show a similar absorption feature as UGPS 0722, but with less data quality for WISE 0313 and a flatter spectral slope for 2M0415. Gl 570D's absorption feature and spectral slope closely resemble UGPS 0722's spectrum[5]. WISE 2056 and WISE 1541 look relatively flat, but appear to have increasing flux at redder wavelengths. Carbon monoxide and the shape of its M-band feature are discussed in more detail in Section 3.4.2. WISE 1541 (400 K), WISE 0855 (250 K), and Jupiter (126 K) cover a temperature range of less than 300 K, yet they express different spectral shapes and molecular absorption features. Jupiter's phosphine (PH_3) feature that stretches from 4.5 μm to 4.7 μm is a tracer of atmospheric quenching, but PH_3 is not obvious for any of the brown dwarfs. However, Jupiter's metallicity abundance is 3 times the solar value and that is important when placing it in context to brown dwarfs which are being modeled and discussed in this paper.

3.4 Model Comparisons

3.4.1 Equilibrium Models

In equilibrium, the dominant absorber across the M-band is water for brown dwarfs below effective temperatures of 800 K and the spectral slope is most sensitive to cloudiness and temperature (Morley et al. (2014, 2018), see Figure 3.5). A model comparison of the cloudless, equilibrium case for each brown dwarf is done using the adopted temperatures found in Section 3.3 (Figure 3.8), assuming surface gravity of

---

[5] We adopt the Gemini spectrum because it has higher signal-to-noise than the AKARI data. The AKARI spectrum does not have an obvious CO feature, but it is consistent within error to the Gemini/NIRI spectrum.

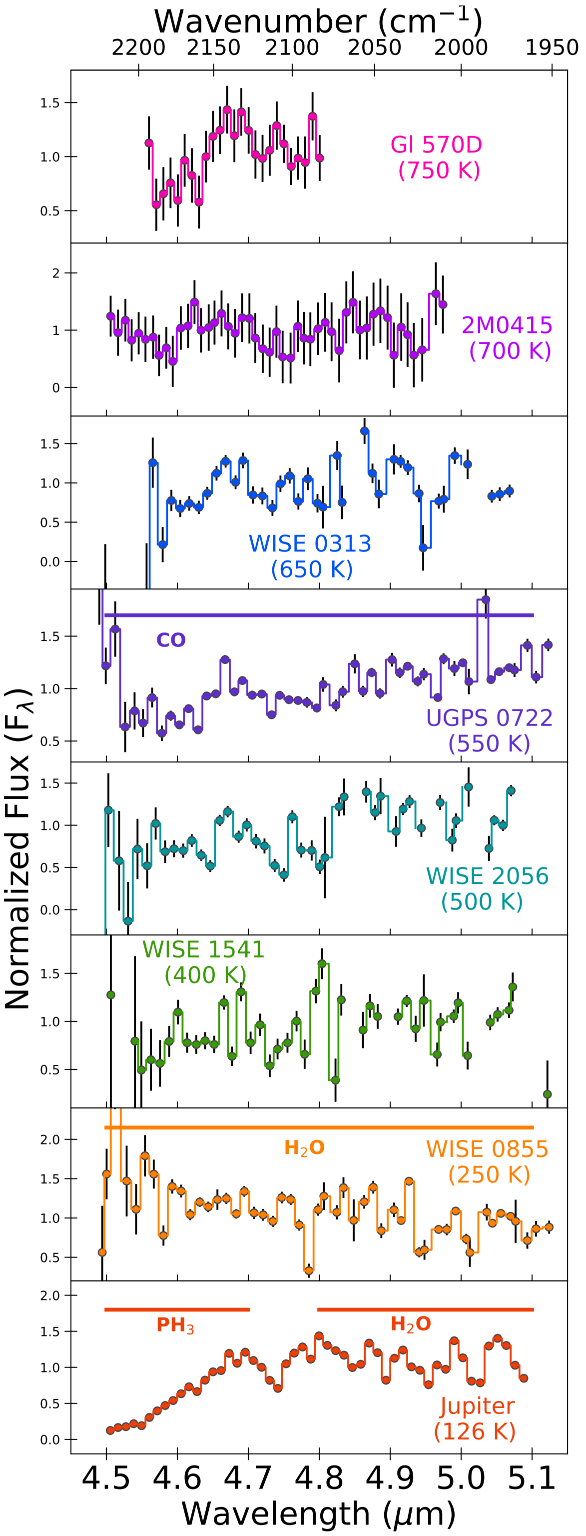

Figure 3.4: Normalized M-band spectra of cool substellar objects. The y-axis of each plot are set differently to emphasize carbon monoxide absorption across the spectra. All of the brown dwarfs show evidence of carbon monoxide absorption indicating that their atmospheres are out of chemical equilibrium. Carbon monoxide has been detected in Jupiter at very high spectral resolution. (Bézard et al., 2002).

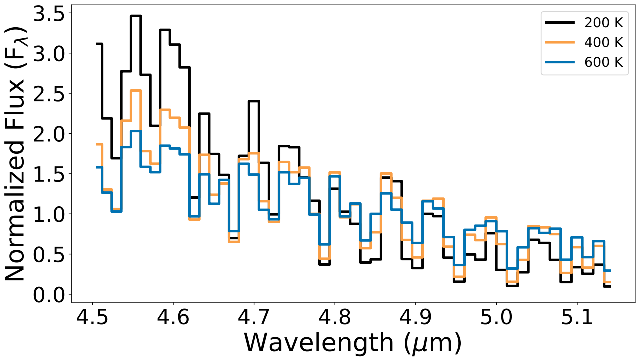

Figure 3.5: Normalized M band spectra of cloudless, solar metallicitiy brown dwarfs of varying temperatures. In normalized space, most of the temperature change can be seen shortward of 4.75 μm and at lower temperatures the spectral slope becomes steeper across the M-band.

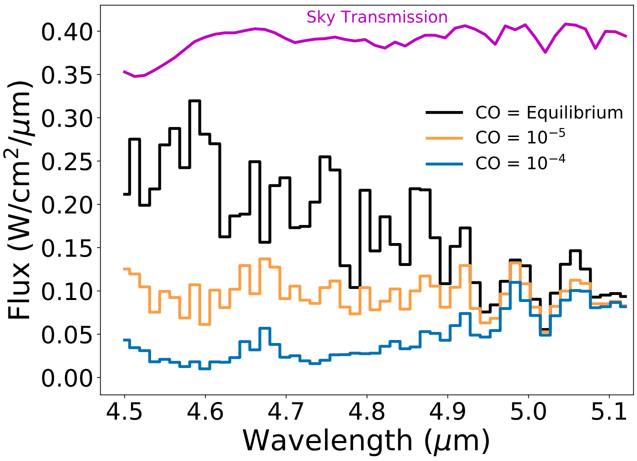

Figure 3.6: M-band spectra of a 550 K cloudless, solar metallicity brown dwarf with varying mole fractions of carbon monoxide. The carbon monoxide abundance influences the entire M-band spectral region. The sky transmission is plotted in magenta at the top of the figure and lower transmission areas typically correspond to higher telluric errors.

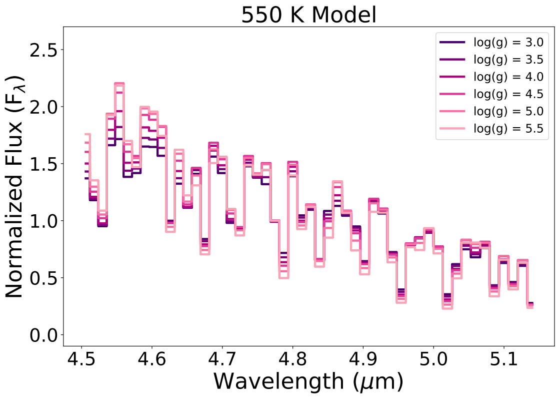

Figure 3.7: A 550 K, cloudless, solar metallicity model with a range of surface gravities plotted. Where surface gravity influences the spectrum the most, the data quality is typically poor(see Figure 3.6).

log(g) = 4.5. The surface gravities are not known, but have very little effect on the shape of the normalized M-band spectra (Figure 3.7). The cloudless equilibrium models do not adequately fit the spectra of the brown dwarfs, because of increased flux on the blue side of the models relative to the data. However, water vapor absorption beyond ~4.85 μm in the equilibrium models do line up with a few dips in the data for some brown dwarfs.

3.4.2 Disequilibrium, Carbon Monoxide Enhanced Models

Vertical atmospheric mixing can bring up carbon monoxide-rich gas from higher temperature regions into pressure levels probed by the observations. CO is usually observed in the K-band spectra of L and early T dwarfs, but the much stronger transitions of the fundamental band, centered near 4.7 μm, can be observed in the M band in late T dwarfs, when the K-band CO features are obscured by CH_4 absorption.

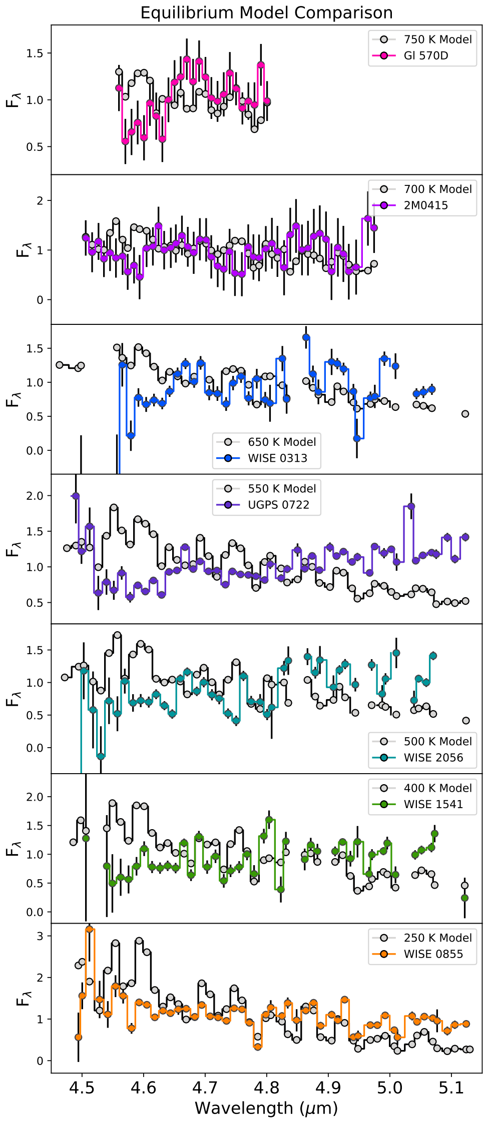

Figure 3.8: The M-band spectra of each brown dwarf (Color) plotted against the same temperature cloudless, solar metallicity, chemical equilibrium model (Light Grey). The models are binned down to the number of elements in the data and then interpolated onto the data's spectral grid. In all cases the models have steeper spectral slopes, which cannot be explained by temperature alone. The y-axis does not show the full range of spectral data to emphasize absorption features.

As mentioned earlier, the brown dwarf Gl229B (900 K) showed absorption across the M-band (Figure 1 and 2 in Noll et al. (1997)) that is best-fit using atmospheric models with enhanced abundances of carbon monoxide. CO has also been previously detected in the atmosphere of Jupiter (Bézard et al., 2002). UGPS 0722 and other brown dwarfs in our sample share similar characteristics with the Gl229B spectrum, therefore we try to understand how much carbon monoxide can explain the variations between the spectra in our sample.

The carbon monoxide enhanced models for the normalized M-band spectra fitting use pressure-temperature profiles from the Sonora Bobcat models. The carbon monoxide abundance profile is changed for different quench abundances of carbon monoxide. Moderate resolution spectra are generated as described in the Appendix of Morley et al. (2015). For each adopted effective temperature and surface gravity of $\log(g) = 4.5$, a model grid with CO mole fractions between 10^{-7} and 10^{-4} (spaced by a factor of 3) are fit against the M-band spectra. Adding carbon monoxide alters the M-band from 4.5 μm to 4.95 μm by flattening out regions of the spectrum and leaving a peak at 4.7 μm (Figure 3.6). Figure 3.9 shows the best fit carbon monoxide enhanced models for each brown dwarf. All of the brown dwarfs needed disequilibrium carbon monoxide abundances to achieve a better spectral fit. These best-fit mole fraction values of carbon monoxide range from values of 10^{-4} to 10^{-7}, with lower abundances at lower effective temperature. WISE 1541 still has some discrepancy on the blue portion of the spectrum, where the disequilibrium model has a slightly steeper slope than the data.

The expected equilibrium mole fraction of carbon monoxide falls rapidly from

$\sim 10^{-7}$ to $\sim 10^{-18}$ (Lodders & Fegley, 2002) within the M-band photopshere for effective temperatures between 750 K and 500 K, which points to atmospheric quenching driving the CO abundances of our objects to disequilibrium. All of the objects in our sample have disequilibrium CO abundances, therefore, atmospheric quenching may be ubiquitous among cool brown dwarfs and gas giant exoplanets. Directly imaged, gas giant exoplanets found around younger stars tend to have lower surface gravities relative to field brown dwarfs, making them prone to stronger atmospheric mixing and expressing disequilibrium abundances of molecules (Zahnle & Marley, 2014). If future directly imaged gas giants frequently fall somewhere within the effective temperature range of the objects in Table 3.2, M-band spectroscopy will be vital for their characterization. The binned spectra presented in this work are fairly low resolution (R $\sim$ 370), but Jupiter's CO abundance is only detectable with high resolution (ex. R $\sim$ 42,680 Bézard et al. 2002)) spectroscopy. As we image colder and older gas giants, higher resolution modes will be essential for exoplanet-focused instruments.

3.4.3 Modeling Clouds and CO in WISE 0855

Carbon monoxide and clouds both have the potential to significantly alter the spectral shape across the M-band (Morley et al., 2014) and we briefly explore their combined effect in this Section. The models described in Section 2.3 of Morley et al. (2018) that have homogeneous clouds and varying amounts of carbon monoxide are used to fit WISE 0855's spectrum. The effective temperature is fixed at 250 K and the surface gravity is fixed at log(g) equal to 4. The lower surface gravity used for WISE 0855 is

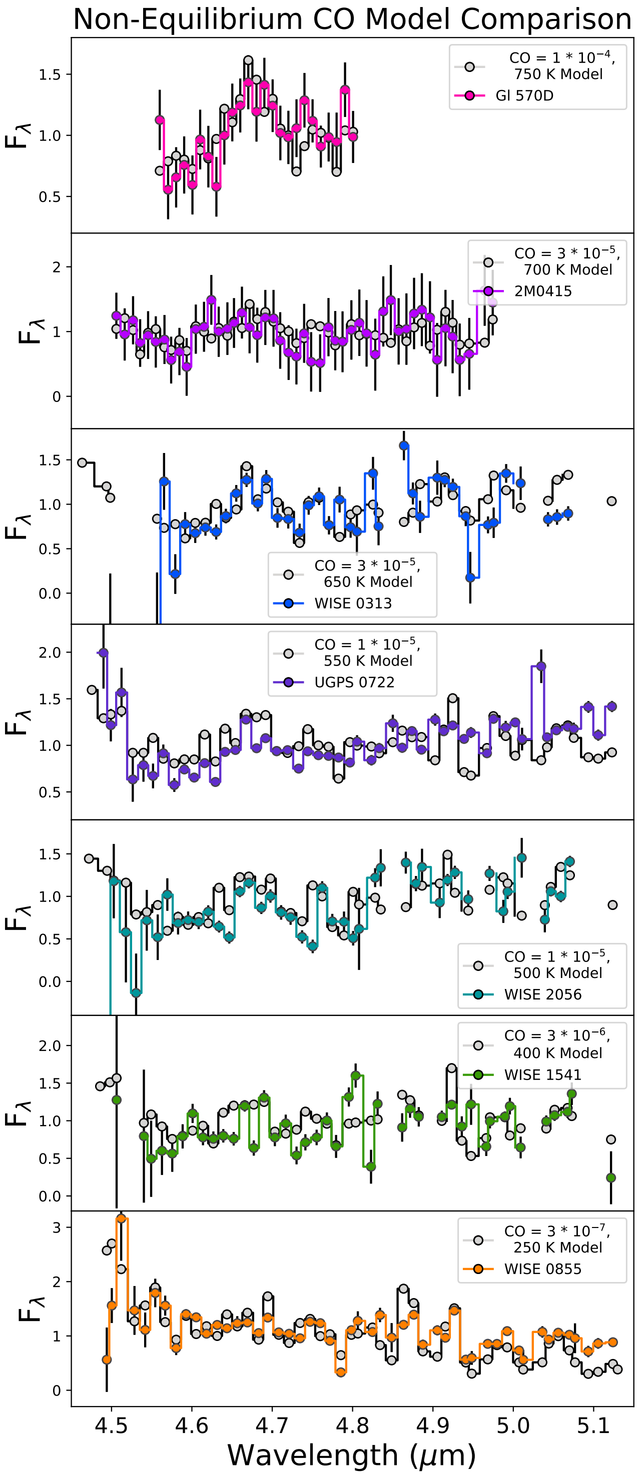

Figure 3.9: The M-band spectra of each brown dwarf (Color) plotted with a cloudless, solar metallicity model with the best fit adjusted carbon monoxide mole fraction (Light Grey). All brown dwarfs need enhanced abundances of CO for a better fit. Warmer objects typically have more carbon monoxide. The y-axis does not show the full range of spectral data to emphasize absorption features

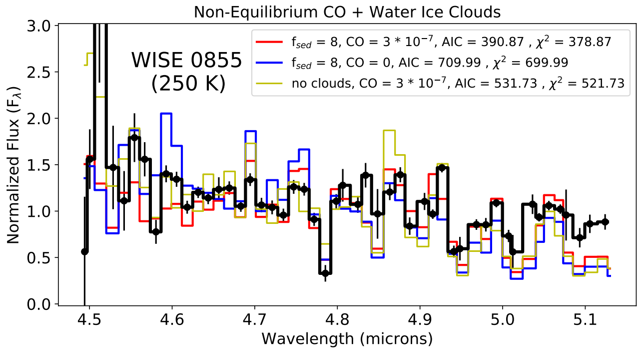

Figure 3.10: Comparisons of models with clouds, CO, and clouds with CO. Both WISE 0855 and WISE 1541 are better fit with CO and clouds, WISE 1541 shows significant deviations from the models at shorter wavelengths within the M-band.

from Morley et al. (2018), though it has a minor effect on the spectrum. Our cloudy model grid covers CO mole fractions between 10^{-5} and $10^{-7.5}$, including a model with no CO. The clouds are parameterized by the sedimentation efficiency (f_{sed}) defined in Ackerman & Marley (2001), where lower values of f_{sed} produce extended lower density clouds and higher values produce thinner, dense clouds. Cloudy models have f_{sed} values of 2 - 10, spaced by increments of 2. Each model is binned to the resolution of the data then interpolated onto the wavelength spacing of the data for fitting.

The best fit model for WISE 0855 has an f_{sed} value of 8 and CO mole fraction of $10^{-6.5}$ (Figure 3.10). According the Akaike information Criterion (AIC), adding clouds to the model is justified because the metric penalizes the addition of extra parameters while assessing relatively model quality. The AIC is chosen over the Bayesian information criterion (BIC) because the true model is not known (see Figure 3.3) and we are looking for a relative comparison of goodness of fit. The AIC of the best-fit cloud and CO model is 390.87, while the AIC values of the cloud-only and CO-only models are 709.99 and 531.73 respectively. Clouds improve the spectral fits compared to equilibrium in all cases, but clouds typically make very broad wavelength changes along a spectrum and should be constrained with a full spectrum or spectral energy distribution of photometry in future work. Our analysis supports the prediction from Morley et al. (2014), that water clouds are a significant opacity source in brown dwarfs under 400 K, and the clouds become optically thick at temperatures between 375 K - 350 K.

The presence of water clouds in WISE 0855's atmosphere has been debated in the literature, but future space-based facilities like JWST may be able place better constraints on water clouds or other condensates. The first evidence for water clouds on WISE 0855 came from the work of Faherty et al. (2014), which used J_{MKO} - W2 colors to rule out atmospheric models that contained no clouds and models with only sulfide clouds. The first spectrum of WISE 0855 published in Skemer et al. (2016a) showed that a grey opacity source, representing water clouds, produces a better spectral fit to the M-band data than an atmospheric model with no clouds. The same spectrum of WISE 0855 was later modeled with water ice clouds (Morley et al., 2018) showing the same results as Skemer et al. (2016a), providing stronger evidence in favor of water clouds. The photometric monitoring done with *Spitzer* presented in Esplin et al. (2016) showed that WISE 0855's variability was irregular and did not have the same pattern between simultaneous *Spitzer* [3.6] and *Spitzer* [4.5] observations. The authors claimed that the irregular photometric series was similar to other T-dwarfs, therefore the source of the variability must arise from opacity sources common to both Y and

T-dwarfs, which could not be water clouds. At the moment, it is likely not feasible to attempt low-resolution spectroscopic monitoring of WISE 0855 from the ground and near-infrared spectroscopic data have not been taken with the Hubble Space Telescope. Photometric measurements may not be able to distinguish cloud variability from heterogenous disequilibrium chemistry or hot spots, therefore spectrographs like NIRSpec on JWST will be needed for space-based, time series, observations to characterize WISE 0855 atmosphere.

3.5 Atmospheric Quenching and Other Disequilibrium Molecules

3.5.1 Inferred Atmospheric Mixing from CO

The chemistry of cool substellar atmospheres is complex and relies on many poorly constrained values such as metallicity, gravity, abundances of trace gases, and vertical mixing rates in the atmosphere. In this section we are not attempting to provide exact calculations to explain the disequilibrium abundances of carbon monoxide in our spectra, but understand what assumptions can reasonably explain the spectral features within our sample and if fundamental assumptions need to be changed in future work.

The strength of large scale vertical mixing is often parameterized by the eddy diffusion coefficient (K_{zz}) which is defined by the equation

$$K_{zz} = \frac{L^2}{\tau_{\rm mix}} \tag{3.1}$$

where L is a length scale of mixing and τ_{mix} is the timescale of mixing. Higher values of K_{zz} correspond to shorter mixing timescales (τ_{mix}) within an atmosphere. Molecules have a chemical timescale (τ_{chem}) at which they are either created and/or turned into new products and these processes are often strongly dependent on temperature and pressure. If at a given pressure and temperature, the mixing timescale of an atmosphere is greater than the chemical timescale of a net reaction, that gas has sufficient time to reach **chemical equilibrium**. If the chemical timescale of a net reaction is greater than the rate of mixing at specific pressure and temperature, the molecule will **not be in chemical equilibrium**. In the disequilibrium case, it is often assumed that the detected abundance of a molecular species in the upper atmosphere is set by the **quench point**, where the chemical timescale is equal to the mixing timescale.

Following the prescription of Zahnle & Marley (2014), the length scale is assumed to be equal to the pressure scale height (H), which is calculated by

$$H = L = \frac{k_b T}{\mu m_h g} \tag{3.2}$$

Assuming a log(g) equal to 4.5, the median scale height for the 250 K - 750 K effective temperature range calculated between pressures of 10^{-4} to 10^{5} bars spans from 32 km to 61 km. The corresponding mixing timescale along the pressure-temperature profile is

$$\tau_{\text{mix}} = \frac{H^2}{K_{zz}} \tag{3.3}$$

The eddy diffusion coefficient value of an object is estimated by finding the point along the pressure-temperature profile where the best-fit molecular abundance is found in chemical equilibrium at solar metallicity, then finding the K_{zz} value required to match the mixing timescale to the chemical timescale at that point. We explore the disequilibrium chemistry of three molecules: carbon monoxide (CO), phosphine (PH_3), and ammonia (NH_3). The equilibrium abundance information as a function of pressure and temperature for CO and NH_3 is taken from the Sonora Bobcat structure models. The abundance of PH_3 along a pressure-temperature profile is calculated by doing 2-D linear interpolation[6] over the mole fraction contour lines versus temperature and pressure in Visscher et al. (2006). The chemical timescale equations for CO and NH_3 are from Equations 12, 13, 14, and 32 of Zahnle & Marley (2014), which are derived from empirical exponential fits to one dimensional models that treat vertical mixing like diffusion. The chemical timescales for PH_3 are derived for each pressure-temperature profile using techniques in Visscher et al. (2006). A constant entropy adiabat in the deep atmosphere is assumed to extend the pressure range of the Sonora grid from a log(P(bars)) of 2.2 out to a depth of log(P (bars)) of 6. The value of μ along the extended pressure-temperature profile is taken as the last value at the high pressure end of the original profile. The mean molecular weight only changes by .007% over the entire profile before extension. With the extended pressure-temperature profiles and the appropriate timescale information we can estimate the K_{zz} values and quench points of CO, PH_3, and NH_3 for each brown dwarf in our sample and Jupiter.

The atmospheric quench points are calculated for each brown dwarf and Jupiter using the best fit CO values. Initially, we assume a log(g) = 4.5 for all brown dwarfs

---

[6] scipy.interpolate.griddata

and Jupiter has a log(g) of 3.4. Jupiter's CO abundance profile is influenced by external factors, but the pressures probed by the M-band extend to the depth where CO is quenched (Bézard et al., 2002; Visscher et al., 2010; Visscher & Moses, 2011). In Figure 3.11 the CO inferred quench points are plotted along pressure-temperature profiles representative of our gas giant sample. The quench points for fixed values of K_{zz} are also plotted. Cooler objects have less CO, but require larger eddy diffusion coefficients to maintain those values. For fixed surface gravity and K_{zz} values, warmer brown dwarfs will have more CO gas detected in the atmosphere. Lower gravity objects will have higher abundances of CO for the same K_{zz} value at fixed effective temperature. Lower gravity caused by youth is one of the reasons why directly imaged exoplanets near the L to T transition can display enhanced CO relative to methane dominated T-dwarfs of similar effective temperature (Barman et al., 2011b; Miles et al., 2018).

CO is a promising tracer for atmospheric quenching in gas giants, but different spectral resolutions will be required to capture the full range of quench levels possible. Between K_{zz} values of 10^2 cm^2 s^{-1} and 10^8 cm^2 s^{-1} the CO mole fraction changes by a factor of 1000 at fixed effective temperature. From 700 K to Jupiter (126 K) the range of CO abundances spans mole fractions of 10^{-13} to 10^{-4}. Jupiter's relatively low CO abundance has only been detected through high resolution spectroscopy, therefore brown dwarfs with smaller K_{zz} values will also need more resolution at sufficiently high signal-to-noise for CO detections. The best fit CO abundances, inferred K_{zz} values, PH_3 abundances, and NH_3 abundances are listed in Table 3.15. The abundances of PH_3 and NH_3 based on CO will be discussed in Sections 3.5.3 and 3.5.4.

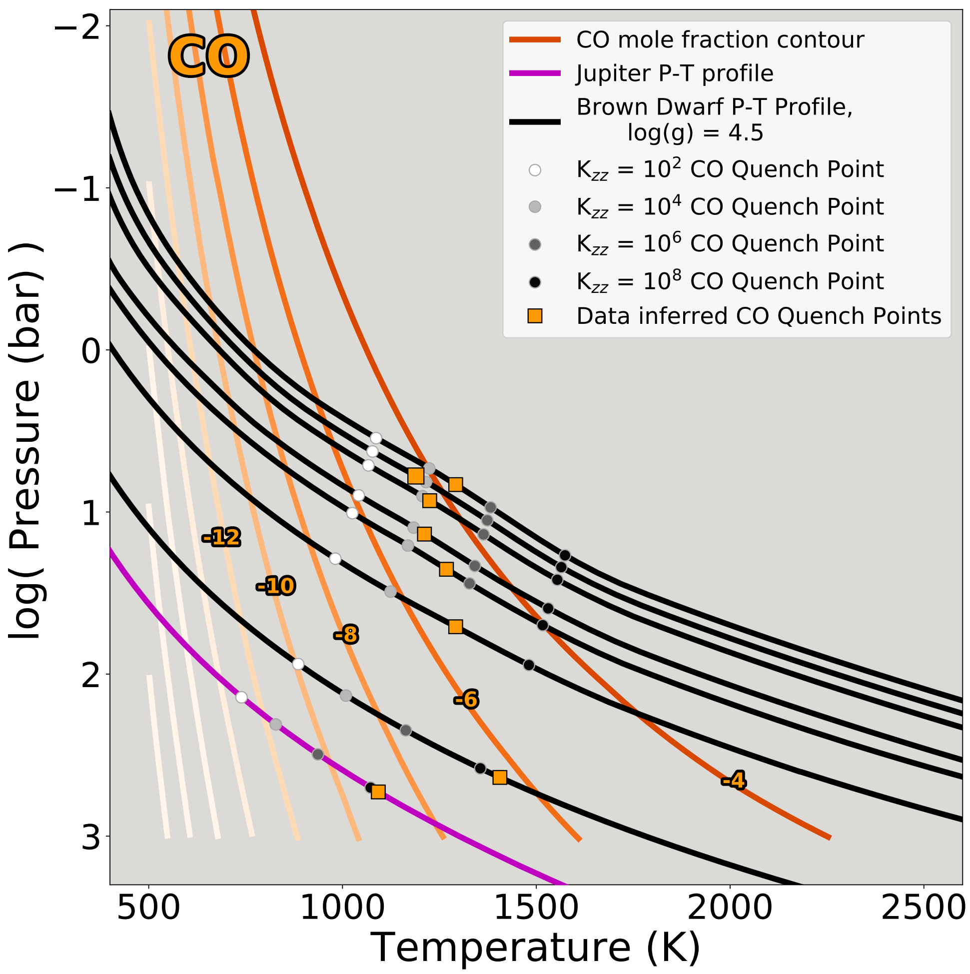

Figure 3.11: This log pressure vs temperature plot contains contour lines of carbon monoxide (CO) mole fractions (orange lines) under equilibrium conditions. The numbers on each orange line represent the exponent value of that mole fraction contour line. Hotter temperatures and pressures correspond to higher abundances of CO. The black lines are pressure-temperature profiles of the adopted log(g) = 4.5 model for each brown dwarf in our sample. From top to bottom the effective temperatures are 750 K (Gl 570D) , 700 K (2M0415), 650 K (WISE 0313), 550 K (UGPS 0722), 500 K (WISE 2056), 400 K (WISE 1541), and 250 K (WISE 0855). Jupiter's pressure-temperature profile (magenta) is created using a hydrogen-helium mixture equation of state form (Chabrier et al., 2019) and structure modeling developed in Thorngren et al. (2016) . Jupiter's P-T profile is below all of the brown dwarf pressure-temperature profiles. The greyscale dots represent quench points for fixed values of K_{zz}. The orange squares are the quench points based on the best fit carbon monoxide enhanced model. Jupiter has a quench point estimate using CO constraints from Bézard et al. (2002). The best fit CO mole fraction tends to decrease at lower effective temperatures, but the amount of mixing required to keep those disequilibrium abundances increases towards lower effective temperatures. Jupiter has a lower surface gravity than the adopted brown dwarfs causing the offset in constant K_{zz} value quench points.

The surface gravities of the brown dwarfs in our sample have not been directly measured, but it is an important parameter for inferring K_{zz} from the data. Warmer brown dwarfs have higher surface gravities for fixed age ranges, which leads to higher values of K_{zz}. However, when accounting for this effect Jupiter and WISE 0855 still have higher K_{zz} relative to their warmer counterparts (Figure 3.12). Since surface gravity is an unconstrained parameter, K_{zz} is inferred for each surface gravity value that exists on the Sonora model grid described in Section 3.4 for all of the brown dwarfs in our sample (Figure 3.13).

3.5.2 CO and Implications for Atmospheric Energy Transport

Brown dwarfs have deep convective interiors and radiative upper atmospheres, which respectively use convective motion and thermal radiation as the primary mode of energy transport (Kippenhahn et al. 2012, Figure 3.14). Brown dwarfs with effective temperatures between 400 K and 750 K have detached upper convective zones with radiative zones in between that could inhibit transport of higher temperature, CO-abundant material into the lower pressure regions of the atmosphere. The radiative zones in between the detached convective zones have steeper temperature gradients that could hinder convection and lower the value of K_{zz} estimated from the CO abundance.

The presence of detached convective zones within our brown dwarfs is explored by estimating the maximum value of K_{zz} possible. We calculate K_{zz} using Equation 4 from Zahnle & Marley (2014), which assumes an object's intrinsic flux the only driving force behind convection. A K_{zz} maximum is estimated for a given effective temperature

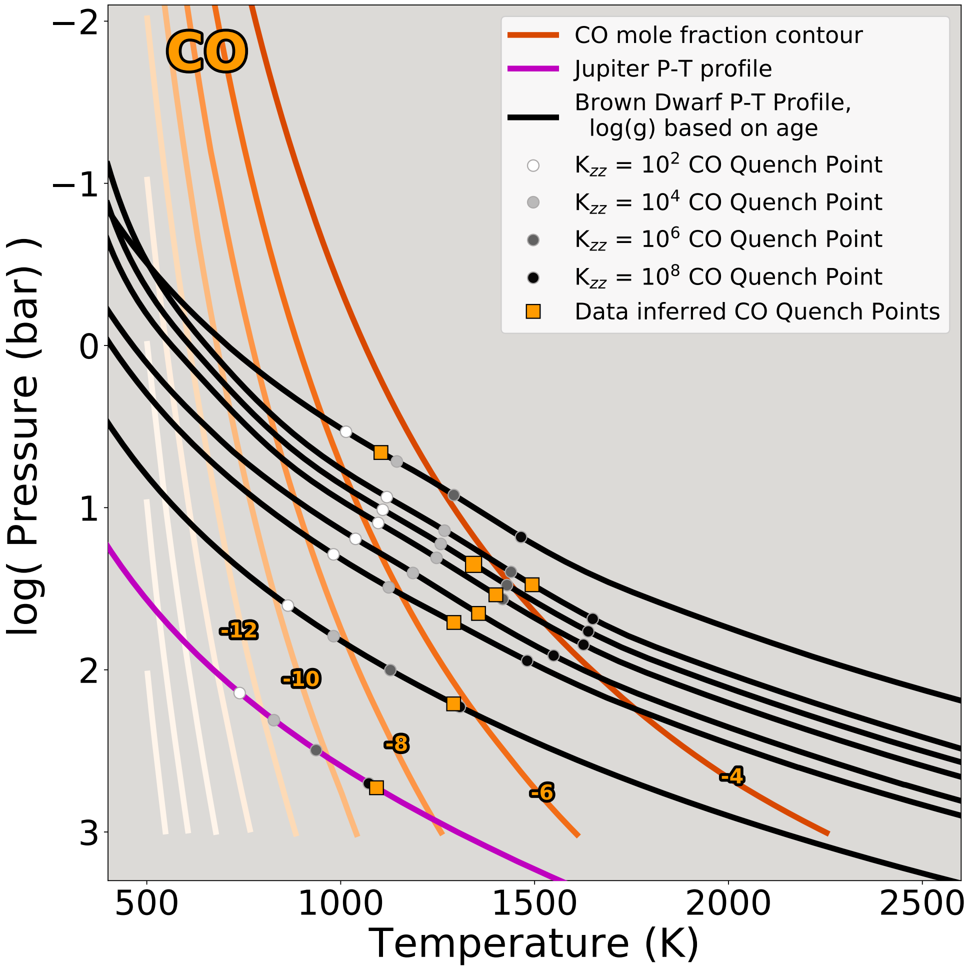

Figure 3.12: Similar labelling as in Figure 3.11. The pressure versus temperature profiles for each brown dwarf, but with different surface gravities based on age (See Table 3.2.) are plotted instead. UGPS 0722 is the upper most P-T profile, due to its lower surface gravity log(g) = 4. The following P-T profiles from top to bottom are Gl 570D (log(g) = 5) , 2M0415 (log(g) = 5), WISE0313 (log(g) = 5), WISE 2056 (log(g) = 4.75), WISE 1541 (log(g) = 4.5), WISE 0855 (log(g) = 4).

and surface gravity, then compared to the CO-inferred K$_{zz}$ values in Figure 3.13. Jupiter and WISE 0855 have CO-inferred K$_{zz}$ values that are near the estimated maximum mixing rate. The warmer ($>$ 400 K) brown dwarfs have K$_{zz}$ values that are up to five factors of 10 below the estimated maximum mixing rate. The CO quench points of the warmer brown dwarfs lie within the radiative zones (Figure 3.14), which could be suppressing the rate of vertical mixing below the theoretical maximum. At 400 K and assuming a log(g) = 4.5, WISE 1541 is supposed to have two convective zones separated by a radiative layer, but uncertainties in gravity and temperature can make the difference between being fully convective and having detached convective zones split by radiative zones. Measured K$_{zz}$ values that are significantly below the theoretical upper limit could be a signature for detached convective zones if this trend is verified in more brown dwarfs and other directly imaged gas giants.

The brown dwarfs in our sample are assumed to resemble the atmospheres of widely separated gas giant exoplanets. Carbon monoxide absorption across the M-band can constrain the atmospheric quenching of gas giant exoplanets, but it also reduces their detectability as shown in Figure 3.6, where larger amounts of CO diminishes the total flux across the M-band (See Figure 4. Saumon et al. 2003). Cold, directly imaged exoplanets and wide companions may have the advantage of being associated with a host star that can be aged and prospects for dynamical mass constraints. This information could reduce the parameter space over which K$_{zz}$ can be estimated for these worlds and maybe even provide the measurements needed to understand the fundamental driving forces behind atmospheric mixing.

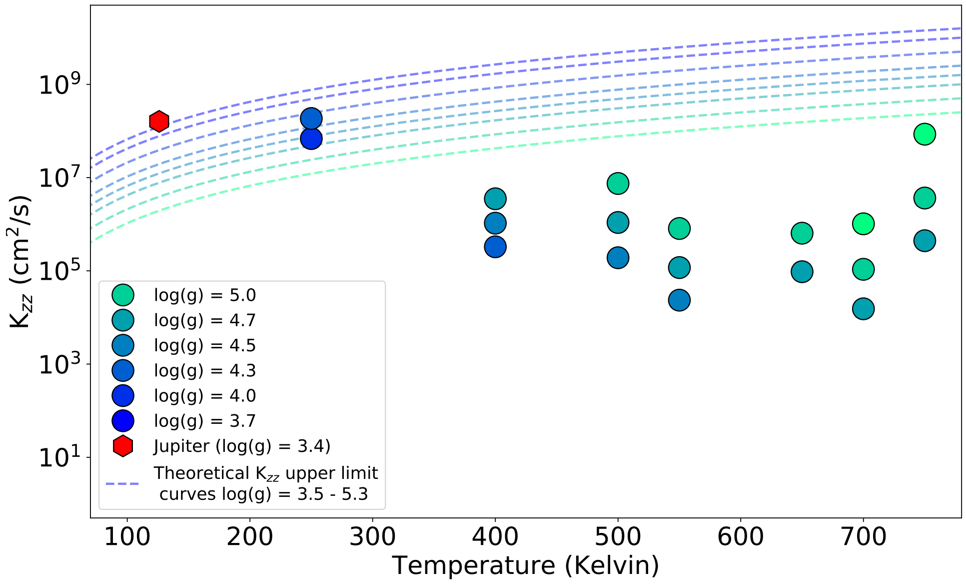

Figure 3.13: The best fit K_{zz} values versus temperature for the adopted models with different allowable surface gravities according to the Sonora Bobcat evolution models. UGPS 0722 (550 K) is plotted as if its allowable age range is 1 - 10 Gyr old. Hotter substellar objects have a wider range of possible surface gravities creating a larger spread in estimated possible K_{zz} values. The dashed lines are the theoretical upper limits of K_{zz} assuming all of the energy from internal heat drives convection. From top to bottom, the theoretical curves correspond to surface gravities of log(g) equal to 3.5, 3.7, 4.0, 4.3, 4.5, 4.7, 5.0, 5.3.

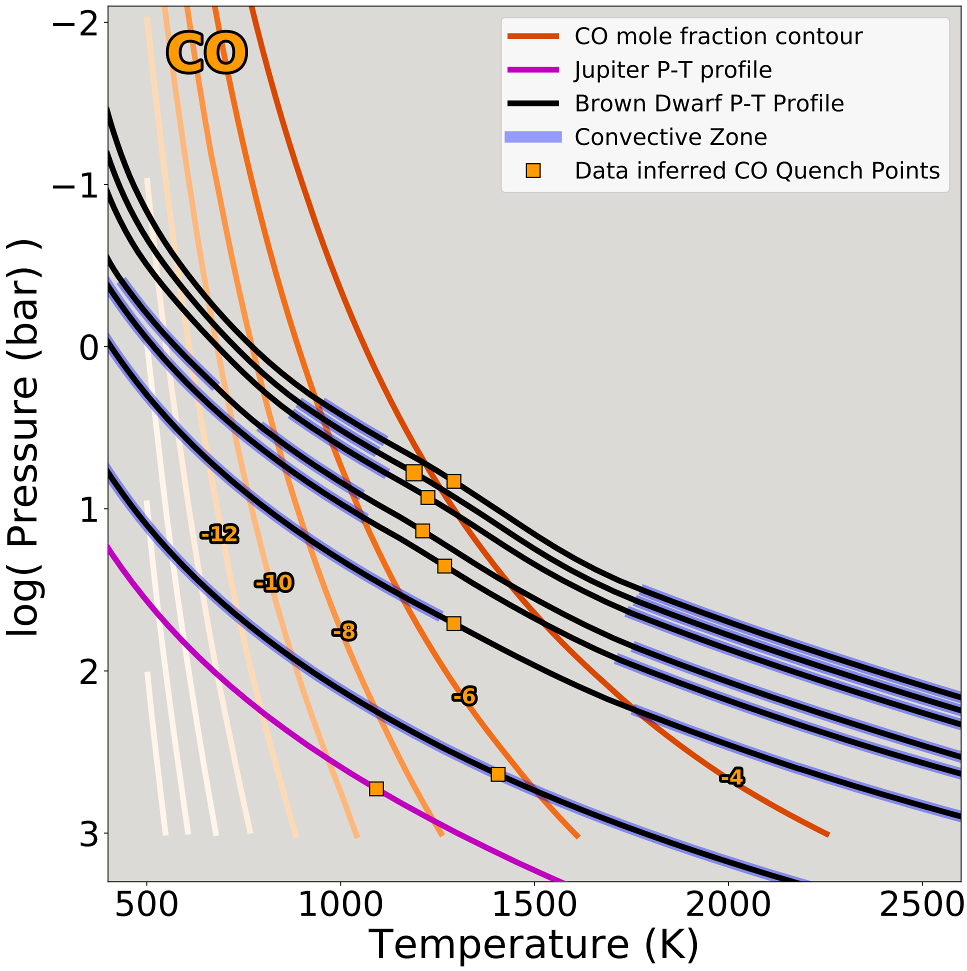

Figure 3.14: Similar set up to Figure 3.11, except the dots of constant K_{zz} are removed and the model defined convective zones are highlighted in blue. For Jupiter and WISE 0855, the inferred quench points lie within convection dominated zones, but for the warmer objects the quench points can occur within a radiation dominated zone.

Object	**Temp** (K)	**best fit CO** log mole fraction	**Inferred K_{zz}** cm^2 s^{-1}	**Inferred PH_3** log mole fraction	**Published PH_3** log mole fraction	**Inferred NH_3** log mole fraction	**Published NH_3** log mole fraction
Gl 570 D	750 K	-4.0	4.9	-6.72	-	-5.3	-
2MASS J0415	700 K	-4.5	3.6	-6.97	-	-5.2	-
WISE 0313	600 K	-4.5	4.3	-6.80	-	-5.1	-
UGPS 0722	550 K	-5.0	4.4	-6.73	-	-4.9	-
WISE 2056	500 K	-5.0	5.3	-6.58	-	-4.8	-4.44
WISE 1541	400 K	-5.5	6.0	-6.26	-	-4.5	-4.43
WISE 0855	250 K	-6.5	8.5	<-6.25	<-6.30	-3.9	-
Jupiter	126 K	-9.0^a	8.2	-	-5.96	-	-3.2

Figure 3.15: Summary of chemical abundances for our sample assuming the adopted temperatures and a log(g) = 4.5 for the brown dwarfs. All values the exponents of the log value. CO abundances are directly measured from the spectra or previously published (a - Bézard et al. (2002)). The PH_3 and NH_3 abundances of Jupiter are compiled in this link here. The inferred NH_3 abundances are from Zalesky et al. (2019). WISE 0855 has an estimate of PH_3 not based on CO from the paper Morley et al. (2018).

3.5.3 Phosphine

Phosphine (PH_3) is a signature of disequilibrium chemistry that has been detected within Jupiter's *L* and *M*-band spectra. Using the K_{zz} values inferred from CO, we estimate the expected abundances of PH_3 for the brown dwarfs and Jupiter. The locations of the PH_3 quench points are shown in Figure 3.16 and the expected PH_3 values have mole fractions from $10^{-6.7}$ to $10^{-6.25}$, quenching at pressures similar to CO. The spread of possible PH_3 abundances are not as large as CO, but the feature should be observable at mole fractions of 10^{-7} in low resolution spectra from 4.5 μm to 4.65 μm (*M*-band) and 4.05 μm to 4.10 μm (*L*-band) (Morley et al., 2018). The vertical mixing inferred from CO tells us that PH_3 should be observable in all of our brown dwarfs, but the wavelengths where PH_3 could be observable occurs in the lowest transmission and lowest signal to noise regions of the spectra. Phosphine absorption is not obvious by eye, however more detailed analysis can place an upper limit on abundances. WISE 0855 should have abundances of PH_3 that are detectable within the Gemini/GNIRS spectra according to estimates in Morley et al. (2018), but it was not seen in the data. Wang et al. (2017) also concluded that a 500 K effective temperature brown dwarf should have a PH_3 mole fraction of $10^{-6.5}$ down to at least log(P) = 3, assuming a K_{zz} of 10^9 cm^2 s^{-1}. Between K_{zz} values of 10^2 to 10^8 the predicted disequilibrium abundance of PH_3 can only change by a factor of 10 for brown dwarfs with effective temperatures of 400 K and above. The abundance contours of PH_3 shown in Figure 3.16 do cross some pressure-temperature profiles twice, which could lead to degenerate measurements of K_{zz} if PH_3 is the only molecule measured. This is not the case for CO because carbon monoxide abundance increases with both temperature and pressure.

3.5.4 Ammonia

The onset of ammonia (NH_3) is supposed to be a defining feature of Y-dwarfs because of their cooler effective temperatures and like PH_3 it offers another element to understand the composition of brown dwarfs and exoplanets. Disequilibrium abundances of NH_3 have been previously detected in near- and mid-infrared brown dwarfs spectra (Saumon et al., 2007; Geballe et al., 2009; Leggett et al., 2010, 2015). We also estimate the abundances of NH_3 based on the K_{zz} values inferred from CO. The predicted quench points of NH_3 for specific values of K_{zz} from CO are shown in Figure 3.17. Below a pressure of 1 bar, the contour lines of NH_3 abundances are almost parallel with the pressure temperature profiles. This implies that NH_3 is a strong indicator of effective temperature and comparatively less sensitive to atmospheric quenching with respect to CO and PH_3, which is in agreement with the results of Saumon et al. (2006).

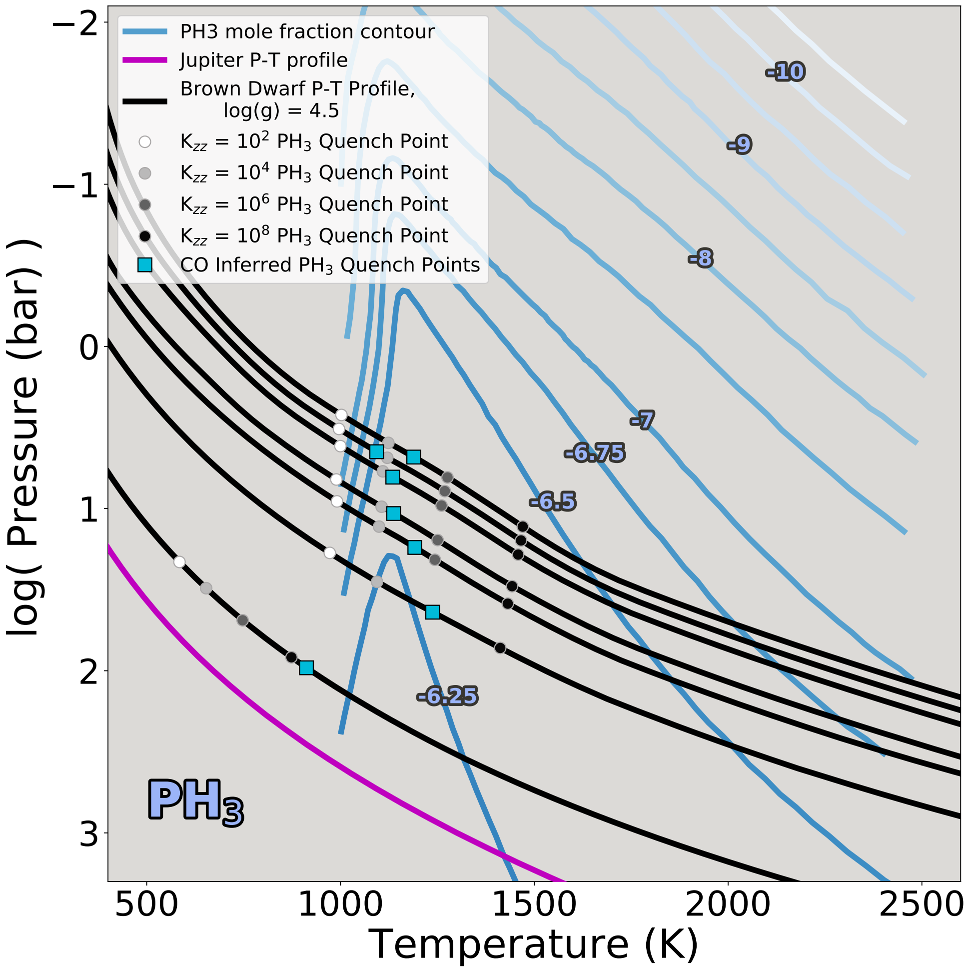

Figure 3.16: Similar labeling convention as in Figure 3.11, but the blue contour lines are the mole fractions of phosphine (PH_3) and the blue squares/triangle represent the inferred quench points of PH_3 based on the K_{zz} values calculated from CO. All of the brown dwarfs should have relatively high values of PH_3 in their atmosphere as predicted in Morley et al. (2014), yet the L and M-band spectra do not show strong PH_3 absorption. Jupiter's PH_3 quench points occur in lower pressure and temperature regions outside of this plot

From K_{zz} values of 10^2 cm^2 s^{-1} to 10^8 cm^2 s^{-1} the abundance stays within a factor of 10 for warmer objects, but this may be less true for cooler objects such as Jupiter. The estimates for NH_3 (Table 3.15 based on CO are consistent with the NH_3 abundances derived from retrievals for WISE 2056 and WISE 1541 computed in Zalesky et al. (2019).

At equilibrium, the nitrogen abundance is primarily dictated by the balance between N_2 and NH_3, but there are minor nitrogen bearing gases such as HCN that affects where when the quenching point occurs at high pressures and temperatures (Lodders & Fegley, 2002; Zahnle & Marley, 2014). Minor nitrogen bearing gases are only expected to change the abundance of NH_3 by $\sim$ 10% or so, which may be difficult to detect with the ground based data that is typically published, but an effect to consider in the high quality spectra that will be taken with JWST. HCN does have distinct opacity signatures across the 3 μm - 5 μm range as shown in Morley et al. (2018), but the opacity per molecule is strongest at longer wavelengths with strong signatures at $\sim$7μm and $\sim$14μm. MIRI/JWST and longer wavelength instruments offer opportunities to understand the nitrogen chemical networks in brown dwarfs and gas giant exoplanets.

3.6 Summary

In this paper we combine new Gemini/GNIRS data and previously published *M*-band spectra to create a temperature sequence of 8 gaseous objects: Gl 570D, 2M 0415, UGPS 0722, WISE 0313, WISE 2056, WISE 1541, WISE 0855, and Jupiter. Our sample covers 750 K to 126 K, starting with brown dwarfs within the effective

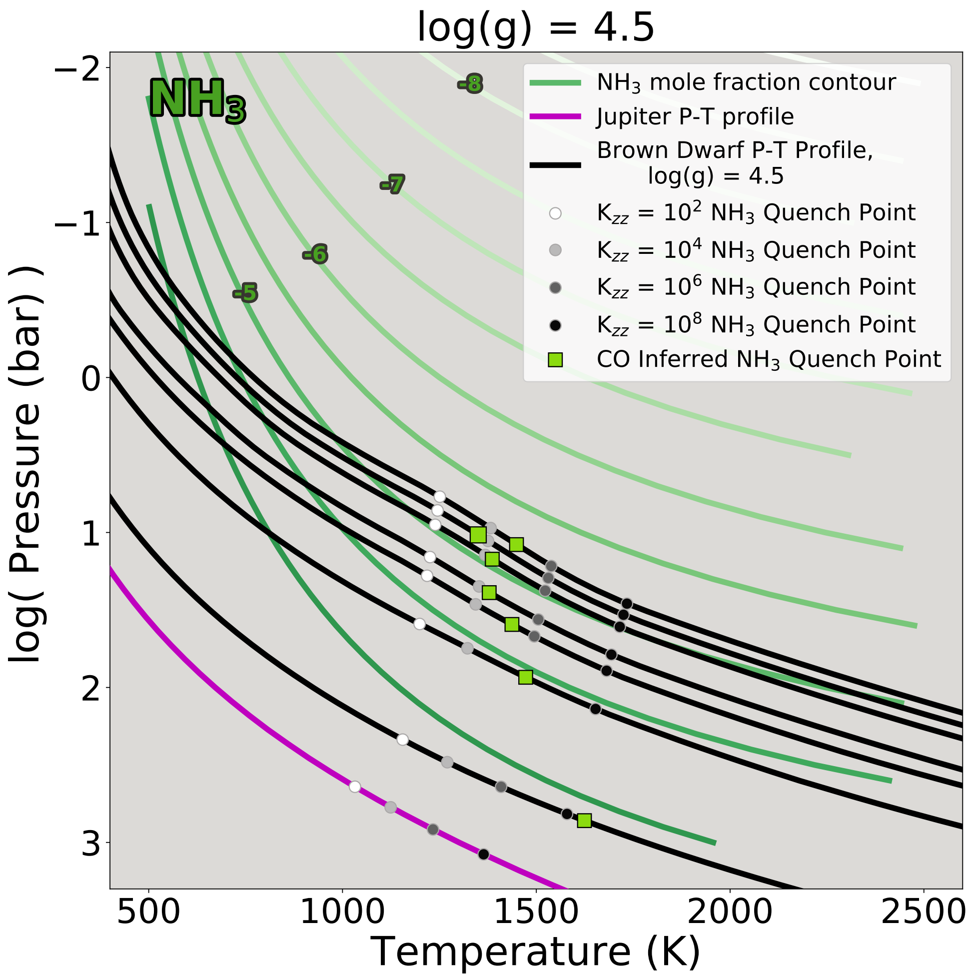

Figure 3.17: Similar labeling convention as in Figure 3.11, but the green contour lines are the mole fractions of ammonia (NH_3) and the green squares represent the inferred quench points of NH_3 based on the K_{zz} values calculated from CO. The NH_3 mole fraction contours run almost parallel with some of brown dwarf pressure-temperature profiles, therefore NH_3 abundances are somewhat insensitive to atmospheric mixing over the typical K_{zz} values in a gas-giant object.

temperature range of the current coldest directly imaged companions (ex. 51 Eri b, GJ 504b), extending into the regime of could-be discovered exoplanets, and ending with our Solar System's largest gas giant, Jupiter. Enhanced abundances of carbon monoxide are detected in all of our objects and mole fractions between 10^{-4} - 10^{-7} are needed to better fit the spectra. Clouds and enhanced carbon monoxide were shown to improve the spectral fitting for WISE 0855.

The best fit CO values are evidence for convection driven, disequilibrium chemistry and the eddy diffusion coefficient (K_{zz}) is estimated for each object based on those abundances. The estimated K_{zz} values of the sample spans from 10^4 cm^2 s^{-1} to $10^{8.5}$ cm^2 s^{-1}. The coolest objects in our sample, WISE 0855 and Jupiter, have estimated mixing strengths close to their theoretical upper limit, while brown dwarfs 400 K and warmer mix below this limit. This may be due to the presence of a predicted radiative zone at temperatures greater than 1100 K in the warmer atmosphere. Brown dwarfs and directly imaged gas giant planets are mostly convective, but warmer, higher gravity objects have detached convective zones, where mixing could be less efficient within the radiative layer and this is supported by our observations.

Using the estimated K_{zz} values from CO, predictions are made for phosphine and ammonia. All of the brown dwarfs should have detectable mole fractions of PH_3 between $10^{-6.7}$ to $10^{-6.25}$, but none of them show obvious absorbprtion within the *M*-band or previously published *L*-band data. In addition to this, we may not understand the behavior of phosphorous bearing molecules deep in the atmosphere of brown dwarfs. Ammonia is relatively insensitive to atmospheric mixing and our values of predicted NH_3

based on CO estimates are consistent with the retrieval analysis published in Zalesky et al. (2019). The chemical abundances of PH_3 and NH_3 will be best constrained with the medium resolution (R∼1,000), high signal-to-noise spectroscopy that can be achieved with JWST.

Directly imaged, gas giant exoplanets are often targeted while young, have lower surface gravities, and condense clouds at lower pressures than similar effective temperature brown dwarfs. Because of this, directly imaged exoplanets may be susceptible to atmospheric quenching and a delayed onset temperature for water clouds compared to brown dwarfs (Morley et al., 2014). The prevalence of CO in objects that are likely older than a 1 Gyr old suggests that disequilibrium CO absorption may be common in colder gas giant exoplanets. Excess CO absorption not only has implications for atmospheric characterization, but the overall detectability of these objects in planet finding surveys. More robust K_{zz} estimates and tests of atmospheric physics could be made if larger numbers of substellar companions and directly imaged planets with age or dynamical mass constraints can be characterized. Cool brown dwarfs are excellent testing grounds for refining our atmospheric models and making predictions for observations of directly imaged exoplanets. Future mid-infrared spectroscopic studies of brown dwarfs and directly imaged gas giants will continue to expand our understanding of atmospheric chemistry and physics in gaseous objects.

Between the graduate student wild cat strike, COVID-19 pandemic, Santa Cruz wild fires, my own health issues, and my detector breaking shortly before my thesis defense, planning the end of my graduate career has often felt extremely pointless. I'm thankful for mentors, friends, and family that remind me to take things one step at a time and carve out joy for myself.

"Trouble in my way
I have to cry sometimes"
- Ira Tucker, Trouble in My Way

Chapter 4

Testing a 10 micron HgCdTe Detector for Ground-Based Exoplanet Science

4.1 Introduction

The contrast necessary to image an Earth-like planet around a Sun-like star is $\sim 10^{10}$ in the visible but only $\sim 10^{7}$ in the mid-infrared (10μm Figure 4.1). As a result, mid-infrared imaging of Earth-like exoplanets will be possible from the next generation of extremely large telescopes (Wagner et al., 2021). Extending our conventional wavelength coverage further into the mid-infrared gives us the ability to characterize a variety of trace gases in the atmospheres of both Earth-like and gas giant exoplanets. In Earth-like planets gases like water (H_2O), ozone (O_3) and carbon monoxide (CO_2) can be detected at resolutions as low as ~ 20 (Kaltenegger et al., 2007). For gas giant planets, ammonia (NH_3) is detectable in the mid-infrared and is important

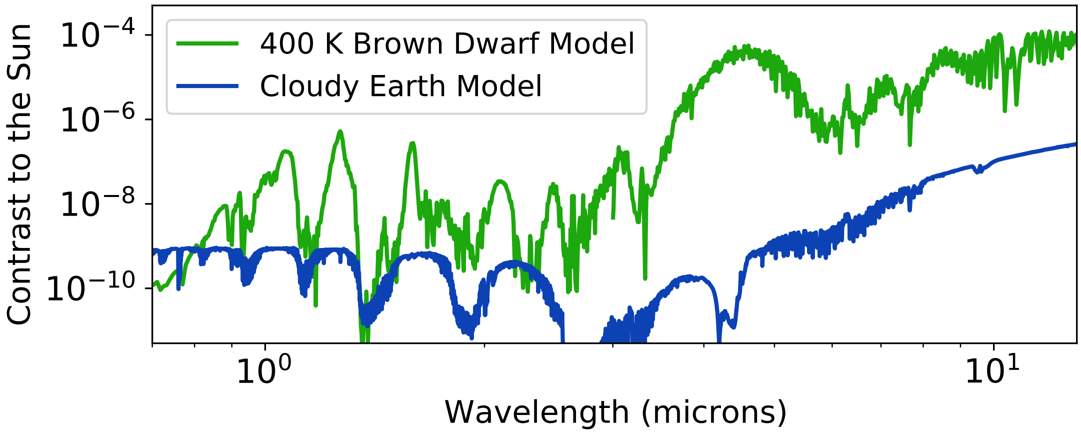

Figure 4.1: Contrast of an Earth model (blue) and a 400 K, cloudless brown dwarf (green) to the Sun, a G2V type star. The Earth model and brown dwarf models are from Madden & Kaltenegger (2020) and Marley et al. (2021) respectively.

gas estimating the nitrogen abundance in these planets (Morley et al., 2014). Colder exoplanets also emit a significant fraction of their luminosity within the mid-infrared, which is useful for placing constraints on their bolometric luminosity and evolutionary history. Detecting and characterizing new exoplanets in the mid-infrared also involves understanding which detectors are best suited for accomplishing these scientific goals.

Several mid-infrared detectors have been developed, but the most commonly used type in astronomical instruments are arsenic doped silicon (Si:As) impurity band conduction detectors (IBC). The IBC Si:AS detectors do well in applications with low background noise such as outer space, but on the ground these detectors suffer from excess low frequency noise (ELFN) (Pipher et al., 2021; Crawford et al., 2006; Arrington et al., 1998). ELFN can be mitigated with chop-nodding, however this reduces the overall efficiency of the observation by a factor of four. Recently, long mid-infrared HgCdTe detectors have been developed primarily for the space-based mission NEO

Surveyor (formerly NEOCam) (Cabrera et al., 2019, 2020), which may be applicable for exoplanet imaging. The differences between IBC Si:As and HgCdTe detectors affect how the two devices should be operated and their potential performance within astronomical instruments. At near-infrared wavelengths HgCdTe detectors have not been observed to have ELFN noise, which may be due to their different pixel structure compared to IBC Si:As detectors. The ELFN present in IBC Si:As detectors is typically attributed to the blocking layer in the pixels (Stapelbroek et al., 1984), which is not present (or depicted) in schematics of a HgCdTe pixels Rieke (2007). If mid-infrared HgCdTe detectors do not have ELFN they would be more sensitive to faint exoplanets than IBC Si:As detectors. Ground-based extremely large telescopes will still need at least an hour to detect an Earth-like planet around the nearest stars[Wagner et al. (2021)], therefore maximizing observational efficiency is important for Earth-like planet hunting.

The average well depth of a IBC Si:As detector is usually four to five times larger than the average well depth of a mid-infrared HgCdTe detector. For example, the IBC Si:As detectors used for MIRI on JWST have a full well depth of $\sim$ 250,000e-[1], whereras the mid-infrared HgCdTe detector we are testing has a minimum well depth of 59,000e-Cabrera et al. (2019). On the ground, this means that HgCdTe detectors saturate quicker and are limited to finer pixel scales when operating. In instruments designed to detect Earth-like planets around nearby stars, smaller fields of view are acceptable. Combined with fast readouts to mitigate the sky background, HgCdTe detectors may be an option for mid-infrared exoplanet imaging.

---

[1] https://jwst-docs.stsci.edu/mid-infrared-instrument/miri-instrumentation/miri-detector-overview

The 1024 by 1024, mid-infrared HgCdTe detector we are discussing in this paper was developed and created by the University of Rochester Infrared Detector team and Teledyne Imaging Systems Cabrera et al. (2019). The detector's wavelength cutoff is 12.8 μm, making it sensitive across the atmospheric window where we hope to directly image Earth-like planets. In order to test this detector's usability we create a 1-to-1 imaging system that would work behind a 30 meter telescope within a cryostat. The cryostat has a filter set for testing the detectors sensitivity and quantum efficiency at 2.3 μm, 5.3 μm, between 8 μm - 12 μm, and 10 μm to 12 μm. We are interested in this detector's use over a broader wavelength coverage because the original characterization paper array Cabrera et al. (2019) made a broad quantum efficiency measurement from 6 μm - 10 μm. The read out electronics chosen to reach high read out speeds are the SIDECAR ASIC (Teledyne Scientific) and a MACIE Card (Markury Scientific). In this paper, we estimate the required imaging system focal ratio required to avoid sky background saturation on the detector. Next we explain the purpose and operation of the electronics used to read out the detector We then explain modifications needed to retrofit the former Keck Angle Tracker for cryogenic detector testing. We discuss the initial room temperature results of the detector being read out at exposure times as low as 11ms. Lastly, we describe the first cryogenic test of the read out electronics with a 2048 by 2048 multiplexer and plans for our cryogenic testing of the detector.

4.2 Detector Re-Imaging System

To test the long wavelength HgCdTe device, we have modified an existing cryostat. The cryostat has been retrofitted it with cabling, mounts, and optics to approximate a similar camera that might be used on extremely large telescopes and we discuss below the design considerations for assembling this setup.

4.2.1 Required Focal Ratio

As a starting point for the optical design, we estimate the focal ratio needed to match the detector well depth. The amount of sky background that collects on a pixel is determined by the solid angle that pixel takes up on the sky. The solid angle of a pixel is only set by the focal ratio of the telescope and we estimated the focal ratio that allows images to be taken on the detector without saturation. The focal ratio is set by a cold stop that limits the field of view and the power falling on the detector. The ideal focal ratio was estimated by calculating the amount of sky background and dark current per pixel the detector experiences as a function of focal ratio. The sky background is based on the Maunakea site published by Gemini Observatory[2]. The sky background flux per area is multiplied by the transmission of an uncoated zinc selenide lens (transmission ~ 70 %) and a broad 8 μm to 12 μm (transmission ~ 90 %) filter before reaching the detector. The sky background flux per area is multiplied by the pixel size to calculate the amount of sky background that collects on each pixel. The dark current (dependent on temperature) is added to the sky background for the total e- noise rate per pixel.

---

[2] https://www.gemini.edu/observing/telescopes-and-sites/sites

The total e- rate is multiplied by the integration time to estimate how many electrons are produced in a pixel.

Knowing the maximum flux that can be collected on a single pixel is important for estimating the minimum focal ratio allowable for the imaging system. This limit can be estimated using the minimum well depth per pixel published in Reference Cabrera et al. (2019) (Detector #18367) for our detector is 59k e-. Focal ratios that produce per pixel background lower than this e- value are viable for cryostat testing and an exoplanet imaging system. The background as a function of focal ratio is shown in Figure 4.2. While operating at a temperature of 33 K, the smallest focal ratio this detector could be run at behind is ∼f/20. This corresponds to a maximum field of view (on one side) of 5 arcseconds on a 30 meter telescope. The field of view is small, but acceptable for imaging Earth-like planets with small separations around the nearest stars. In the future, a more precise focal ratio can be chosen for specific exoplanet survey/detection reasons, but for demonstration purposes we go with a f-number of 100 which is a factor of 10 below the minimum well depth after a 20 millisecond integration.

4.2.2 Filter Set

We have chosen filters that span from 2 μm to the detector cutoff at 12.8 μm. This wavelength range will allow us to understand the performance and drawbacks of using such a detector shortward of the 8 μm -12 μm region for which it was designed. The filter set for detector testing is composed of off the shelf optics that fall into or near Earth's infrared atmospheric transmission windows (Figure 4.3). The four filters include

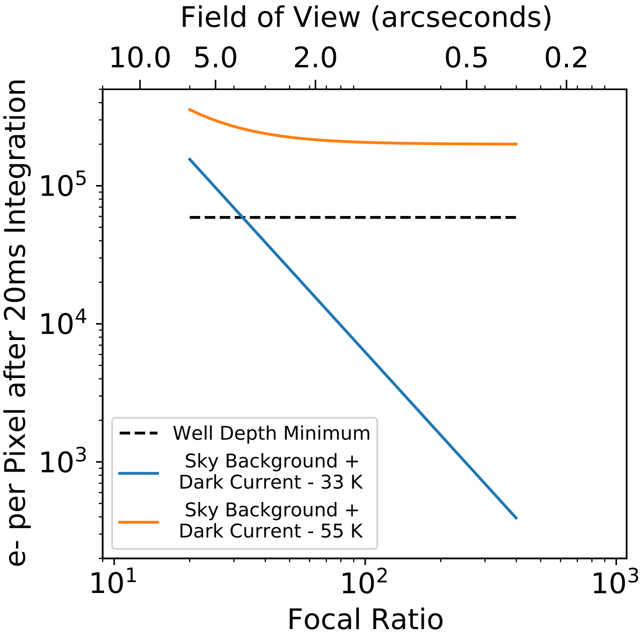

Figure 4.2: Estimated amount of electrons per pixel for a 20 millisecond exposure for a given focal ratio/field of view. The blue curve assumes a detector temperature of 33 K. The orange curve assumes a detector temperature of 55 K. Larger field of views lead to faster focal ratios and higher risk of saturation on the detector. At a high enough temperature the dark current dominates signal on the detector no matter the focal ratio. At 33K, the smallest focal ratio acceptable is about 30.

a narrow 2.3 μm filter, narrow 5.3 μm filter, 10 μm - 12 μm filter, and a broader 8 μm to 12 μm filter. Infrared blockers were purchased to use with 2.3 μm and 5.3 μm filters because the filters do not have perfect suppression of infrared light longer than 2 μm. The excess infrared light allowed through the 2.3 μm and 5.3 μm filters was estimated using a 800 K blackbody. Without blockers, a quarter of the light measured through the 2.3 μm filter would be infrared leakage. For the 5.3 μm filter, this value is 3.8%. By using a fused silica blocker is in series with the 2.3 μm filter, wavelengths longer than 4 μm can be suppressed and the detector's quantum efficiency can be measured to about 8.4% in this filter. The 5.3 μm filter is used with a sapphire blocker, to block light longward of 7μm to measure the detector's quantum efficiency to about 3.3%. The 10 μm filters do not need infrared blockers because the excess infrared light allowed through these filters at an ambient clean room temperature of 297 K would only influence the quantum efficiency measurements by 0.5%.

4.2.3 Imaging System

The optics are arranged to re-image objects directly outside of the cryostat on the detector with a magnification of 1. This is done with an uncoated, 100 mm focal length, plano-convex zinc selenide lens. A cold stop is placed one focal length away from the lens to set the focal ratio of the system and control the amount of light that falls onto the detector. A filter wheel is placed behind the entrance window/lens before the cold stop within the cryostat. A simplified version of this is shown in Figure 4.4. Inside of the cryostat a gold-coated, aluminum flat mirror is added after the cold stop to fit

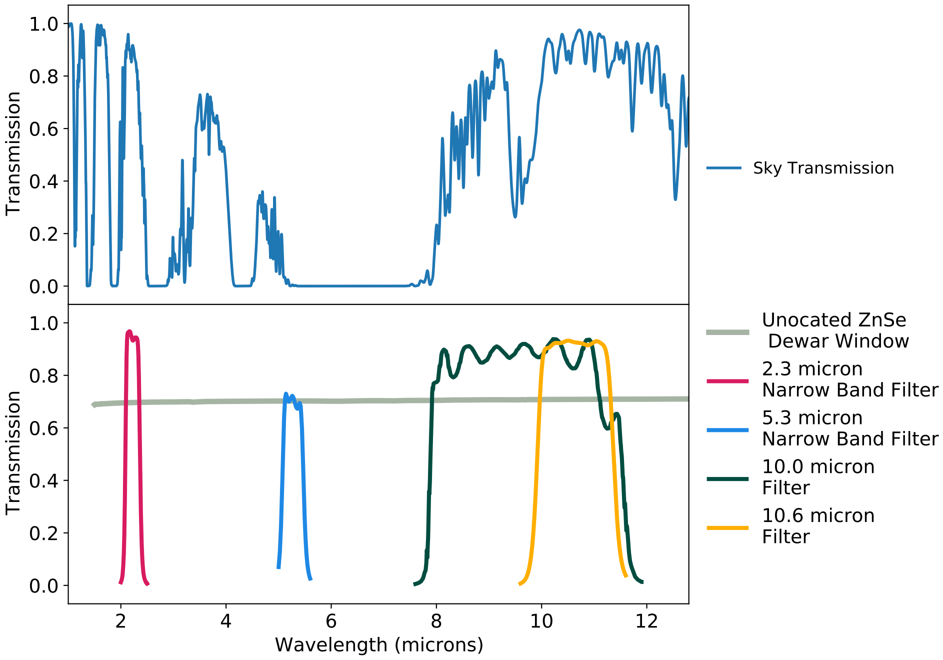

Figure 4.3: (Top) Atmospheric sky transmission from the near infrared to mid infrared at sea level. (Bottom) The transmission profiles of the filter set and the entrance lens of the cryostat. The filters were chosen to be near or within infrared atmospheric windows.

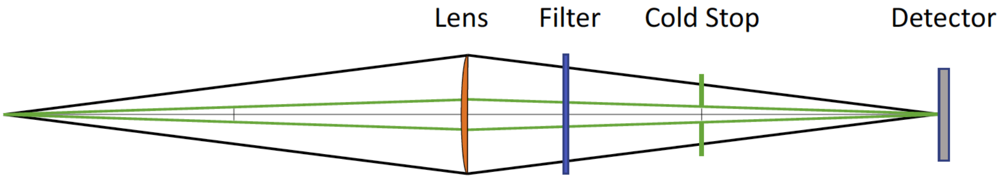

Figure 4.4: Schematic of the optics used to image objects in front of the cryostat on to the detector. Light travels from left to right through the lens, filter, cold stop then falls on the detector. The cold stop (not to scale) is used to set the focal ratio of the system by limiting the possible angles of light than enter the system. The outer, black lines indicate the range of light allowed on the detector without a cold stop. The green lines creating a smaller cone show the spread of light allowed through a potential cold stop.

the optics and electronics on the cold plate. The filter wheel is slightly offset from the central path of the detector and entrance lens, but this is not an issue given the system will be run at higher f-number. To create a f/100 system the cold stop needs to have a 1mm diameter.

4.3 Detector Read Out Electronics

Images of the detector are read out using electronics that have cryogenic and room temperature components. A flow chart of the components are shown in Figure 4.5. HxRG detectors typically have two clocking modes for reading out the array, “slow mode” and “fast mode”. Slow mode has a typical pixel rate of 100kHz, while fast mode has a typical pixel rate of 5 MHz. The cost of running fast mode is higher read noise and a factor of 100 more power output compared to slow mode. The HgCdTe H1RG we are testing for this project is not able to operate in fast mode. Additional hardware and new firmware were needed to make use of a “hybrid fast mode” where the detector is run in slow mode while the read out electronics are still configured as if they were in fast mode. The additional hardware required was a board (called the buffer board) purchased from Teledyne that lowers the overall resistance on each output channel for a set of pixels to read and reset more quickly at the cost of more power to operate in this mode. In un-buffered mode cross talk between pixels is more likely at higher frequencies, because a buffer is not present to help isolate the pixels and the output (Bezawada et al., 2020).

Inside of the cryostat, the detector is connected to the SIDECAR ASIC through a cable and the buffer board. The SIDECAR ASIC is connected to the room temperature MACIE card by a cable that runs through the cryostat wall. The SIDECAR ASIC is used to operate the detector by setting clocking speeds, several reference voltages/currents and digitizing the output signal from the detector. The offset voltage and the gain on the pre-amplifier are the primary settings changed on the SIDECAR ASIC for detector images. The MACIE Card is used to control the firmware,settings, and registers on the SIDECAR ASIC and the board has a GUI to read out the detector.

Hybrid fast mode is used to achieve the read out speeds needed to overcome the sky or clean room background since the detector cannot be operated in true fast mode. The hybrid fast mode firmware runs the SIDECAR ASIC with the 12 bit (instead of 16) analog to digital converter with extra power supplied by the buffer board for 1MHz pixel rates. Without reaching exposure times less than .1 seconds, the potential field of view of instruments that could use mid-infrared HgCdTe detectors would be severely

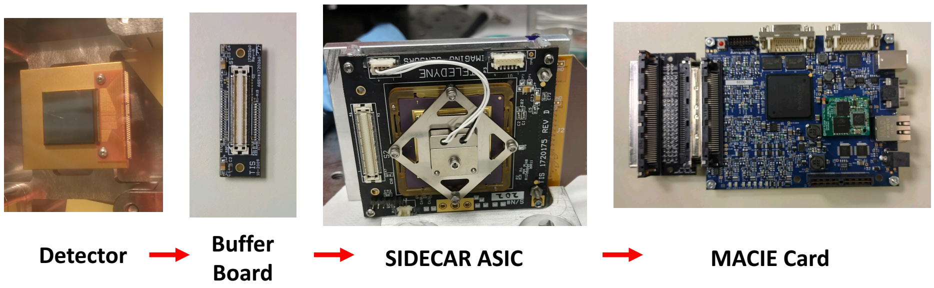

Figure 4.5: Flow diagram of components used to read out the detector. Cables of components are not depicted. (Left to Right) The HgCdTe detector captures the infrared light. The buffer board helps the pixels on the detector to reset quickly for hybrid fast mode. The SIDECAR ASIC amplifies and digitizes the signals from the detector. The MACIE Card is used to control the SIDECAR ASIC through a GUI interface on a computer.

limited. Hybrid fast mode and eventually true fast mode are essential for enabling the potential science that can be done with HgCdTe detectors in the mid-infrared.

4.4 Detector Cryostat Set Up

4.4.1 Electronics

The cryostat used for detector testing was formerly the Keck Angle Tracker (Crawford et al., 2006) and it needed to be repurposed for this project. The wires used for detector focus platform limit switches and homing switch of the filter wheel were converted for reading out 2 DT-470 Series Silicon Diode temperature sensors with a Lakeshore monitor. One temperature sensor is attached to the cold plate and the other temperature sensor is placed on the molybdenum block that is in thermal contact with the detector.

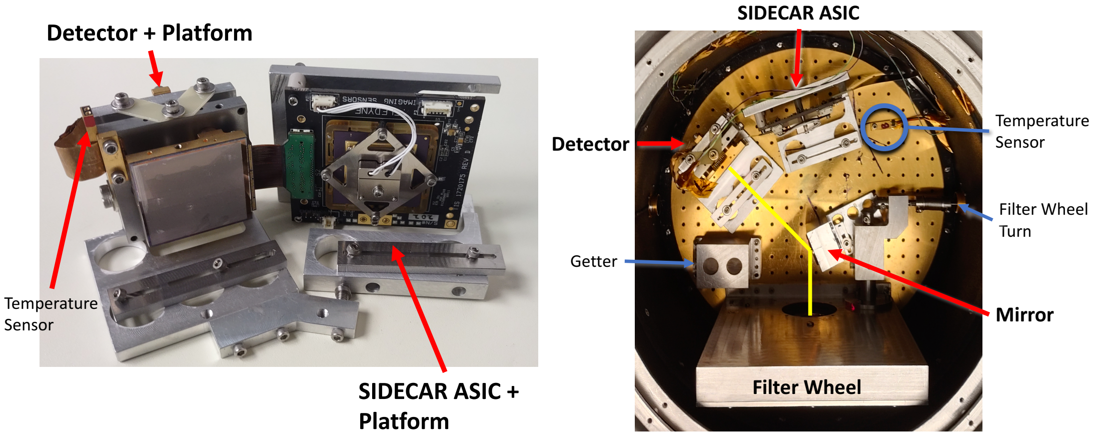

Figure 4.6: (Left Image) The detector and SIDECAR ASIC mounts. In the photo, a 2048 by 2048 multiplexer (MUX) is mounted for testing the electronics. (Right Image) Layout of the optics and electronics on the cryostat cold plate. The yellow line marks the optical path from the outside of the cryostat, through the filter wheel, off the mirror onto the detector.

The old left side detector port (Top right hole in Figure 4.6) had its radiation shield hole expanded to allow the SIDECAR ASIC to MACIE cable to pass through the cryostat wall. A new feed through for the cable was created to fit the current screw holes. The cable was potted into the feed through using room temperature vulcanizing (RTV) silicone on the warm (external) half, the cold half (internal) was potted using Stycast 2850-FT mixed with microspheres.

4.4.2 Optics

The cryostat window was originally a flat circle of fused silica and needed to be changed to a material that transmits at wavelengths longer than 2 microns and has power for re-imaging objects onto the detector. A new lens holder was created to seat

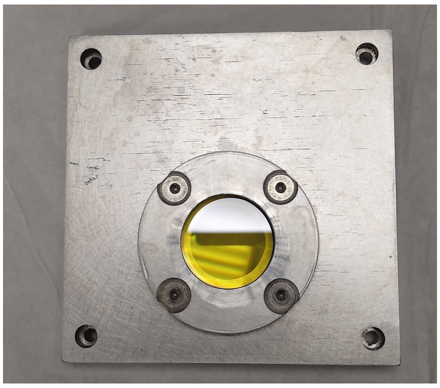

Figure 4.7: The modified entrance lens for the cryostat. The uncoated zinc selenide lens held to the metal base with a circular retainer.

the plano-convex ZnSe lens along the optical axis of the detector. The ZnSe lens is sandwiched in between two o-rings for a vacuum seal and held against the cryostat with a circular retainer (Figure 4.7). The filter wheel that came with the cryostat has 1.5 inch diameter slots. Holders and spacers needed to be made for the undersized filters and blockers used for this project. The 1 inch 10.0 μm and 10.6 μm filters are placed into metal holders that drop into the original 1.5 inch slots. The 2.3 μm and 5.3 μm filters have holders combined with with metal spacers to hold blockers in the original slots (Figure **??**). The 1 inch mirror is mounted on an L-shaped bracket by three screws with a ball pivot point to allow for adjustments. No isolated photos of the mirror mounter were taken but it can be seen in the center of Figure 4.6. Isolated pictures of the filters and entrance lens optics are shown in Figure 4.9. The sapphire and silica blockers are clear disks that look identical.

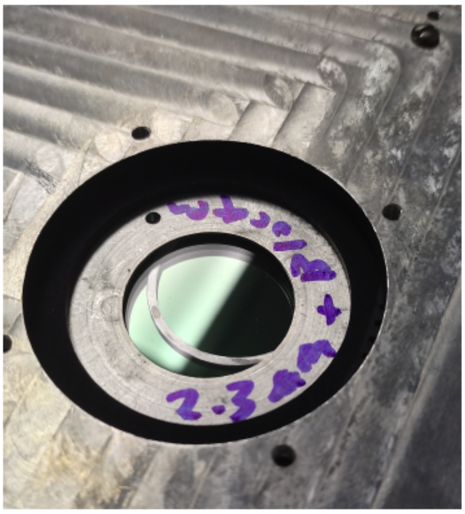

Figure 4.8: This figure depicts a filter within the filter wheel of the cryostat. The filter holder is the metal donut shape with the filter labeling in blue sharpie. In between the blocker (clear, top layer) and the filter (blue, below) there is a thin metal ring that separates the blocker and filter. This photo shows a poorly fit version of the spacer, but it makes clear how the components are layered. In the current set up, the spacer connects the blocker and filter at the outer circumference of the small diameter optic (typically the blocker) and would not be visible without opening the filter holder.

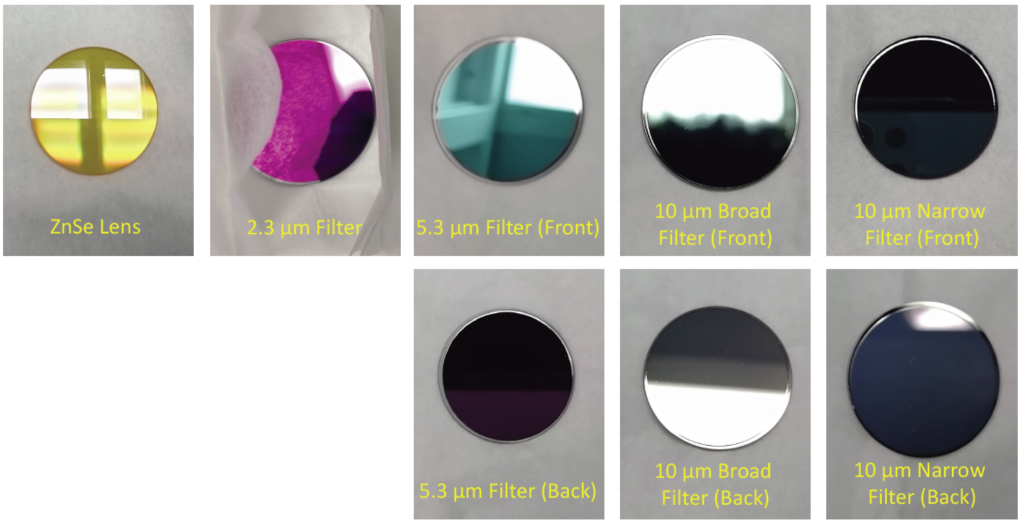

Figure 4.9: The lens and filters used in detector imaging system. The Zinc Selenide (ZnSe) lens is plano-convex. The filters and lenses are not shown on the same scale. The back of the 2.3 μm filter was not taken in isolation but it is shown in Figure 4.8.

4.4.3 Detector and SIDECAR ASIC Mounts

The mount holding the detector needs to thermally isolate the electronics from the cold plate and prevent any conduction between the detector and the cryostat itself. The detector should not cool faster than about 1K per minute and needs to be attached to a material that has a similar coefficient of thermal expansion (CTE). Molybdenum matches the CTE of the detector and was chosen as the mounting block. The molybdenum block is attached to the cold plate base using triangular G10 stand offs(4.6) and provide thermal isolation. A thin copper strap connects the molybdenum block to the the detector mount base, letting heat to transfer between the mount and the molybdenum block/detector at a relatively controlled rate. The SIDECAR ASIC is mounted to its base using polyether ether ketone (PEEK) standoffs to keep it insulated from the cryostat's cold plate. Cooling too quickly was not a significant concern for the SIDECAR ASIC. A temperature sensor is attached directly to the molybdenum block to make sure the detector is not cooling to quickly and estimate the operating temperature of the detector. The SIDECAR ASIC has temperature sensors within the circuit board, but reading them has not been enabled yet.

4.5 Readout and Detector Testing

All cold detector testing has not been completed, however room temperature and some cryogenic runs have been done to test the detectors general operation in slow mode and hybrid fast mode with the buffer board. The detector cannot operate in the

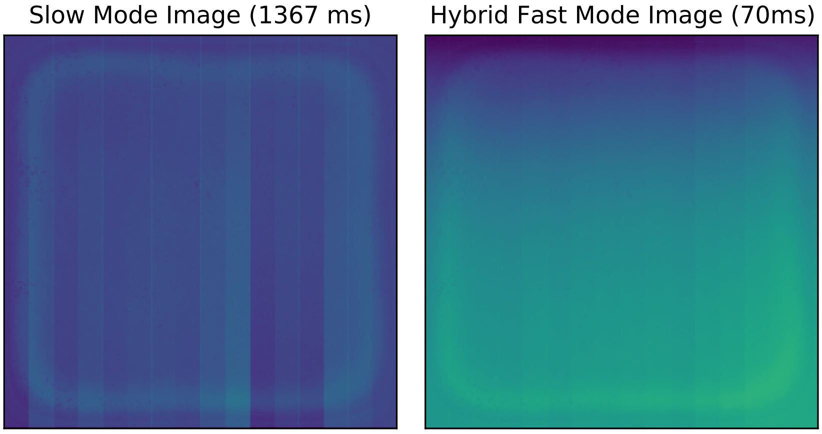

Figure 4.10: Single read out the HgCdTe detector at room temperature in slow and hybrid fast mode.

traditional fast mode setting at room temperature. Figure 4.10 shows images of the detector in slow (1367 ms) and hybrid fast mode (70 ms). The detector picture frame can be seen in both slow and fast mode. The hybrid fast mode appears smoother and has an amplitude gradient from top to bottom of the array but the offset and gain settings between the slow and fast hybrid mode are different so a one to one comparison is difficult without any further image reduction.

4.6 Cryogenic MUX testing

The MUX shown in Figure 4.6 was used to test the detector read out electronic's operability at cryogenic temperatures before use with the detector. The first test used liquid nitrogen to cool the cold plate and optics down to 77K. At this cold

Exposure Time (ms)	MACIE Clock Driver (MHz)	ASIC Mode	Worked? (Y/N)	Comments
70.7	10	Fast	Y	
35.4	20	Fast	Y	
23.6	30	Fast	Y	Lines between the output “channels”
17.7	40	Fast	Y	Lines between the“channels”
14.4	50	Fast	Y	Lines between the “channels”
11.8	60	Fast	Y	Strong lines between the “channels”
10.1	70	Fast	N	Horizontal lines, Strong lines between the “channels”

Table 4.1: Results of single frame exposures of the detector at room temperature. The ”lines” that appear in the images are on the edges of the bands shown in Figure 4.10. There are 16 bands that are $\sim$ 62 pixels wide in that image. As frame time shortens the lines increase in amplitude. Below are the important parameters used to reproduce these results when running the MACIE control program (msac) program provided by Markury Scientific.

MSAC Paramters
MACIE Firmware File - MACIE_Registers_Fast.mrf
MACIE Clock Phase Shift Value - 0x01c0
ASIC Firmware File
- DevBrd_H1RG_12bit_16output_
SlowMode_1MHz_at_10MHz_Clk_coldASIC_telemetry.mcd
ASIC Preamplifier Scheme - Single Ended

plate temperature, the molybdenum block the MUX is mounted to has an equilibrium temperature of 90 K and can get as warm as 97 K while taking images. The second cryogenic test used solid nitrogen to cool the cold plate and optics down to 57 K. The detector/MUX mount consistently stays about 15 K warmer than the cold plate while converting the liquid nitrogen into solid nitrogen using a vacuum pump. Converting solid nitrogen into liquid nitrogen in the cryostat allows us to reach temperatures down to 52 K on the cold plate. In addition to this, the cool down rate is never too fast for the detector. The equilibrium temperature of the MUX while using solid nitrogen has not been determined yet (we ran out of liquid nitrogen), but the electronics were able to take images with the MUX at 72 K. The picture frame was visible in the MUX images during the liquid nitrogen and solid nitrogen tests. Initially, the next step was to do the same cryogenic tests with the MUX using liquid helium. However, a helium shortage and the cost of liquid helium limited my project to one liquid helium run that will hopefully be used on the detector (Deno Stelter and Philip Hinz, private communication). Most of the thermal contraction within the cryostat happens above 100 K and based on recorded temperatures of the detector base and the cold plate we can assume this will not be an issue moving to helium.

4.7 Cryogenic Detector testing

The HgCdTe detector was used with the buffer board cryogenically behind the ZnSe lens and the filter set shown in 4.3. Using liquid nitrogen and solid nitrogen temperatures the detector is capable of running in slow mode and hybrid fast mode with the buffer board. Liquid helium is the next cryogen we want to use for testing the detector because the dark current quoted in Cabrera et al. (2019) (Figure 4.2) at temperatures 55 K are too high to not saturate the detector regardless of system f number. This section of the chapter describes the results and trouble shooting with the cryogenic testing of the detector to date.

4.7.1 MACIE Phase Offset

The MACIE phase offset is a setting that needs to be adjusted to allow for fast hybrid mode to run without producing First In First Out (FIFO) errors that trigger a halt, preventing an image from reading out. The ideal phase offset changes between systems and the value may change with temperature. At room and liquid nitrogen temperatures, the phase offset that works for all tested read out speeds is the hex value 0x01c0. At solid nitrogen temperatures $\sim$ 66 K, 0x01c0 works well but only up to frame speeds of 17.6 milli-seconds, then the value needs to be adjusted to access higher read out times. 70 milli-seconds is estimated to be enough to overcome the sky background in exoplanet applications but exploring higher readout speeds for HgCdTe detectors could be useful for making their use more general. Figure 4.11 shows a table of the phase offset value and if an image was able to read out or not. The MACIE phase shift values will need to be recorded again when liquid helium is used for operating the detector.

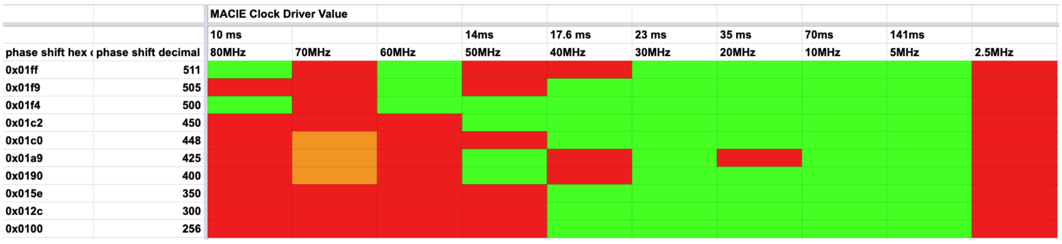

		MACIE Clock Driver Value									
		10 ms			14ms	17.6 ms	23 ms	35 ms	70ms	141ms	
phase shift hex (	phase shift decimal	80MHz	70MHz	60MHz	50MHz	40MHz	30MHz	20MHz	10MHz	5MHz	2.5MHz
0x01ff	511	🟩	🟥	🟩	🟥	🟥	🟩	🟩	🟩	🟩	🟥
0x01f9	505	🟥	🟥	🟩	🟥	🟩	🟩	🟩	🟩	🟩	🟥
0x01f4	500	🟩	🟥	🟩	🟩	🟩	🟩	🟩	🟩	🟩	🟥
0x01c2	450	🟥	🟥	🟥	🟩	🟩	🟩	🟩	🟩	🟩	🟥
0x01c0	448	🟥	🟧	🟥	🟥	🟩	🟩	🟩	🟩	🟩	🟥
0x01a9	425	🟥	🟧	🟥	🟩	🟥	🟩	🟥	🟩	🟩	🟥
0x0190	400	🟥	🟧	🟥	🟩	🟥	🟩	🟩	🟩	🟩	🟥
0x015e	350	🟥	🟥	🟥	🟥	🟩	🟩	🟩	🟩	🟩	🟥
0x012c	300	🟥	🟥	🟥	🟥	🟩	🟩	🟩	🟩	🟩	🟥
0x0100	256	🟥	🟥	🟥	🟥	🟩	🟩	🟩	🟩	🟩	🟥

Figure 4.11: ITAR check. Table of usable MACIE phase shift values for the clock driver. The left columns indicate the phase shift hex value. The red and green boxes under frame exposure times indicate whether or not a frame could be read or not. Red box - Cannot read. Green - can read. Orange - can read sometimes.

4.7.2 Liquid and Solid Nitrogen Testing

The HgCdTe detector operated in slow and hybrid fast mode at $\sim$ 89 K and $\sim$ 58 K using liquid nitrogen and solid nitrogen as cryogens respectively. In both runs the detector did not get cold enough to become light sensitive. The picture frame was visible in the read out images but flux values did not change when alternating though open, closed, and the filters in the filter wheel set. Pictures of the detector images from the liquid nitrogen and solid nitrogen tests are shown in Figure 4.12. These images are the same speeds as the room temperature frames and show similar features. There is less gradient in the vertical direction of the detector when hybrid mode is run cryogenically compared to room temperature. At relatively fast speeds the horizontal lines (described in Table 4.1) between readout channels appears in the images. For speeds faster than 9ms an image can be read out my changing the MACIE phase offset from 0x01c0 to 0x01ff or 1040, but the noise in the few pixels separating read out channels becomes relatively high. Once we test the detector in the light sensitive regime we will need to understand how those intensity peaks influence the overall scientific quality of an

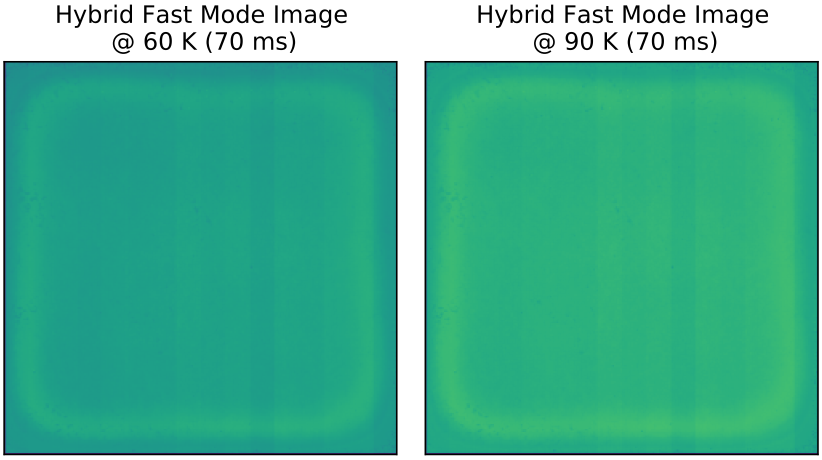

Figure 4.12: Single read out the HgCdTe detector at room temperature in slow and hybrid fast mode.

image. A summary of detector read out testing for liquid nitrogen and solid nitrogen are summarized in Tables 4.2 and 4.3. At these temperatures the detector runs fast enough for what is theoretically needed to overcome the mid-infrared sky background.

4.7.3 Future Liquid Helium Testing and Current Project Status

The last experiment for this project is to cool down the detector using liquid helium into a light sensitive regime where the detector can be characterized in multiple filters. The primary measure of success is the detector being able to capture light without saturating and reading out with the detector electronics at such a cold temperature. Once the detector is functioning, we will measure the dark current, read noise, gain, quantum efficiency, and create a pixel operability map. I can estimate all of these parameters using synthetic HxRG data and test data from the James Webb

Exposure Time (ms)	MACIE Clock Driver (MHz)	ASIC Mode	Worked? (Y/N)	Comments
141.45	5	Fast	Y	
70.7	10	Fast	Y	
35.4	20	Fast	N	read out halted
23.6	30	Fast	Y	
17.7	40	Fast	Y	FIFO errors
14.4	50	Fast	Y	Horizontal lines between the "channels""
11.8	60	Fast	Y	FIFO errors
10.1	70	Fast	Y	Strong Horizontal lines between the "channels""

Table 4.2: Results of single frame exposures of the detector when cooled with liquid nitrogen. The detector mount base held a temperature of 89.4 K to 91.5 K during the time the images were taken. The "lines" that appear in the images are on the edges of the bands shown in Figure 4.10. There are 16 bands that are $\sim$ 62 pixels wide in that image. As frame time shortens the lines increase in amplitude. Below are the important parameters used to reproduce these results when running the MACIE control program (msac) program provided by Markury Scientific.

MSAC Paramters
MACIE Firmware File - MACIE_Registers_Fast.mrf
MACIE Clock Phase Shift Value - 0x01c0
ASIC Firmware File
- DevBrd_H1RG_12bit_16output_SlowMode_1MHz_at_10MHz_Clk_coldASIC_telemetry.mcd
ASIC Preamplifier Scheme - Single Ended

Exposure Time (ms)	MACIE Clock Driver (MHz)	ASIC Mode	Worked? (Y/N)	Comments
141.45	5	Fast	Y	FIFO errors
70.7	10	Fast	Y	FIFO errors
35.4	20	Fast	N	read out halted
23.6	30	Fast	Y	FIFO errors
17.7	40	Fast	N	halted
14.4	50	Fast	Y	FIFO errors, Horizontal lines between the “channels””
11.8	60	Fast	N	halted
10.1	70	Fast	Y	Horizontal lines between the “channels””

Table 4.3: Results of single frame exposures of the detector when cooled with solid nitrogen. The detector mount base held a temperature of 58.9 K to 59.0 K during the time the images were taken. The ”lines” that appear in the images are on the edges of the bands shown in Figure 4.10. There are 16 bands that are $\sim$ 62 pixels wide in that image. As frame time shortens the lines increase in amplitude. Below are the important parameters used to reproduce these results when running the MACIE control program (msac) program provided by Markury Scientific.

MSAC Paramters
MACIE Firmware File - MACIE_Registers_Fast.mrf
MACIE Clock Phase Shift Value - 0x01c0
ASIC Firmware File
- DevBrd_H1RG_12bit_16output_
SlowMode_1MHz_at_10MHz_Clk_coldASIC_telemetry.mcd
ASIC Preamplifier Scheme - Single Ended

Space Telescope NIRSpec detectors. The dark current is estimated by calculating the flux incident onto the detector while the entrance window is blocked off. This is done by calculating the slope on a per pixel basis over time and taking the median of the slopes over the entire detector. The read noise can be estimated using the CDS read configuration of the msac program or by manually subtracting two frames and the residual flux to find the median scatter within the image. Gain of the detector is manually set within the msac program but can be verified by plotting the median variance of a pixel against the median image value for each frame in a series of images. The center of the detector is best for characterizing gain because the response of the detector is more uniform there compared to the edges. Estimating the quantum efficiency of the detector is complicated because you are comparing the measured flux onto the detector compared to what is expected, which includes the response of the entire system and whatever the detector is imaging. The measured flux is estimated by taking slopes over series of frames taken for a source in each filter setting. Knowing the temperature of the source, transmission of the entrance lens, filters, and mirrors, the expected number of electrons on the detector can be estimated. The fraction of measured electrons to the expected electrons is the quantum efficiency of the detector within a given filter. Liquid helium testing to characterize these properties of the detector has not been completed primarily because of a helium shortage that got my order delayed.

In the process of waiting for liquid helium, infrared shielding has been added to the cryostat (Figure 4.13) to minimize the heat from read out electronics or relatively warm areas of the cryostat creating a signal on the detector. Aluminum tape was added

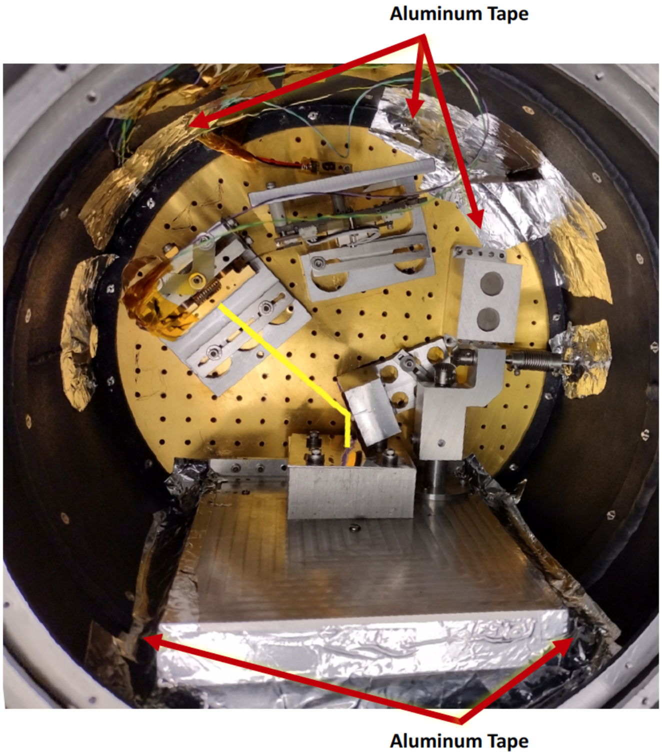

Figure 4.13: The modified entrance lens for the cryostat. The uncoated zinc selenide lens held to the metal base with a circular retainer.

in areas where excess light could potentially shine through onto the detector. These areas were found by shining a flashlight through openings in the dewar while the room was dark. This method is not perfect but it helps with blocking off larger obvious infrared leak sources. Prior to the helium run, the aluminum tape is outgassed by placing the cryostat under vacuum. Outgassing materials is important for allowing the dewar to reach as low of a pressure as possible when cooling it down with cryogens.

Lastly, around the time I figured that only one liquid helium run would be feasible I changed the MUX out for the HgCdTe detector. While doing room temperature testing, the HgCdTe detector stopped working and only read out images that looked like no detector was attached. After trying all previously used settings, I removed the detector and read out electronics from the cryostat to start from ground zero and run the same tests. After about two weeks of troubleshooting I emailed connections at Markury Scientific and Teledyne Scientific to figure out what was wrong. After using firmware updates and toggling extra settings I was asked to investigate the wirebonds on the detector itself. The wirebonds are very fine wires that transfer signal from the detector to the SIDECAR ASIC and close up images revealed that they were touching and possibly getting shorted. This prevented the detector from reading correctly and Teledyne Scientific offered to fix it at no charge. After the fix the detector came back in May and works the same at room temperature. Despite setbacks, the detector has been shown to run in hybrid fast mode cryogenically and once liquid helium becomes available for testing I look forward to see how it will perform under realistic conditions.

Chapter 5

Conclusions and Next Steps

My dissertation work extends beyond the conventional observational wavelength ranges used to find and study the atmospheres of brown dwarfs and directly imaged exoplanets into the mid-infrared. Brown dwarfs across the L, T, and Y sequence all have spectral signatures between 3 μm - 5 μm that imply the presence of disequilibrium atmospheric chemistry due to convective mixing. Both near and mid-infrared spectra of these objects are influenced by atmospheric clouds. Directly imaged exoplanets that may be discovered in the near-future with similar effective temperatures to brown dwarfs will likely have stronger disequilibrium chemistry due to their lower surface gravities and younger ages. The direct imaging method is currently only sensitive to gas-giant exoplanets. To extend the astronomical community's discovery potential into cooler, rocky, Earth-like planets, improvements must be made to understand the optimal components, such as detectors, for mid-infrared imagers that will come online with 30-meter class telescopes.

The work from Chapter 2 demonstrated that late L-dwarfs with similar temperatures to ∼1400 K directly imaged exoplanets have lower apparent methane abundances in the near and mid-infrared due to atmospheric mixing. Despite cooler effective temperatures, there are prominent carbon monoxide features in the near-infrared as if they were much warmer L-dwarfs. These methane features require medium resolution spectroscopy to detect and as with previously published work, clouds and disequilibrium chemistry are required to reproduce the spectra of the exoplanet analogs. The work presented in Chapter 3 shows that brown dwarfs between ∼600 K and ∼250 K, and our own gas giant Jupiter also display disequilibrium chemistry with the primary marker being carbon monoxide gas. Cooler effective temperature brown dwarfs have less carbon monoxide, but require much stronger atmospheric mixing to maintain their abundances. Warmer brown dwarfs have combinations of convective and radiative zones within their upper atmosphere, that can potentially reduce the overall efficiency of atmospheric mixing. A wide range of atmospheric effective temperatures of brown dwarfs are influenced by disequilibrium chemistry and these effects will need to be considered when future observations are done with JWST and ground based instruments.

Planned followup observations with JWST will offer higher signal, resolution, and broader wavelength coverage of brown dwarfs that will potentially access a wider range of molecular gases unobscured by the atmospheric infrared windows of Earth. These data sets will expand our knowledge of upper atmosphere gas composition and also be the benchmark for refining atmospheric models that will eventually get applied to directly imaged gas giant planets. There are numerous guaranteed time observations

(GTO), early release science (ERS), general observer observations that will study the atmospheres of exoplanets and brown dwarfs. The two programs I am participating in after graduate school are the ERS Program 1386: High Contrast Imaging of Exoplanets and Exoplanetary Systems with JWST and the GO Program 2327: Water Ice Clouds and Weather on the Coldest Brown Dwarf. Both programs are extensions of work featured in this dissertation.

5.1 High Contrast Imaging of Exoplanets and Exoplanetary Systems with JWST

The High Contrast Imaging of Exoplanets and Exoplanetary Systems with JWST is a three component program to asses the ability of JWST to observe and characterize directly imaged exoplanets. VHS 1256 b, which was discussed in Chapter 2 will have spectra taken from 1 μm to 28 μm using the NIRSpec and MIRI instruments on JWST. The spectra will be relatively continuous and high signal-to-noise that can access a significant atmospheric pressure range to understand the gas composition and potential cloud structure. Such a wide wavelength range is powerful for understanding what planetary mass objects look like spectroscopically, what cloud species influence the upper atmosphere, and how disequilibrium chemistry varies with atmospheric depth. A subset of the collaboration is using ground-based telescopes to track the variability of VHS 1256 on short time scales in the optical/near-infrared to understand how variable VHS 1256 b object is within timescales of the JWST observations. The ground based observations will not have the same wavelength coverage as the JWST Observations but may help constrain the type or size of cloud influencing the upper atmosphere of VHS 1256 b. Alternatively, the mid-infrared spectra from MIRI could be used to interpret why the time series data have a certain pattern if there is a specific cloud type that can be identified in the longer wavelength portions of the spectra.

5.2 Water Ice Clouds and Weather on the Coldest Brown Dwarf

During JWST Cycle 1, my collaboration will analyze the first spectroscopically resolved variability data for WISE 0855. These observations will shed light on lingering questions regarding the apparent absence of phosphine within the atmosphere of ground based WISE 0855 spectra and characteristics of water clouds. The observations will be completed using NIRSpec to observe WISE 0855 in 15 minute intervals with 2.87 μm – 5.10 μm spectra at a resolution of $\sim$1000 over 11 hours. The estimated rotation period of WISE 0855 based on Spitzer photometry (Esplin et al., 2016) is about 12 hours. Using principle component analysis, the time series data set will be able to distinguish variations due to water clouds or water vapor changes within the atmosphere. The individual pointings and co-added spectra will be used to get better model comparisons to interpret WISE 0855's atmospheric composition.

5.3 Testing HgCdTe Detectors on Sky

In Chapter 4, I discuss work that may demonstrate the effectiveness of mercury cadmium telluride detectors to operate cryogenically and to potentially image Earth-like exoplanets. In addition to the upcoming JWST characterization efforts. I have plans to test this type of detector on sky by upgrading a current instrument NOMIC at the Large Binocular Telescope (LBT) as a postdoctoral scholar. The LBT may not be sensitive to Earth-like planets, but with several nights of data, 10 μm observations can be completed of currently know gas giant planets to asses the detectors ability to produce scientific data. JWST will be able to image gas giants within the mid-infrared with MIRI Imaging, but only with broad band imaging. Ground-based observatories have the advantage of benchmarking data against JWST and choosing filters or dispersion modes that can single out specific potential cloud features for characterization.

Bibliography

Ackerman, A. S., & Marley, M. S. 2001, ApJ, 556, 872

Allers, K. N., Gallimore, J. F., Liu, M. C., & Dupuy, T. J. 2016, ApJ, 819, 133

Allers, K. N., & Liu, M. C. 2013, ApJ, 772, 79

Apai, D., Cowan, N., Kopparapu, R., et al. 2017, arXiv e-prints, arXiv:1708.02821

Arrington, D. C., Hubbs, J. E., Gramer, M. E., & Dole, G. A. 1998, in Society of Photo-Optical Instrumentation Engineers (SPIE) Conference Series, Vol. 3379, Infrared Detectors and Focal Plane Arrays V, ed. E. L. Dereniak & R. E. Sampson, 361–370

Asplund, M., Grevesse, N., Sauval, A. J., & Scott, P. 2009, ARA&A, 47, 481

Atreya, S. K., Crida, A., Guillot, T., et al. 2016, arXiv e-prints, arXiv:1606.04510

Baraffe, I., Chabrier, G., Allard, F., & Hauschildt, P. H. 1998, A&A, 337, 403

—. 2002, A&A, 382, 563

Barman, T. S., Konopacky, Q. M., Macintosh, B., & Marois, C. 2015, ApJ, 804, 61

Barman, T. S., Macintosh, B., Konopacky, Q. M., & Marois, C. 2011a, ApJ, 733, 65

—. 2011b, ApJ, 735, L39

Becklin, E. E., & Zuckerman, B. 1988, Nature, 336, 656

Beichman, C., Gelino, C. R., Kirkpatrick, J. D., et al. 2014, ApJ, 783, 68

Beuzit, J.-L., Feldt, M., Dohlen, K., et al. 2008, in Proc. SPIE, Vol. 7014, Ground-based and Airborne Instrumentation for Astronomy II, 701418

Bézard, B., Lellouch, E., Strobel, D., Maillard, J.-P., & Drossart, P. 2002, Icarus, 159, 95

Bezawada, N., Ives, D., Alvarez, D., et al. 2020, in Society of Photo-Optical Instrumentation Engineers (SPIE) Conference Series, Vol. 11454, Society of Photo-Optical Instrumentation Engineers (SPIE) Conference Series, 114543J

Biller, B. 2017, The Astronomical Review, 13, 1

Biller, B. A., Vos, J., Bonavita, M., et al. 2015, ApJ, 813, L23

Biller, B. A., Vos, J., Buenzli, E., et al. 2018, AJ, 155, 95

Birkmann, S. M., Ferruit, P., Alves de Oliveira, C., et al. 2014, in Proc. SPIE, Vol. 9143, Space Telescopes and Instrumentation 2014: Optical, Infrared, and Millimeter Wave, 914308

Birkmann, S. M., Ferruit, P., Rawle, T., et al. 2016, in Proc. SPIE, Vol. 9904, Space Telescopes and Instrumentation 2016: Optical, Infrared, and Millimeter Wave, 99040B

Bowler, B. P. 2016, PASP, 128, 102001

Bowler, B. P., Liu, M. C., Dupuy, T. J., & Cushing, M. C. 2010, ApJ, 723, 850

Burgasser, A. J., Geballe, T. R., Leggett, S. K., Kirkpatrick, J. D., & Golimowski, D. A. 2006, ApJ, 637, 1067

Burgasser, A. J., Marley, M. S., Ackerman, A. S., et al. 2002, ApJ, 571, L151

Burgasser, A. J., Kirkpatrick, J. D., Cutri, R. M., et al. 2000, ApJ, 531, L57

Burrows, A., Sudarsky, D., & Hubeny, I. 2006, ApJ, 640, 1063

Burrows, A., Sudarsky, D., & Lunine, J. I. 2003, ApJ, 596, 587

Burrows, A., Marley, M., Hubbard, W. B., et al. 1997, ApJ, 491, 856

Cabrera, M. S., McMurtry, C. W., Dorn, M. L., et al. 2019, Journal of Astronomical Telescopes, Instruments, and Systems, 5, 036005

Cabrera, M. S., McMurtry, C. W., Forrest, W. J., et al. 2020, Journal of Astronomical Telescopes, Instruments, and Systems, 6, 011004

Chabrier, G., Mazevet, S., & Soubiran, F. 2019, ApJ, 872, 51

Charnay, B., Bézard, B., Baudino, J. L., et al. 2018, ApJ, 854

Chauvin, G., Lagrange, A.-M., Dumas, C., et al. 2004, A&A, 425, L29

Crawford, S. L., Ragland, S., Booth, A., Colavita, M. M., & Hovland, E. 2006, in Society of Photo-Optical Instrumentation Engineers (SPIE) Conference Series, Vol.

6268, Society of Photo-Optical Instrumentation Engineers (SPIE) Conference Series, ed. J. D. Monnier, M. Schöller, & W. C. Danchi, 62683W

Crossfield, I. J. M. 2015, Publications of the Astronomical Society of the Pacific, 127, 941

Currie, T., Burrows, A., Itoh, Y., et al. 2011, ApJ, 729, 128

Currie, T., Burrows, A., Girard, J. H., et al. 2014, ApJ, 795, 133

Cushing, M. C., Rayner, J. T., & Vacca, W. D. 2005, ApJ, 623, 1115

Cushing, M. C., Roellig, T. L., Marley, M. S., et al. 2006, ApJ, 648, 614

Cushing, M. C., Kirkpatrick, J. D., Gelino, C. R., et al. 2011, ApJ, 743, 50

Cutri, R. M., & et al. 2013, VizieR Online Data Catalog, II/328

Delfosse, X., Tinney, C. G., Forveille, T., et al. 1997, A&A, 327, L25

Dupuy, T. J., & Liu, M. C. 2012, ApJS, 201, 19

Elias, J. H., Joyce, R. R., Liang, M., et al. 2006, in Proc. SPIE, Vol. 6269, Society of Photo-Optical Instrumentation Engineers (SPIE) Conference Series, 62694C

Encrenaz, T. 2022, Icarus, 376, 114885

Encrenaz, T., de Graauw, T., Schaeidt, S., et al. 1996, A&A, 315, L397

Esplin, T. L., Luhman, K. L., Cushing, M. C., et al. 2016, ApJ, 832, 58

Faherty, J. K., Rice, E. L., Cruz, K. L., Mamajek, E. E., & Núñez, A. 2013, AJ, 145, 2

Faherty, J. K., Tinney, C. G., Skemer, A., & Monson, A. J. 2014, ApJ, 793, L16

Faherty, J. K., Riedel, A. R., Cruz, K. L., et al. 2016, ApJS, 225, 10

Filippazzo, J. C., Rice, E. L., Faherty, J., et al. 2015, ApJ, 810, 158

Foreman-Mackey, D., Hogg, D. W., Lang, D., & Goodman, J. 2013, Publications of the Astronomical Society of the Pacific, 125, 306

Gao, P., Wakeford, H. R., Moran, S. E., & Parmentier, V. 2021, Journal of Geophysical Research (Planets), 126, e06655

Gaudi, B. S. 2022, in Astrophysics and Space Science Library, Vol. 466, Demographics of Exoplanetary Systems, Lecture Notes of the 3rd Advanced School on Exoplanetary Science, ed. K. Biazzo, V. Bozza, L. Mancini, & A. Sozzetti, 237–291

Gauza, B., Béjar, V. J. S., Pérez-Garrido, A., et al. 2015, ApJ, 804, 96

Geballe, T. R., Saumon, D., Golimowski, D. A., et al. 2009, ApJ, 695, 844

Geballe, T. R., Saumon, D., Leggett, S. K., et al. 2001, ApJ, 556, 373

Geballe, T. R., Knapp, G. R., Leggett, S. K., et al. 2002, ApJ, 564, 466

Golimowski, D. A., Leggett, S. K., Marley, M. S., et al. 2004, AJ, 127, 3516

Greenbaum, A. Z., Pueyo, L., Ruffio, J.-B., et al. 2018, AJ, 155, 226

Groff, T., Chilcote, J., Brandt, T., et al. 2017, in Proceedings of the SPIE, Volume 10400, id. 1040016 6 pp. (2017)., Vol. 10400

Guzmán-Marmolejo, A., & Segura, A. 2015, Boletín de la Sociedad Geológica Mexicana, 67, 377

Hinkley, S., Skemer, A., Biller, B., et al. 2017, High Contrast Imaging of Exoplanets and Exoplanetary Systems with JWST, JWST Proposal ID 1386. Cycle 0 Early Release Science

Hinz, P., Arbo, P., Bailey, V., et al. 2012, in Optical and Infrared Interferometry III. Proceedings of the SPIE, Volume 8445, article id. 84450U, 10 pp. (2012)., Vol. 8445

Hinz, P. M., Rodigas, T. J., Kenworthy, M. A., et al. 2010, ApJ, 716, 417

Hubeny, I., & Burrows, A. 2007, ApJ, 669, 1248

Hunter, J. D. 2007, Computing in Science Engineering, 9, 90

Irwin, P. G. J. 2003,

—. 2009,

Jones, E., Oliphant, T., Peterson, P., et al. 2001–, [Online; accessed ¡today¿]

Kaeufl, H.-U., Ballester, P., Biereichel, P., et al. 2004, in Proc. SPIE, Vol. 5492, Ground-based Instrumentation for Astronomy, ed. A. F. M. Moorwood & M. Iye, 1218–1227

Kaltenegger, L., Traub, W. A., & Jucks, K. W. 2007, ApJ, 658, 598

Karkoschka, E. 1994, Icarus, 111, 174

Keppler, F., Hamilton, J. T. G., Braß, M., & Röckmann, T. 2006, Nature, 439, 187

Kim, S., Prato, L., & McLean, I. 2015, REDSPEC: NIRSPEC data reduction, ascl:1507.017

Kippenhahn, R., Weigert, A., & Weiss, A. 2012,

Kirkpatrick, J. D. 2005, Annual Review of Astronomy and Astrophysics, 43, 195

Kirkpatrick, J. D. 2005, ARA&A, 43, 195

Kirkpatrick, J. D., Beichman, C. A., & Skrutskie, M. F. 1997, ApJ, 476, 311

Kirkpatrick, J. D., Cushing, M. C., Gelino, C. R., et al. 2011, The Astrophysical Journal Supplement Series, 197, 19

Kirkpatrick, J. D., Gelino, C. R., Cushing, M. C., et al. 2012, ApJ, 753, 156

Kirkpatrick, J. D., Martin, E. C., Smart, R. L., et al. 2019, ApJS, 240, 19

Knapp, G. R., Leggett, S. K., Fan, X., et al. 2004, AJ, 127, 3553

Konopacky, Q. M., Barman, T. S., Macintosh, B. A., & Marois, C. 2013, Science, 339, 1398

Kumar, S. S. 1963, ApJ, 137, 1121

Larkin, J., Barczys, M., Krabbe, A., et al. 2006, in Proc. SPIE, Vol. 6269, Society of Photo-Optical Instrumentation Engineers (SPIE) Conference Series, 62691A

Leconte, J. 2018, ApJ, 853

Leggett, S. K., Morley, C. V., Marley, M. S., & Saumon, D. 2015, ApJ, 799, 37

Leggett, S. K., Morley, C. V., Marley, M. S., et al. 2013, ApJ, 763, 130

Leggett, S. K., Saumon, D., Burningham, B., et al. 2010, ApJ, 720, 252

Leggett, S. K., Saumon, D., Marley, M. S., et al. 2007, ApJ, 655, 1079

Leggett, S. K., Tremblin, P., Esplin, T. L., Luhman, K. L., & Morley, C. V. 2017, ApJ, 842, 118

Leggett, S. K., Saumon, D., Marley, M. S., et al. 2012, ApJ, 748, 74

Leggett, S. K., Dupuy, T. J., Morley, C. V., et al. 2019a, ApJ, 882, 117

—. 2019b, arXiv e-prints, arXiv:1907.07798

Lellouch, E., Bézard, B., Moses, J. I., et al. 2002, Icarus, 159, 112

Lew, B. W. P., Apai, D., Zhou, Y., et al. 2016, ApJ, 829, L32

Li, L., Baines, K. H., Smith, M. A., et al. 2012, Journal of Geophysical Research (Planets), 117, E11002

Line, M. R., Teske, J., Burningham, B., Fortney, J. J., & Marley, M. S. 2015, ApJ, 807, 183

Line, M. R., Wolf, A. S., Zhang, X., et al. 2013, ApJ, 775

Line, M. R., Marley, M. S., Liu, M. C., et al. 2017, ApJ, 848, 83

Liu, M. C., Dupuy, T. J., & Allers, K. N. 2016, ApJ, 833, 96

Liu, M. C., Magnier, E. A., Deacon, N. R., et al. 2013, ApJ, 777, L20

Lodders, K., & Fegley, B. 2002, Icarus, 155, 393

Lucas, P. W., Tinney, C. G., Burningham, B., et al. 2010, MNRAS, 408, L56

Luhman, K. L. 2014, ApJ, 786, L18

Luhman, K. L., & Esplin, T. L. 2016, AJ, 152, 78

Luna, J. L., & Morley, C. V. 2021, ApJ, 920, 146

Lunine, J. I. 1993, The Atmospheres of Uranus and Neptune, https://doi.org/10.1146/annurev.aa.31.090193.001245

Macintosh, B., Graham, J. R., Ingraham, P., et al. 2014, Proceedings of the National Academy of Science, 111, 12661

Macintosh, B., Graham, J. R., Barman, T., et al. 2015, Science, 350, 64

Madden, J., & Kaltenegger, L. 2020, ApJ, 898, L42

Madhusudhan, N., Burrows, A., & Currie, T. 2011, ApJ, 737, 34

Marley, M. S., Saumon, D., Cushing, M., et al. 2012, ApJ, 754, 135

Marley, M. S., Saumon, D., Visscher, C., et al. 2021, arXiv e-prints, arXiv:2107.07434

Marois, C., Macintosh, B., Barman, T., et al. 2008, Science, 322, 1348

Marois, C., Zuckerman, B., Konopacky, Q. M., Macintosh, B., & Barman, T. 2010, Nature, 468, 1080

Martin, E. C., Mace, G. N., McLean, I. S., et al. 2017, ApJ, 838, 73

Martin, E. C., Kirkpatrick, J. D., Beichman, C. A., et al. 2018, ApJ, 867, 109

Mawet, D., Delorme, J. R., Jovanovic, N., et al. 2017, in Society of Photo-Optical Instrumentation Engineers (SPIE) Conference Series, Vol. 10400, Society of Photo-Optical Instrumentation Engineers (SPIE) Conference Series, 1040029

McLean, I. S., Becklin, E. E., Bendiksen, O., et al. 1998, in Proc. SPIE, Vol. 3354, Infrared Astronomical Instrumentation, ed. A. M. Fowler, 566–578

Metchev, S., Marois, C., & Zuckerman, B. 2009, ApJ, 705, L204

Miles, B. E., Skemer, A. J., Barman, T. S., Allers, K. N., & Stone, J. M. 2018, ApJ, 869, 18

Morley, C. V., Fortney, J. J., Marley, M. S., et al. 2015, ApJ, 815, 110

Morley, C. V., Marley, M. S., Fortney, J. J., et al. 2014, ApJ, 787, 78

Morley, C. V., Skemer, A. J., Allers, K. N., et al. 2018, ApJ, 858, 97

Nakajima, T., Oppenheimer, B. R., Kulkarni, S. R., et al. 1995, Nature, 378, 463

Noll, K. S. 1993, in Astronomical Society of the Pacific Conference Series, Vol. 41, Astronomical Infrared Spectroscopy: Future Observational Directions, ed. S. Kwok, 29

Noll, K. S., Geballe, T. R., Leggett, S. K., & Marley, M. S. 2000, ApJ, 541, L75

Noll, K. S., Geballe, T. R., & Marley, M. S. 1997, ApJ, 489, L87

Öberg, K. I., Murray-Clay, R., & Bergin, E. A. 2011, ApJ, 743, L16

Oppenheimer, B. R., Kulkarni, S. R., Matthews, K., & van Kerkwijk, M. H. 1998, ApJ, 502, 932

Patience, J., King, R. R., de Rosa, R. J., & Marois, C. 2010, A&A, 517, A76

Patten, B. M., Stauffer, J. R., Burrows, A., et al. 2006, ApJ, 651, 502

Perryman, M. A. C., Lindegren, L., Kovalevsky, J., et al. 1997, A&A, 500, 501

Pipher, J. L., McMurtry, C. W., Cabrera, M. S., & Forrest, W. J. 2021, Journal of Astronomical Instrumentation, 10, 2150008

Pontoppidan, K. M., Pickering, T. E., Laidler, V. G., et al. 2016, in Society of Photo-Optical Instrumentation Engineers (SPIE) Conference Series, Vol. 9910, Proc. SPIE, 991016

Radigan, J., Jayawardhana, R., Lafrenière, D., et al. 2012, ApJ, 750, 105

Rayner, J., Tokunaga, A., Jaffe, D., et al. 2016, in Proc. SPIE, Vol. 9908, Ground-based and Airborne Instrumentation for Astronomy VI, 990884

Rayner, J. T., Toomey, D. W., Onaka, P. M., et al. 2003, PASP, 115, 362

Reid, I. N., Cruz, K. L., Kirkpatrick, J. D., et al. 2008, AJ, 136, 1290

Rich, E. A., Currie, T., Wisniewski, J. P., et al. 2016, ApJ, 830, 114

Rieke, G. H. 2007, ARA&A, 45, 77

Rieke, G. H., Blaylock, M., Decin, L., et al. 2008, AJ, 135, 2245

Ruiz, M. T., Leggett, S. K., & Allard, F. 1997, ApJ, 491, L107

Saumon, D., & Marley, M. S. 2008, ApJ, 689, 1327

Saumon, D., Marley, M. S., Cushing, M. C., et al. 2006, ApJ, 647, 552

Saumon, D., Marley, M. S., Lodders, K., & Freedman, R. S. 2003, in IAU Symposium, Vol. 211, Brown Dwarfs, ed. E. Martín, 345

Saumon, D., Marley, M. S., Leggett, S. K., et al. 2007, ApJ, 656, 1136

Schneider, A. C., Cushing, M. C., Kirkpatrick, J. D., & Gelino, C. R. 2016, ApJ, 823, L35

Schneider, A. C., Cushing, M. C., Kirkpatrick, J. D., et al. 2015, ApJ, 804, 92

Skemer, A. J., Close, L. M., Szúcs, L., et al. 2011, ApJ, 732, 107

Skemer, A. J., Hinz, P. M., Esposito, S., et al. 2012, ApJ, 753, 14

Skemer, A. J., Marley, M. S., Hinz, P. M., et al. 2014, ApJ, 792, 17

Skemer, A. J., Hinz, P., Montoya, M., et al. 2015, in Proc. SPIE, Vol. 9605, Techniques and Instrumentation for Detection of Exoplanets VII, 96051D

Skemer, A. J., Morley, C. V., Allers, K. N., et al. 2016a, ApJ, 826, L17

Skemer, A. J., Morley, C. V., Zimmerman, N. T., et al. 2016b, ApJ, 817, 166

Skemer, A. J., Stelter, D., Mawet, D., et al. 2018, ArXiv e-prints, arXiv:1808.03304

Skrutskie, M. F., Cutri, R. M., Stiening, R., et al. 2006, AJ, 131, 1163

Smith, M. D. 1998, Icarus, 132, 176

Sorahana, S., & Yamamura, I. 2012, ApJ, 760, 151

—. 2014, ApJ, 793, 47

Spiegel, D. S., & Burrows, A. 2012, ApJ, 745, 174

Stapelbroek, M. G., Petroff, J. J. S., & Bharat, R. 1984, in Infrared and Photoelectronic Imagers and Detector Devices, Proc. IRIS Specialty Group on Infrared Detectors, 63–73

Stephens, D. C., Leggett, S. K., Cushing, M. C., et al. 2009, ApJ, 702, 154

Stone, J. M., Skemer, A. J., Kratter, K. M., et al. 2016, ApJ, 818, L12

Suárez, G., & Metchev, S. 2022, arXiv e-prints, arXiv:2205.00168

The Astropy Collaboration, Price-Whelan, A. M., Sipőcz, B. M., et al. 2018, ArXiv e-prints, arXiv:1801.02634

Thorngren, D. P., Fortney, J. J., Murray-Clay, R. A., & Lopez, E. D. 2016, ApJ, 831, 64

Tremblin, P., Amundsen, D. S., Chabrier, G., et al. 2016, ApJ, 817

Tremblin, P., Chabrier, G., Baraffe, I., et al. 2017, ApJ, 850, 46

Tsuji, T., & Nakajima, T. 2003, ApJ, 585, L151

Van Der Walt, S., Colbert, S. C., & Varoquaux, G. 2011, ArXiv e-prints, arXiv:1102.1523

Visscher, C., Lodders, K., & Fegley, Bruce, J. 2006, ApJ, 648, 1181

Visscher, C., & Moses, J. I. 2011, ApJ, 738, 72

Visscher, C., Moses, J. I., & Saslow, S. A. 2010, Icarus, 209, 602

Wagner, K., Boehle, A., Pathak, P., et al. 2021, Nature Communications, 12, 922

Wang, D., Miguel, Y., & Lunine, J. 2017, ApJ, 850, 199

Wang, J., Mawet, D., Hu, R., & Benneke, B. 2016, in Proc. SPIE, Vol. 9911, Modeling, Systems Engineering, and Project Management for Astronomy VI, 99112T

Wright, E. L., Eisenhardt, P. R. M., Mainzer, A. K., et al. 2010, AJ, 140, 1868

Wright, E. L., Mainzer, A., Kirkpatrick, J. D., et al. 2014, AJ, 148, 82

Yurchenko, S. N., & Tennyson, J. 2014, MNRAS, 440, 1649

Zahnle, K. J., & Marley, M. S. 2014, ApJ, 797, 41

Zalesky, J. A., Line, M. R., Schneider, A. C., & Patience, J. 2019, ApJ, 877, 24